



**A MESOSCALE DYNAMICS
STUDY OF THE PHASES IN
SURFACTANT-WATER
TERNARY SYSTEMS**

By

Neil Denham

A thesis submitted in partial fulfilment for the requirements for
the degree of

Doctor of Philosophy

at the

University of Central Lancashire

December 2008

Declaration

I declare that while registered as a candidate for the research degree, I have not been a registered candidate or enrolled student for another award of the University or other academic or professional institution.

I declare that no material contained in this thesis has been used in any other submission for an academic award and is solely my own work.

Signature of Candidate: 

Type of Award: *Doctor of Philosophy*

Department: *School of Engineering and Physical Sciences*

Abstract

A mesoscale dynamics simulation using a Dissipative Particle Dynamics regime was developed to investigate the ability of small molecules to control phase structures in non-ionic surfactant-water systems. The ability to control phase structure has positive implications for potential templating applications which require ordered and stable phases with high surface curvature. The phases present in such systems were successfully modelled, the results of which compare well with experiment.

Additives which decreased the surface curvature of the interfacial region included oils and long-chained alcohols. These molecules destabilised high-surface curvature phases, such as the bicontinuous cubic and mesh phases, in favour of the lamellar phase.

However, the addition of anaesthetics and short-chained alcohols, which are small amphiphilic molecules, promote surface curvature, and there is an optimum chain length for maximum stability of the mesh phase.

Coulombic interactions, although unsuccessfully modelled with the simulations, were found to be important through Langmuir trough investigations adding ionic and non-ionic anaesthetics to non-ionic surfactant and ionic lipid monolayers, as ionic monolayer-anaesthetic combinations showed a larger increase in surface pressure compared to the non-ionic monolayer-anaesthetic combination.

It is therefore very difficult to engineer phase structures for templating applications because the extreme chemical environment in the templating solution would serve to destabilise any high surface curvature these additives would stabilise.

Contents

Declaration	i
Abstract	ii
Contents	iii
List of Figures	vi
List of Tables.....	xi
Acknowledgements.....	xii
Glossary – Abbreviations & Commonly Used Symbols	xiv
1 Introduction.....	1
1.1 Liquid Crystals.....	1
1.2 Thermotropics	2
1.3 Amphiphiles	3
1.3.1 The hydrophobic Effect.....	4
1.3.2 Aggregation.....	5
1.3.3 Critical Micelle Concentration.....	6
1.4 Phases.....	7
1.4.1 Geometry of Aggregates	7
1.4.2 Classical Phases	11
1.4.3 Intermediate.....	14
1.4.4 Nomenclature	15
1.4.5 Diagrams	16
1.5 Previous Work.....	18
1.5.1 Binary Systems	18
1.5.2 Intermediate Phases.....	20
1.5.3 The addition of oil.....	24
1.5.4 The addition of anaesthetics.....	28
1.6 Aim of the Study: Controlling the Phases.....	32
1.7 References	33

2	Computational Model	38
2.1	Introduction.....	38
2.2	Computer Simulations.....	38
2.2.1	Molecular Dynamics.....	38
2.2.2	Monte Carlo.....	39
2.2.3	Finite-size effects.....	40
2.3	Selection of Simulation Method.....	40
2.4	Simulations Literature Review.....	41
2.5	Dissipative Particle Dynamics.....	44
2.6	DPD Parameters.....	46
2.6.1	Time evolution & Temperature Stability.....	46
2.6.2	Units.....	47
2.6.3	The Repulsion Parameter.....	47
2.6.4	Hydrophobic Repulsion.....	49
2.7	Model.....	50
2.7.1	Length Scale.....	50
2.7.2	Bonds.....	51
2.8	Simulation Hardware & Software.....	52
2.9	References.....	52
3	DPD Binary System – Parameter Setting	55
3.1	Introduction.....	55
3.2	Experimental Results.....	55
3.3	Bond Strength k	56
3.4	Phase Sequence & Phase Definitions.....	57
3.5	Δa Phase Diagram.....	62
3.6	a_{BB} Phase Diagram.....	63
3.7	Box Sizes.....	64
3.8	Summary.....	66
3.9	References.....	67
4	Oil Addition	68
4.1	Introduction.....	68
4.2	Modelling Oil.....	68
4.3	Method.....	69
4.4	Oil Addition Results.....	69
4.4.1	Hexane.....	69
4.4.2	Dodecane.....	71
4.4.3	Octadecane.....	72
4.4.4	Comparison of the Phase Diagrams.....	73
4.5	Analysis.....	75
4.5.1	d_0 Spacing and Oil Behaviour in the Tail Region.....	75
4.5.2	Probability Density Functions of Lamellar Phases.....	84
4.5.3	Tail Bead Probability Density Functions.....	90
4.6	Comparison with Experimental Results.....	93
4.7	Temperature and Concentration Equivalence.....	94
4.8	Experimental Findings.....	95
4.9	Discussion.....	97
4.10	Summary.....	97
4.11	References.....	98

5	Modelling Anaesthetics & Alcohols.....	99
5.1	Introduction.....	99
5.2	Modelling Anaesthetics.....	99
5.3	Results.....	99
5.3.1	d_0 and S_a	101
5.3.2	Probability Density Functions of Lamellar Phases.....	102
5.4	Modifying the Anaesthetic Parameters.....	103
5.4.1	Modifying Anaesthetic Tail-Surfactant Tail Interaction Strength.....	103
5.4.2	Modifying Anaesthetic Head-Water Interaction Strength.....	105
5.5	Comparison to Experiment.....	110
5.6	Alcohol.....	112
5.7	Summary.....	117
5.8	References.....	117
6	Langmuir-Blodgett Trough.....	118
6.1	Introduction.....	118
6.2	Monolayers.....	118
6.3	Materials.....	119
6.4	Experimental Apparatus.....	120
6.5	Compression Isotherms.....	121
6.6	Surface Activity.....	125
6.7	Amphiphile Anaesthetic Interactions.....	128
6.8	Conclusion.....	131
6.9	Summary.....	132
6.10	References.....	132
7	Conclusion and Further work.....	134
7.1	Conclusion.....	134
7.2	Further work.....	135
	Appendix A – About OCTA & COGNAC.....	136
	Appendix B.....	137
	Appendix C.....	139
	Afterword.....	140

List of Figures

Figure 1.1 The average direction of the liquid crystals indicates the director \hat{n} . The molecular long axis is denoted by a	2
Figure 1.2 Typical thermotropic phase sequence on heating (left to right) or reverse on cooling.....	3
Figure 1.3 An Amphiphile	3
Figure 1.4 A spherical micelle, upon aggregation above the critical micelle concentration (CMC)	5
Figure 1.5 Sketch showing how solubility and CMC affect micelle formation.....	7
Figure 1.6 The interfacial region of an aggregation of amphiphiles.....	8
Figure 1.7 Mean curvature is measured by taking the radius of curvature in two perpendicular directions.	9
Figure 1.8 From left to right, spherical micelles, the hexagonal and lamellar phases.	11
Figure 1.9 The micellar cubic phase, with slightly elongated micelles packed in a body centred cubic arrangement.	12
Figure 1.10 From left to right, the inversed micellar phase and inversed hexagonal phase.....	13
Figure 1.11 Bicontinuous Cubic phases, showing the Ia3d, Pm3m and Im3m space groups from left to right ^[16]	14
Figure 1.12 The Ribbon Phases, showing the c2mm and p2gg space groups from left to right	14
Figure 1.13 The mesh phase. The rhombohedral mesh phase is a three connected structure with monodisperse pores stacked in an ABC fashion. The random mesh phase has pores with distribution in size and there is no correlation between layers. .	15
Figure 1.14 Schematic representation of the sponge phase ^[28]	15
Figure 1.15 A (simplified) typical phase diagram (not all phases would be present for any one system). Water rich and surfactant rich regions are denoted by w and x respectively.	17
Figure 1.16 Phase diagram upon cooling (left) and heating (right) for C ₁₆ E ₆ from reference ^[19]	19
Figure 1.17 Phase diagram for C ₁₂ E ₆ , taken from reference ^[33]	19
Figure 1.18 A penetrating oil, shorter than the alkyl chain of the surfactant.....	25
Figure 1.19 A swelling oil, longer than the alkyl chain of the surfactant.	26
Figure 1.20 Phase diagram for addition of oils to C ₁₆ EO ₆ -water mixture, taken from reference ^[49] . C ₁₆ E ₆ /water/1-hexene (red), C ₁₆ E ₆ /water/n-decane (blue) and C ₁₆ E ₆ /water/n-octadecane (green), all on cooling.	27
Figure 1.21 Typical Anaesthetic molecules (a) Halothane, (b) Sodium Thiopental, (c) Lidocaine (base form), (d) Ketamine hydrochloride, (e) Prilocaine hydrochloride and (f) Lidocaine hydrochloride. ^[52,55,56]	29

Figure 1.22 Effect of a type I anaesthetic (red) and type II anaesthetic (blue), taken from reference ^[61]	30
Figure 2.1 Excess pressure as a function of simulated density. The DPD equation of state holds above $\rho \approx 3$, where the graph becomes linear. Taken from ^[13]	51
Figure 3.1 Phase diagram for $C_{12}E_6$, taken from reference ^[1]	55
Figure 3.2 Average bond length as a function of bond spring constant. Errors show the standard deviation of the bond length. Line is a guide to the eye.	57
Figure 3.3 A Total energy v time plot for a typical simulation. Line is a guide to the eye.	58
Figure 3.4 Isodensity surface images of $C_{12}E_6$ -water simulations after 100,000 time steps showing the interface between the head and the tail region.	60
Figure 3.5 Bead-stick images of (a) H_1 phase, 60% and (b) L_α phase (90%). Dark blue represents head beads, light blue represents water beads and red represents tail beads.	61
Figure 3.6 Phase Diagram showing phase sequence with different hydrophobic interaction parameters. Lines are a guide to the eye.	62
Figure 3.7 Phase Diagram showing phase sequences for different head to head interaction parameters. Lines are a guide to the eye.	63
Figure 3.8 Phase Diagram showing phase sequence for different box sizes.	64
Figure 4.1 Molecular structure and DPD bead representation of the three oils added in the simulations.	69
Figure 4.2 Phase diagram showing phases on increasing mole fraction of hexane (14.5nm box). Filled squares = L_α , open circles = Mh_1 , filled diamonds = L_3 and open triangles = dV_1 . Lines are a guide to the eye.	70
Figure 4.3 Phase diagram showing phases on increasing mole fraction of hexane (8.75nm box). Filled squares = L_α , open circles = Mh_1 , filled diamonds = L_3 and open triangles = dV_1 . Lines are a guide to the eye.	70
Figure 4.4 Phase diagram showing phases on increasing mole fraction of dodecane (14.5nm box). Filled squares = L_α , open circles = Mh_1 , filled diamonds = L_3 and open triangles = dV_1 . Lines are a guide to the eye.	72
Figure 4.5 Phase diagram showing phases on increasing mole fraction of octadecane (14.5nm box). Filled squares = L_α , open circles = Mh_1 , filled diamonds = L_3 and open triangles = dV_1 . Lines are a guide to the eye.	73
Figure 4.6 Composite Phase Diagram for all three oils as a function of oil volume fraction	74
Figure 4.7 Isodensity images of phase structures on the addition of hexane (left), dodecane (middle) and octadecane (right) at $X_{sw}=0.16$	74
Figure 4.8 (a) Schematic of a simulation box with a lamellar phase orientated so that there are 3 repeats in the x direction, 2 repeats in the y direction and 1 in the z direction. (b) Schematic diagram showing the angles α and β , used to calculate d_0 . n_{xy} is a line normal to the lamellae plane residing in the xy plane. α is the angle between x and n_{xy} , and β is the angle between n_{xy} and n, a line normal to the lamellae plane.	77

Figure 4.9 d_0 spacing as a function of oil mole fraction. Lines are least squares fit....	78
Figure 4.10 d_0 spacing as a function of oil volume fraction. Lines are least squares fit.	78
Figure 4.11 Orientations of lamellae in simulation box on increasing octadecane concentration. Orientation changes as lamellae thicken because of swelling behaviour of octadecane.....	79
Figure 4.12 Ideal penetrating and swelling behaviour for hexane and octadecane respectively, compared to simulation results.	81
Figure 4.13 Surface area per head group for ideal penetrating and swelling behaviour	82
Figure 4.14 Ideal penetrating and swelling behaviour for dodecane	83
Figure 4.15 Surface area per head group for Ideal penetrating and swelling behaviour for dodecane	84
Figure 4.16 Typical probability density function across lamellar phase showing tail, head, water and oil beads. Graph shown is of 0.04 hexane mole fraction, $X_{sw}=0.75$. Filled squares = tail, open circles = head, filled diamonds = water and open triangles = oil beads.	85
Figure 4.17 Probability density functions for oil (left) and tail (right) beads for oils. Arrows indicate increasing oil concentration.....	87
Figure 4.18 Probability density functions for oil (left) and tail (right) beads from low to high concentrations (top to bottom). Arrows indicate the increasing length of oil (butane, hexane, dodecane and octadecane).	88
Figure 4.19 Oil FWHM for increasing oil mole fraction. Lines are least squares fit. .	89
Figure 4.20 Tail FWHM for increasing oil mole fraction. Lines are least squares fit.	89
Figure 4.21 Tail Bead Probability Density Function example.....	90
Figure 4.22 FWHM for beads 1 and 2 for (a) butane, (b) hexane, (c) dodecane and (d) octadecane. Filled circles = bead 1 and open squares = bead 2.	91
Figure 4.23 Peak Separation for beads 3 and 4 for (a) butane, (b) hexane, (c) dodecane and (d) octadecane. Filled squares = bead 3 and open triangles = bead 4.	92
Figure 4.24 Two possibilities leading to wider peak for bead 1 than bead 2 in probability density function. (a) Angle between beads 3, 2 and 1 is less than 90° . (b) Interdigitation of tails.....	93
Figure 4.25 Lamellar spacing as a function of hexane mole fraction. Taken from ^[1,2]	96
Figure 4.26 Lamellar spacing as a function of octadecane mole fraction. Taken from ^[1,2]	96
Figure 4.27 Surface area per molecule as a function of mole fraction of oil. Taken from ^[1,2]	96
Figure 5.1 Schematic showing generic anaesthetic molecule with one hydrophobic bead (red) and one hydrophilic bead (blue) connected with a bond.	99

Figure 5.2 Phase diagram showing phases on increasing mole fraction of anaesthetic (14.5nm box) Filled squares = L_α , open circles = Mh_1 , filled diamonds = L_3 and open triangles = dV_1 . Lines are a guide to the eye.	100
Figure 5.3 Isodensity images showing phase structures on the addition of anaesthetic at $X_{sw}=0.16$	100
Figure 5.4 d_o spacing as a function of anaesthetic mole fraction.....	101
Figure 5.5 S_a as a function of anaesthetic mole fraction.....	101
Figure 5.6 Probability density function of lamellar phase for $\phi_{an}= 0.02$ (a), 0.04 (b), 0.06 (c) and 0.08 (d). Filled squares = tail, open circles = head, filled diamonds = water and open triangles = anaesthetic.	102
Figure 5.7 Composite probability density functions of lamellar phase for anaesthetic beads for $\phi_{an}= 0.02$ (Filled triangles), 0.04 (open squares), 0.06 (filled diamonds) and 0.08 (open circles).....	102
Figure 5.8 Phase diagram showing phases on increasing mole fraction of anaesthetics with $a_{TS^*Ta} = 25, 30$ and 35 (14.5nm box). Filled squares = L_α , open circles = Mh_1 , filled diamonds = L_3 and open triangles = dV_1 . Lines are a guide to the eye.	104
Figure 5.9 Phase diagram showing phases on increasing mole fraction of anaesthetics with $a_{HaW} = 15, 20, 25, 30$ and 35 (14.5nm box). Filled squares = L_α , open circles = Mh_1 , filled diamonds = L_3 and open triangles = dV_1 . Solid lines are a guide to the eye.	106
Figure 5.10 Phase transition concentration for the addition of anaesthetic for the $L_3 - Mh_1$ transition at $X_{sw}=0.16$	108
Figure 5.11 Phase transition concentration for the addition of anaesthetic for the $Mh_1 - dV_1$ transition at $X_{sw}=0.16$	108
Figure 5.12 Phase transition concentration for the addition of anaesthetic for the $Mh_1 - dV_1$ transition at $X_{sw}=0.23$	109
Figure 5.13 Phase transition concentration for the addition of anaesthetic for the $L_\alpha - Mh_1$ transition at $X_{sw}=0.36$	109
Figure 5.14 Phase diagram showing phases on increasing mole fraction of AB (14.5nm box). Filled squares = L_a , open circles = Mh_1 , filled diamonds = L_3 and open triangles = dV_1 . Solid lines are a guide to the eye.	113
Figure 5.15 Phase diagram showing phases on increasing mole fraction of A_2B (14.5nm box). Filled squares = L_a , open circles = Mh_1 , filled diamonds = L_3 and open triangles = dV_1 . Solid lines are a guide to the eye.	114
Figure 5.16 Phase diagram showing phases on increasing mole fraction of A_3B (14.5nm box). Filled squares = L_α , open circles = Mh_1 , filled diamonds = L_3 and open triangles = dV_1 . Solid lines are a guide to the eye.	114
Figure 5.17 Phase diagram showing phases on increasing mole fraction of A_4B (14.5nm box). Filled squares = L_α , open circles = Mh_1 , filled diamonds = L_3 and open triangles = dV_1 . Solid lines are a guide to the eye.	115
Figure 5.18 Composite Phase diagram showing phases on increasing mole fraction of AB, A_2B , A_3B and A_4B (14.5nm box). Filled squares = L_a , open circles = Mh_1 , filled diamonds = L_3 and open triangles = dV_1 . Solid lines are a guide to the eye. Phase	

region for L_3 remains same for all alcohols, and as chain lengthens beyond A_2B phase region for dV_1 extends (boxes) and phase boundary for Mh_1 to L_α transition lowers (lines).....	115
Figure 5.19 Isodensity surfaces showing phase structures on the addition of alcohol A_2B left and A_4B (right) at $X_{sw}=0.16$	116
Figure 5.20 Surface curvature promoted by short chain alcohol/anaesthetic molecules (left), Surface Curvature flattened by long chain alcohols (right).	116
Figure 6.1 Molecular structure of the anaesthetics prilocaine hydrochloride (a) and lidocaine (base form) (b).....	120
Figure 6.2 Molecular structure of the lipids DMPC and DMPS.....	120
Figure 6.3 Schematic Diagram of Langmuir-Blodgett Trough.....	121
Figure 6.4 Langmuir-Blodgett trough set up for compressional isotherms. Anaesthetics are spreaded dropwise onto subphase with a syringe allowing a monolayer to form.....	122
Figure 6.5 Isotherm for lidocaine.....	122
Figure 6.6 Isotherm for prilocaine hydrochloride.....	122
Figure 6.7 C_s^{-1} as a function of surface area per molecule of lidocaine.....	124
Figure 6.8 C_s^{-1} as a function of surface area per molecule of prilocaine hydrochloride.....	124
Figure 6.9 Schematic diagram of the Langmuir–Blodgett trough set up for surface activity experiments. Anaesthetics float up to surface after injection.	126
Figure 6.10 Surface Pressure increase on the addition of 10mM prilocaine hydrochloride (after 120 seconds) to a Tris subphase.....	126
Figure 6.11 Surface Pressure increases of prilocaine hydrochloride added to a Tris Buffer. Line is a guide to the eye.	127
Figure 6.12 Surface Pressure increases of lidocaine added to a Tris Buffer. Line is a guide to the eye.	127
Figure 6.13 Langmuir-Blodgett set up for amphiphile-anaesthetic interaction experiments. Anaesthetics float up to surface after injection, changing surface pressure of monolayer.	128
Figure 6.14 Typical surface pressure increase plot: The addition of 10mM lidocaine to a DMPC monolayer.	129

List of Tables

Table 2.1 Densities and volumes for water, hydrocarbon and oxyethylene groups. ...	50
Table 3.1 Parameters and values selected for the model	67
Table 5.1 Phase transition concentrations on changing surfactant tail-anaesthetic tail repulsion parameter	105
Table 5.2 Phase transition concentrations on changing anaesthetic head-water repulsion parameter	106
Table 5.3 Summary of the results of adding anaesthetics to bulk surfactant-water systems in experiment and simulation for ease of comparison.....	111
Table 6.1 Surface Pressure increases for different anaesthetic-surfactant/lipid combinations	129
Table 6.2 Surface Pressure Increases ($\text{mNm}^{-1} \pm 0.1 \text{ mNm}^{-1}$) after averaging results from both surfactants and both lipids.....	129
Table 6.3 pK_a and pH values for the anaesthetics showing degree of protonation....	130

Acknowledgements

Looking back on the past three years and three months, I don't recall any particular time when the going got *really* tough or I didn't know where to go having reached a certain point. I had expected that at some point I was bound to tackle seemingly insurmountable obstacles and reach what would seem like dead-ends, but I appear to have come out of the process reasonably smoothly. I owe this entirely to all of the people who have helped me on my way, and without them, not only would I have continuously struggled but probably even failed to even get this far.

Firstly, I must once again thank my director of studies, Prof. Mike Holmes. He has been the dominant impetus to my research from its inception, and without which the result of which would be insignificant and meaningless. He asked all the right questions, gave me direction and offered suggestions.

Second supervisor Dr Andrei Zvelindovsky receives thanks for offering much help and advice throughout the modelling process. Most importantly, I am grateful for his optimism and belief for our computational approach.

Guo Xiaohu offered much assistance in helping set up simulations on a great supercomputer cluster, and ensured that the simulations were completed quickly and efficiently. Without his help, I may still be gathering results!

Also on the computational side of things, I'd like to thank Dung Ly and Marco Pinna, for helping me get to grips with OCTA and molecular dynamics simulations, respectively.

On the experimental side of things, I am greatly indebted to Dr Sarah Dennison for her help and support throughout all of the trough work; without her, such work would have been beyond the realms of possibility.

To spend such a significant time on a piece of work and remain sane, one needs a productive and friendly environment. Fellow researchers are to thank for providing an excellent atmosphere to work in, contributing both useful answers to chemistry-based questions, and much hilarity. On that note, I better thank them also for putting up with my sense of 'Yuma'. Fabrice, thanks for all of your help scientific and otherwise. Ralph, thanks to you (and your Scottish alter ego) for all of your encouragement throughout. Sarah (G), I must thank you for your friendship and sense of humour. Tina, thanks so much for your motivation, enthusiasm and optimism. Thanks also go to Jane, Jordy, Julie, Dave, Richard, Mick, Phil, James, Kim and Natalie for additional

moral support and encouragement, and any others who have helped me but I've neglected to mention here; there have been so many people who have helped with this work, and you know what I'm like with remembering things.

Finally, I'd like to thank my family for all of the encouragement I received throughout this work, while at home and away, and for understanding when I couldn't visit as often as I'd have liked to!

Preston

September 2008

Glossary – Abbreviations & Commonly Used Symbols

Abbreviations

LCD	Liquid Crystal Display
CMC	Critical Micelle concentration
SAXS	Small Angle X-ray Scattering
SANS	Small Angle Neutron Scattering
PFC	Parabolic Focal Conic
NMR	Nuclear Magnetic Resonance
MD	Molecular Dynamics
MC	Monte Carlo
DPD	Dissipative Particle Dynamics
FWHM	Full width at Half Maximum of a peak

Liquid Crystal Symbols

S	Orientational order parameter
\hat{n}	Liquid crystal director
θ	Angle between each individual molecule's long axis and \hat{n}

Thermodynamic Symbols

β	Compressibility
V	Volume
P	Pressure
ρ	Density
T	Temperature
N	Number of molecules/Aggregation number
R	Gas constant ($8.31 \text{ JK}^{-1}\text{mol}^{-1}$)
k_B	Boltzmann's constant ($1.38 \times 10^{-23} \text{ JK}^{-1}$)

Aggregation Symbols

μ	Chemical potential
μ_N	Mean chemical potential of molecule in aggregate of N molecules
μ_N^0	Mean interaction free energy per molecule (Standard component of μ)
X_N	Concentration of molecules in aggregates of N molecules
N_S	Surfactant parameter
V	Volume of hydrocarbon chain
l_c	Max length above which molecule no longer considered fluid
l_{max}	All-trans length of chain (stretched)
H	Mean curvature
R_1, R_2	Radii of curvature

Nomenclature of Phases

L_1, L_2	Normal and inversed micellar phases
L_3	Sponge phase
H_1, H_2	Normal and inversed hexagonal phases
V_1	Bicontinuous cubic phase
L_a	Lamellar phase
Mh_1	Mesh phase
Rb	Ribbon phase
Bc	Bicontinuous Intermediate phase

DPD Symbols & Units

r_i	Position of i^{th} particle
p_i	Momentum of i^{th} particle
Δt	Value of time step
m_i	Mass of i^{th} particle
F_{ij}^T	Total force on a particle
γ	Friction coefficient
σ	Amplitude of noise
w_D, w_R	Weight functions
e_{ij}	$=(r_i - r_j)/r_{ij}$
ζ_{ij}	Gaussian white noise term
v_i	Velocity of i^{th} particle
λ	Constant associated with time integration
r_c	Cut off radius
ρ_A	Density of component A
V_B	Volume per bead
β	Compressibility
ρ	Bead density
a_{ij}	Repulsion parameter
Δa	Excess/hydrophobic repulsion parameter
a_{AB}	Repulsion between bead A and bead B
a_{TsTa}	Repulsion between tail of surfactant and tail of anaesthetic
a_{HaW}	Repulsion between head of anaesthetic and water
τ	DPD unit of time
ε	DPD unit of energy
σ	DPD unit of length

Monolayer Symbols

M	Concentration in moles
Π	Surface pressure
γ	Surface tension of pure liquid
γ_0	Surface tension of film-covered surface
C_s^{-1}	Compressibility modulus
A	Surface area
R_0	Natural radius of curvature
k_c	Constant of rigidity

Other Symbols

X_{sw}	Surfactant to water mole ratio
X_{os}	Oil to surfactant mole ratio
φ_A	Mole/Volume fraction of component A
φ_{alkyl}	Volume fraction of alkyl chain
$\varphi_{but}, \varphi_{hex} \dots$	Mole fraction of butane, hexane, etc.
d_0	Lamellar layer repeat distance
d_{hc}	Hydrophobic region thickness
S_a	Effective surface area per headgroup molecule
d_0^0	Lamellar layer repeat distance in binary system
d_{hc}^0	Hydrophobic region thickness in binary system
S_a^0	Effective head group area per molecule in binary system
χ	Flory-Huggins parameter
F	Degrees of freedom
P	Number of phases
C	Number of components
δE	Energy per unit area
$\Delta\nu$	Quadrupolar splitting (Obtained from NMR spectroscopy)
ΔE	Change in energy
k	Spring constant
r	Bond length
r_o	Equilibrium bond length
U_{bond}	Bond potential
f	Frequency
L	Side length of simulation box
n_x	Number of discrete lamellae in x direction
v_a	Volume of constituent a
α, β	Angles from simulation box axes to direction normal to lamellae
F	Free energy per lattice site
f_v	Free energy corresponding to single component
Type I An.	Anaesthetic with polar moiety
Type II An.	Anaesthetic with localised charge

1 Introduction

1.1 Liquid Crystals

The term liquid crystal is used to describe a fourth phase of matter, occurring between solids and liquids for certain compounds and mixtures of compounds. This phase has distinct crystalline features like a solid, but still flows like a liquid. Liquid crystals are able to exhibit optical birefringence and X-ray diffraction because their molecules possess long range orientational and sometimes positional order - properties usually associated with crystals.

Liquid Crystals were first observed in the late 19th Century by Virchow, a biologist who noticed birefringence in certain nerve fibres in water. However, this birefringence was not attributed to a separate phase until Reinitzer, an Austrian Botanist, found two distinct melting points for cholesterol benzoate ^[1]. Although liquid crystals were observed before him, Reinitzer is regarded as the discoverer of liquid crystals. He sent his samples to Lehmann ^[2], a German chemist who studied crystalline solids with a heating stage attached to his microscope. Lehmann was convinced that the fluids, observed as an amorphous form from which solids crystallised, were a different phase, and began to call them liquid crystals. Upon heating, the first melting point is when the solid changes to an opaque liquid, the liquid crystal. After further heating, the second melting temperature is reached where the liquid crystal melts into a transparent liquid. Research in the field of liquid crystals did not take off until Gray et al ^[3] studied their response to electric fields leading to the development of liquid crystal displays (LCD) in the 1960s.

The fundamental property of a liquid crystal is that it possesses long range orientational order of its molecules. To fulfil this condition the molecules must be anisometric, i.e., they have an axis substantially longer than the other two axes.

The orientational order that a liquid crystal possesses is described by the liquid crystal director \hat{n} , which points in the same direction as the average direction of the molecular long axis (See Figure 1.1). The degree to which the liquid crystals align with this director is quantified by S , the orientational order parameter. The orientational order parameter is defined by the equation ^[2]:

$$S = \frac{1}{2} \langle 3 \cos^2 \theta - 1 \rangle \quad (1.1)$$

θ is the angle between each individual molecule's long axis and the director direction \hat{n} , and S may take values from 0 (no order, isotropic phase) to 1 (perfect orientational order). $S > 0.4$ for a typical liquid crystal phase.

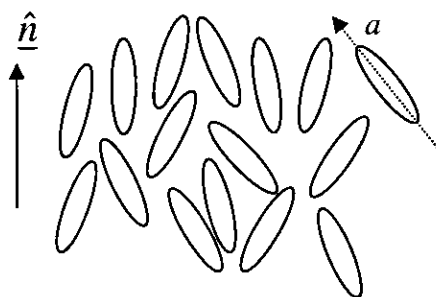


Figure 1.1 The average direction of the liquid crystals indicates the director \hat{n} . The molecular long axis is denoted by a .

There are two main types of liquid crystal, thermotropic and lyotropic. Lyotropic liquid crystals are the focus in this research, and will be considered in more detail. The basics of thermotropic liquid crystals are included for the sake of completeness. Thermotropic liquid crystals are those that change phase on changing temperature ^[2], whereas lyotropic liquid crystals are formed upon dissolution of amphiphilic molecules in a solvent (normally water). Lyotropic phases are formed by changing the concentration of the amphiphile as well as the temperature. Lyotropics have a wide range of uses such as soaps, detergents, emulsifiers, cosmetics and agrochemicals. A large part of lyotropic research is devoted to biological systems, such as cell membranes.

1.2 Thermotropics

A compound that exhibits thermotropic properties changes from crystal, to liquid crystal to isotropic liquid upon heating, and the reverse upon cooling (See Figure 1.2). Thermotropic liquid crystals are made up of anisotropic molecules, where one axis is larger than others, facilitating long range orientational order. They may also have translational order in 1, 2 or 3 dimensions. Thermotropics studied to date have been either rod or disc shaped. These are known as calamitic or discotic liquid molecules, respectively. Thermotropics are widely used for display devices such as calculators and flat screen monitors.

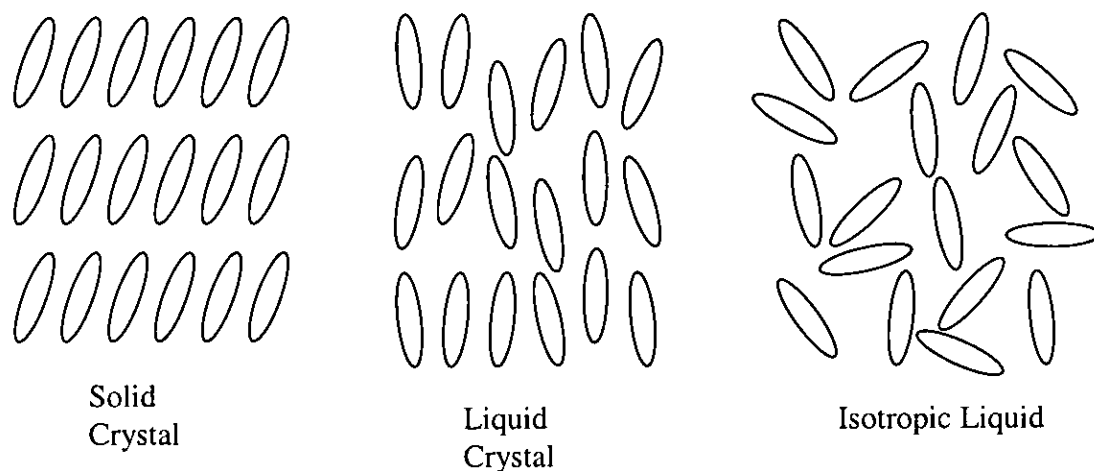


Figure 1.2 Typical thermotropic phase sequence on heating (left to right) or reverse on cooling.

1.3 Amphiphiles

An amphiphile is a molecule consisting of two moieties, a hydrophilic head group and a hydrophobic tail group (see Figure 1.3). The head group may be charged (ionic), uncharged (non-ionic) or zwitterionic (having two opposite charges, such as lipids). The tail group is a non polar hydrocarbon or fluorocarbon chain. Amphiphiles are also known as surface active agents, or surfactants for short. These are molecules are wetting agents that reduce the surface tension of water by adsorbing onto the liquid-gas interface. Because of this property, surfactants are widely used as detergents, emulsions, coatings, etc.

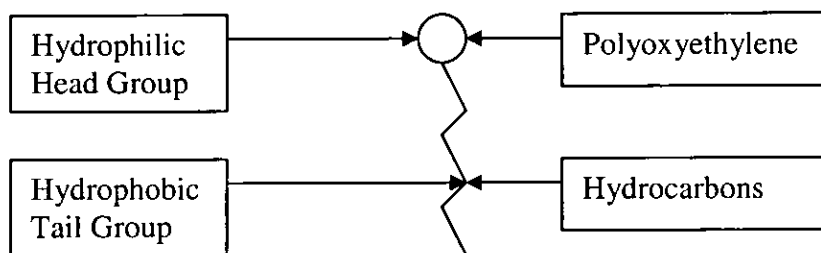


Figure 1.3 An Amphiphile

1.3.1 The hydrophobic Effect

Water is the most abundant molecule on the earth's surface. However, despite its abundance, it has some unusual properties, and in particular two special interactions can occur, namely hydrogen bonding, and the hydrophobic effect. For a liquid with a relatively low molecular weight, it has unexpectedly high melting and boiling points [4]. The solid is an open structure of lower density than its liquid. The strong intermolecular bonds formed in ice must therefore persist into the water state, and they must have orientation dependence as water has a tetrahedral coordination, with four nearest neighbours per molecule. The intramolecular O-H bond distance is about 0.10nm, but the intermolecular O-H bond distance is 0.18nm, much less than summing the two van der Waals radii (0.26nm). This suggests the existence of an intermolecular O-H bond, and is referred to as a hydrogen bond. Hydrogen bonds are also found in other compounds, between electronegative atoms such as O, N, F and Cl and H atoms covalently bound to electronegative atoms themselves.

The strong tendency of water molecules to form hydrogen bonds with each other influences interactions with non-polar molecules that are incapable of forming hydrogen bonds (alkanes, hydrocarbons, fluorocarbons and inert atoms). In this case, water molecules have at least one of their four charges pointing towards the solute molecule, and this will be lost to hydrogen bond formation. The best configuration is to have the least tetrahedral charges pointing towards the unaccommodating species. If the non-polar solute is not too large, it is possible for the water to pack around it without losing any hydrogen bonds [5]. Reorientation and restructuring of water around a non-polar solute or surface is entropically unfavourable, as it disrupts the existing water structure, imposing a new, more ordered structure. Therefore hydrocarbons are not very soluble in water, characterised by highly unfavourable free energy of solubilisation that is mainly entropic. This immiscibility of inert substances with water and mainly entropic nature of this incompatibility is known as the hydrophobic effect [6]. Therefore, with an adequate concentration of amphiphiles dissolved in water, the amphiphiles are able to form supramolecular structures to reduce entropically unfavourable contact between tail groups and water.

Related to the hydrophobic effect is the hydrophobic interaction. This describes the unusually strong interaction between hydrophobic molecules in water, often stronger

than in free space. There have been few direct measurements of the hydrophobic interaction, mainly because the non-polar molecules are so insoluble.

Certain water soluble molecules repel each other strongly, in contrast to the attraction of hydrophobic groups, preferring contact with water than each other. The hydrophobic and hydrophilic interactions are not additive, and are interdependent. It is expected that they are interdependent as both rely on the structure of the water hydrogen bonding around the dissolved groups.

1.3.2 Aggregation

At low concentrations, surfactants dissolved in water are simply suspended in water, with some molecules located at the water/air interface, with the head groups on the water surface, and the tail groups pointing upwards, avoiding contact with the water. The interactions between head groups and water molecules are weaker than the inter water interactions, so the surface tension is reduced.

As the concentration of surfactant is increased, a certain concentration is reached where a sufficient number of surfactant molecules are present in water to facilitate self-assembly. This is where the molecules aggregate (normally as spherical molecules) with tail groups in the centre, and head groups surrounding the surface of the sphere, “shielding” the oily chains from contact with water (see Figure 1.4).

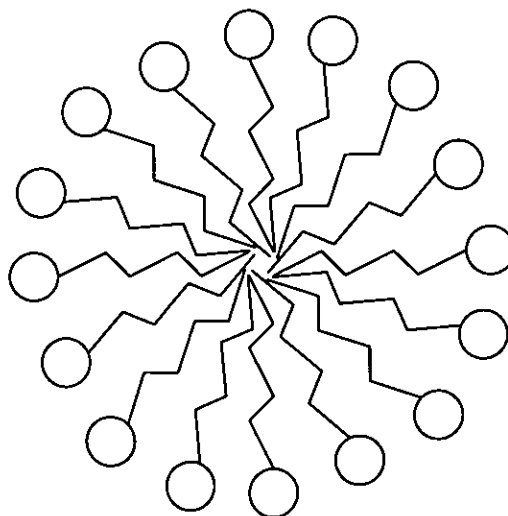


Figure 1.4 A spherical micelle, upon aggregation above the critical micelle concentration (CMC)

Equilibrium thermodynamics requires that in a system of molecules that form aggregated structures in solution, the chemical potential of all identical molecules in different aggregates is the same, so

$$\mu = \mu_N = \mu_N^0 + \frac{kT}{N} \log\left(\frac{X_N}{N}\right) = \text{constant} \quad (1.2)$$

where μ_N is the mean chemical potential of a molecule in an aggregate of aggregation number N , μ_N^0 is the standard part of the chemical potential (the mean interaction free energy per molecule) in aggregates of aggregation number N and X_N is the concentration of molecules in aggregates of aggregation number N .

Aggregates only form when there is a difference between the cohesive energies of the molecules in the aggregated and the dispersed (monomer) states. Therefore the necessary condition for the formation of large aggregates is that μ_N^0 is smaller than the chemical potential of an isolated molecule, μ_1^0 , where μ_N^0 decreases as N increases, or has a minimum at some finite aggregation number N . (If there is no minimum point, then very large aggregates are the result, causing phase separation.) The exact $\mu_N^0 \nu N$ relationship determines many physical properties of aggregates. Many molecules will have a peak at more than one N value.

1.3.3 Critical Micelle Concentration

At the critical micelle concentration (CMC), micelles form spontaneously. Micelles spontaneously and dynamically aggregate and disperse from amphiphiles, having a lifetime of approximately 1ms. The CMC is a conflict between two opposing forces. The hydrophilic chains try to minimise their contact with water, resulting in micelle formation, but as head groups are placed closer together, repulsive forces between the head groups oppose micelle formation.

The CMC is temperature dependent, with its value increasing with increasing temperature. This is because of the solubility of the surfactant in a solvent, which also increases (at a much higher rate) with increasing temperature (see Figure 1.5). The temperature where the CMC and the solubility curve intersect is known as the Kraft temperature. Below this, surfactants form hydrated crystals, but above it they form a variety of liquid crystal phases, given a supercritical micelle concentration. The formation of micelles occurs only when the temperature is above the Kraft temperature and the concentration is above the CMC^[7,8].

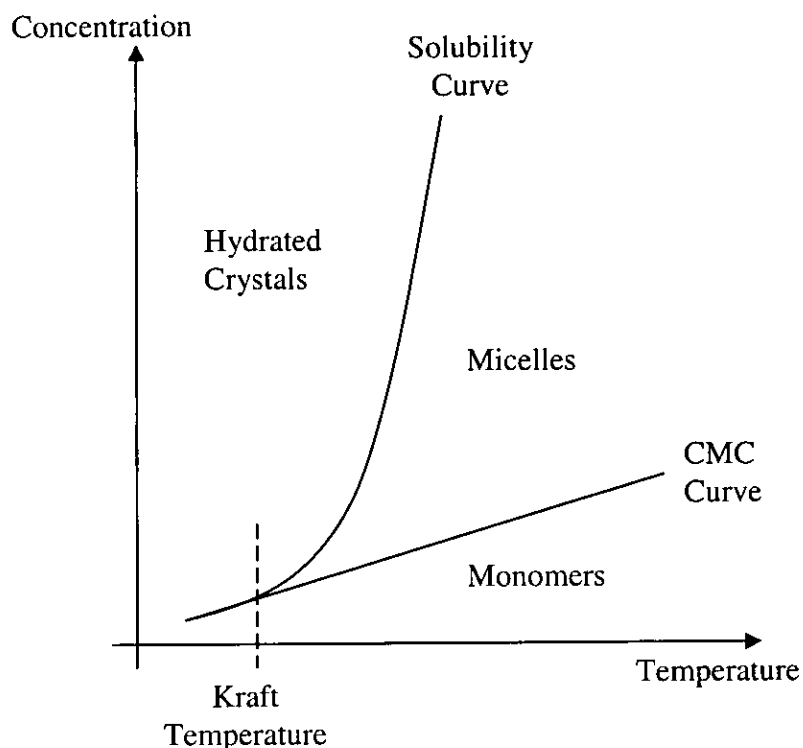


Figure 1.5 Sketch showing how solubility and CMC affect micelle formation

1.4 Phases

1.4.1 Geometry of Aggregates

Lytropic phases are identified by optical microscopy and x-ray scattering. They are characterised by the curvature of the interfacial region between hydrophilic and hydrophobic entities. The anisometric unit of lyotropic phases is a group of molecules, for example a micelle. A diagram showing the tail-head group and water interface in an aggregate of amphiphiles in solution is shown in Figure 1.6. The geometry of the aggregates depends on the dimensions of the surfactant (its headgroup surface area, chain length, etc), the curvature of the interface of the aggregate and the inter-aggregate forces.

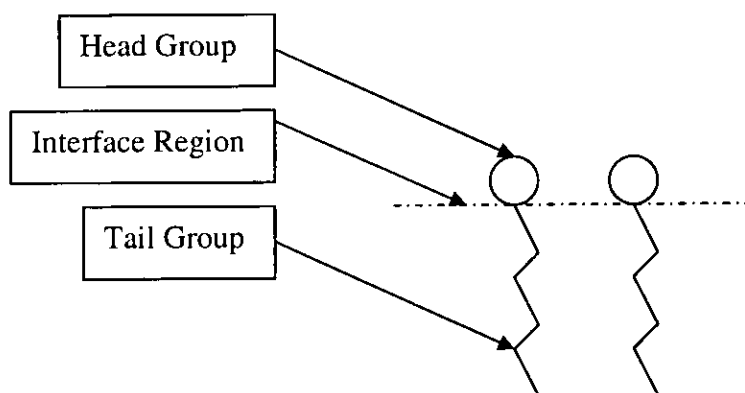


Figure 1.6 The interfacial region of an aggregation of amphiphiles

A given amphiphile under certain conditions will have a certain head group area. This arises from a hydrophobic attraction of the chain molecules and a repulsive hydrophilic interaction between the headgroups. These opposing forces lead to an optimal headgroup area. Together with the length and volume of the hydrocarbon chain of the amphiphile, these three parameters can be used to define the surfactant parameter, N_s [9]. This is defined as:

$$N_s = v/(S_a l_c) \quad (1.3)$$

Where v is the volume of the hydrocarbon chain, S_a is the effective surface area per headgroup molecule, and l_c is a semiempirical parameter representing the maximum length above which the chain is no longer considered to be a fluid. These three parameters can be satisfied by a variety of different structures. It has been shown by [10] that the value of the surfactant parameter will determine the type of aggregate they will form:

$N_s < 1/3$	Spherical micelles
$1/3 < N_s < 1/2$	Non-spherical micelles or cylinders
$1/2 < N_s < 1$	Vesicles or bilayers
$N_s > 1$	Inverted structures

These correspond to minimum-sized aggregates in which all lipids have minimum free energy. The surfactant parameter is also a measure of interfacial curvature.

There are two additional contributions to the energy of the interface that will affect the curvature of the aggregate. One is a headgroup repulsion, acting at some distance above the interface. The nature of this force is described later. The second is the chain repulsion, which arises from a restriction in chain freedom in bilayers, and acts inside the chain region, a certain distance below the interface. ($l_c \approx l_{max}$ for spheres and cylinders, but for bilayers, $l_c \approx 0.7l_{max}$.) These effects result in an additional curvature dependence of μ_N^0 . If head group repulsion dominates, curvature tends to increase, if chain repulsion dominates, curvature tends to decrease.

Another approach to analysing aggregate structures uses the curvature of the surface. The mean curvature H at a point on the surface as:

$$H = \frac{1}{2} \left(\frac{1}{R_1} + \frac{1}{R_2} \right) \quad (1.4)$$

where R_1 and R_2 are the radii of curvature in two perpendicular directions. Figure 1.7 shows how the radii of curvature are taken from a surface. For a sphere, $R_1 = R_2$, so $H = 1/R$. For a cylinder, $R_1 = R$ and $R_2 = \infty$ so $H = 1/2$. For a planar bilayer, $H=0$. H can also be zero on a saddle surface, where $R_1 = -R_2$.

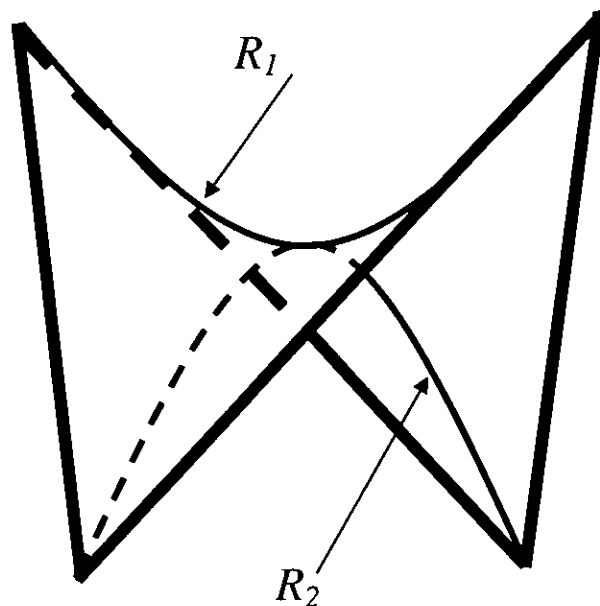


Figure 1.7 Mean curvature is measured by taking the radius of curvature in two perpendicular directions.

There are numerous phase structures that may occur, but within one system only a few of these will occur. These may be categorised into classical phases, that occur frequently, and intermediate phases, that occur between the most common phases.

Before the different phases are discussed, it is useful to introduce the different forces that occur between surfaces in liquids. Both intra and inter aggregate interactions affect the phase structure. In concentrated solutions, it is the interaggregate interactions that tend to dictate the structure of the phases. Increasing the concentration causes the amount of interface to decrease along with curvature and also minimises interfacial separation. Therefore increasing the concentration from spherical micelles, the aggregate surfaces are closer together, which is energetically unfavourable. If cylinders form, the surfaces are further away. If bilayers form, the surfaces are even further away. These phase transitions arise from the repulsive forces between inter-aggregate surfaces. The four main forces between surfaces in liquids are van der Waals, electrostatic, solvation (hydration) and steric forces. Attractive van der Waals forces between surfaces are weak. Electrostatic double layer repulsive forces arise if the headgroup has an ionic charge, and are sensitive to pH, concentration of electrolyte and potential changes. As hydrophilic surfaces approach one another, the water molecules bound to the surface dehydrate. Because of the energy required to dehydrate the surface, a repulsive force arises, known as the hydration force. The headgroups are considered to be 'rough' on the same scale as water, and the headgroups are thermally mobile so steric repulsion is also taking place. It is hard to distinguish between these two interactions, and the surfaces are not well defined. These hydration forces dominate the van der Waals and double layer forces at small separations. Finally, steric forces occur at surfaces. These are made up of protrusion, undulation, peristaltic and headgroup overlap forces. Of these, only the undulation force is expected to have a long range, which may exceed the length of the of the amphiphilic molecule, and the other forces will decay beyond the length of a molecule. Protrusion forces occur when the surfaces are so close that molecular-scale protrusions overlap. Undulation and peristaltic forces occur as a result of thermal fluctuations at a macroscopic level. Undulatory forces are associated with a bending of the surfaces, and peristaltic forces are associated with a squeezing of the surface, where the thickness of the membrane fluctuates locally about a mean thickness, with no bending. These are both repulsive forces, arising from the entropic confinement of their undulation and peristaltic waves as two surfaces approach each other. The head

group overlap force is a type of steric interaction and occurs when two polymer-covered surfaces approach each other, and the outer constituents begin to overlap. This interaction usually leads to a repulsive osmotic force due to the unfavourable entropy associated with compressing the chains between the surfaces.

1.4.2 Classical Phases

The three most common shapes that amphiphiles can aggregate into are spherical micelles, cylindrical rods or flat layers. These phases are known as micellar, hexagonal and lamellar respectively (Figure 1.8).

Two phases may be constructed from micelles. The first is a micellar phase, which is isotropic, since it does not possess any long range order. The second is the micellar cubic phase which consists of slightly elongated micelles arranged in a body centred cubic fashion (Figure 1.9). This is also isotropic, but this is considered to be a colloid crystal phase as it has long-range order, because of the arrangement of the micelles.

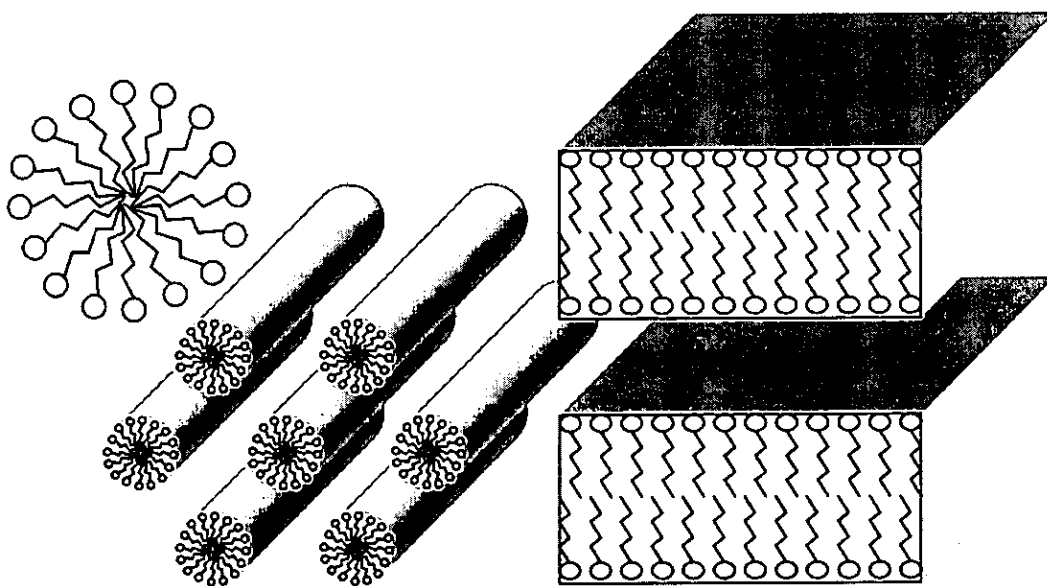


Figure 1.8 From left to right, spherical micelles, the hexagonal and lamellar phases.

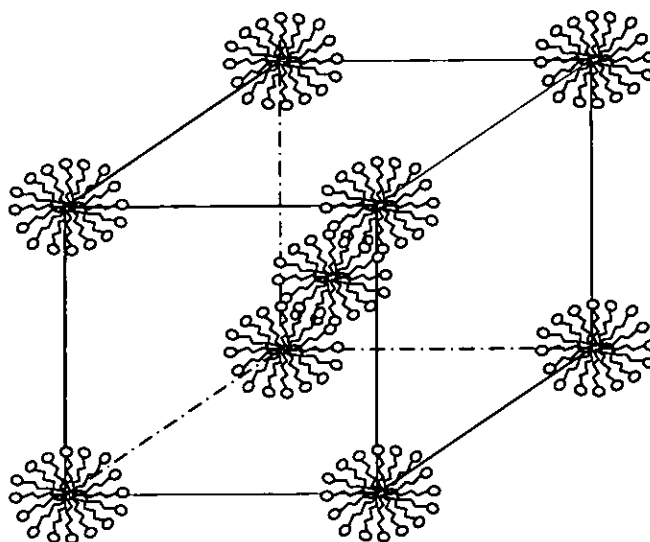


Figure 1.9 The micellar cubic phase, with slightly elongated micelles packed in a body centred cubic arrangement.

The hexagonal phase is made up of cylindrical rods of surfactant of indefinite length arranged hexagonally in a 2-D array, with water in between. This phase is birefringent due to its anisotropy, and is very viscous.

The lamellar phase consists of stacked bilayers. (A bilayer is a region of surfactant that has a thickness of two alkyl chain groups.) The distance between consecutive bilayers depends on the concentration of surfactant and water.

Reversed phases of isotropic and hexagonal phases are possible, where the spheres or rods are the water regions instead of the alkyl chain region (Figure 1.10).

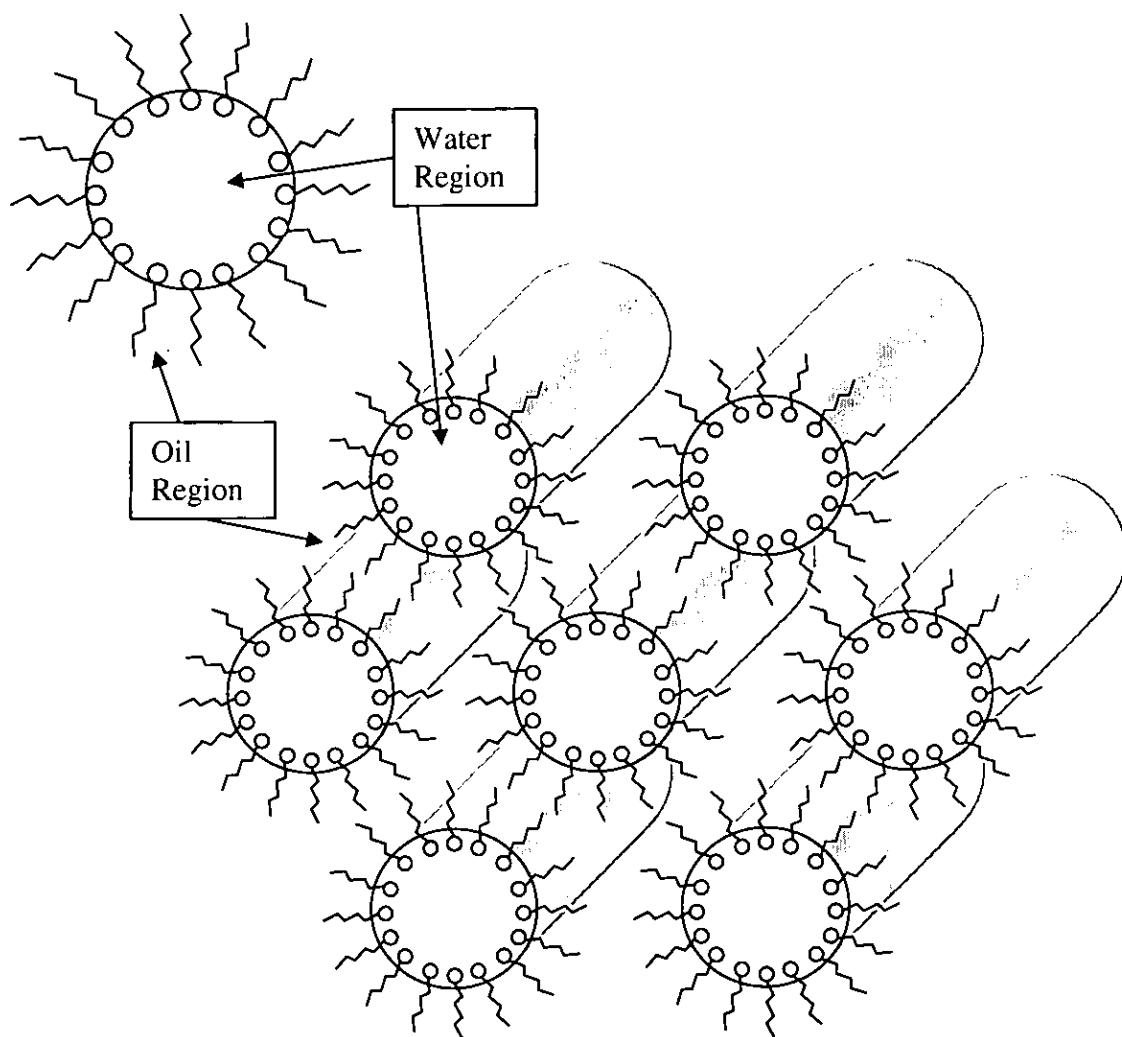


Figure 1.10 From left to right, the inverted micellar phase and inverted hexagonal phase.

One final type of the standard phases is the bicontinuous cubic phase. This is a phase where both the surfactant and water regions exist as continuous parts, connected to infinity. There are three possible space groups for this phase, and these are pictured in Figure 1.11. Because of the interlocking nature of the structures, no shear movement can occur without disrupting the phase, making this phase highly viscous. This phase is isotropic. Space groups $Ia3d$ ^[11] and $Pn3m$ ^[12] are the most common, and act as models to biological membranes^[13,14]. The $Im3m$ ^[15] space group is quite rare.

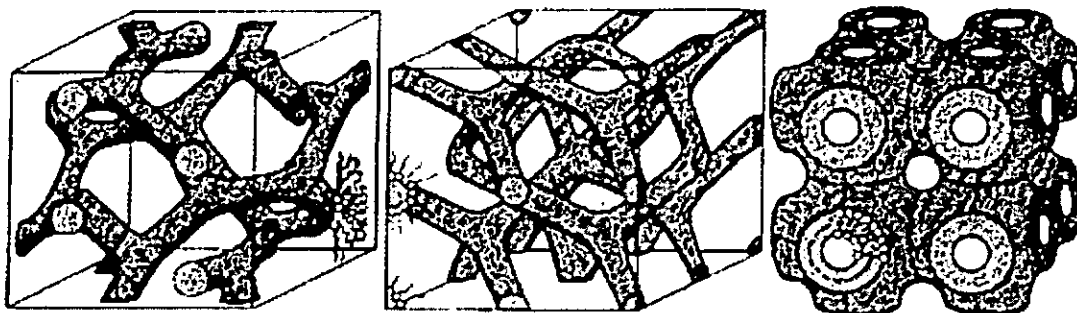


Figure 1.11 Bicontinuous Cubic phases, showing the $Ia3d$, $Pm3m$ and $Im3m$ space groups from left to right^[16].

1.4.3 Intermediate

Intermediate phases are those that occur between the hexagonal and lamellar phase, where the bicontinuous cubic phase is expected^[17]. The intermediate phases can be categorised into 3 broad types, ribbon^[18,19], mesh^[20] and bicontinuous (non-cubic). In some ways, these types may be considered to be related to the following standard phases respectively: hexagonal, lamellar and bicontinuous cubic. None of these three types have a constant interfacial curvature, unlike the standard phases. Bicontinuous non-cubic intermediate phases have only been hypothesised^[20].

The ribbon phases are very similar to the hexagonal phase, only with elliptical cylinders instead of circular ones. The ribbon phase has two possible space groups, pictured in Figure 1.12. The long dimension of the ellipsoid will decrease with decreasing temperature, forming the hexagonal phase^[20]. A typical phase sequence would be hexagonal to ribbon to lamellar.

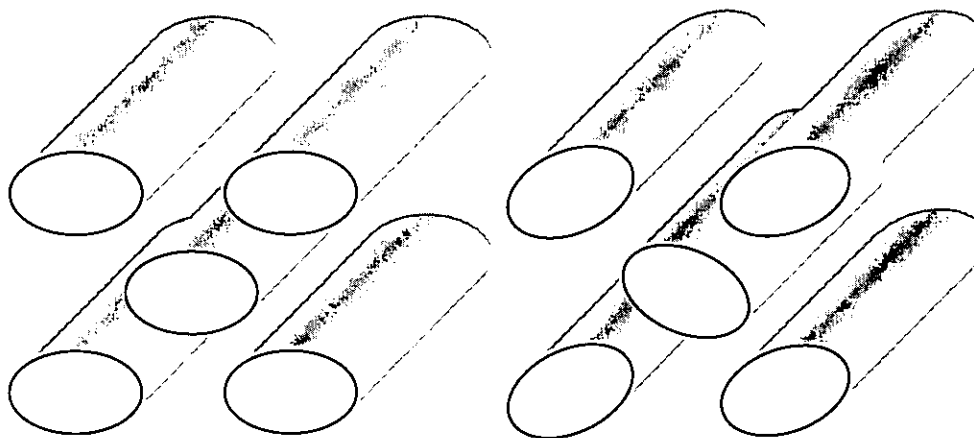


Figure 1.12 The Ribbon Phases, showing the $c2mm$ and $p2gg$ space groups from left to right

There are three different mesh phases. One of them is the random mesh phase, which is the lamellar phase with water filled defects or pores^[21]. These pores have no

correlation with each other. The other two types do have correlation. These are the rhombohedral and the tetragonal mesh phases ^[19,22]. The rhombohedral phase is a three connected mesh structure, stacked in an ABC manner. The tetragonal mesh structure is less common, but has been found by Kekicheff and Tiddy ^[23]. Figure 1.13 shows a diagram of the intermediate mesh phase.

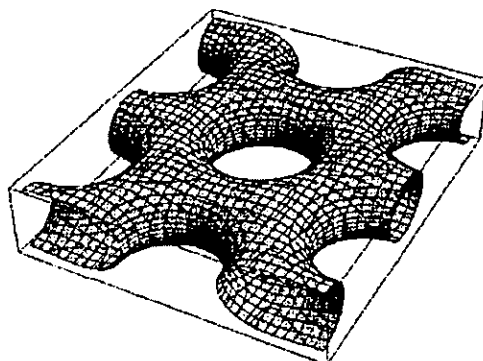


Figure 1.13 The mesh phase. The rhombohedral mesh phase is a three connected structure with monodisperse pores stacked in an ABC fashion. The random mesh phase has pores with distribution in size and there is no correlation between layers.

A sponge like phase is another bilayer-based phase, occurring most often next to a swollen lamellar phase at low surfactant concentrations ^[5,24-27], as well as rich in oil. The sponge phase is a liquid-like disordered phase, consisting of 3D multiply connected bilayers, with negative monolayer curvature ^[28-30]. A sponge phase is shown in Figure 1.14.

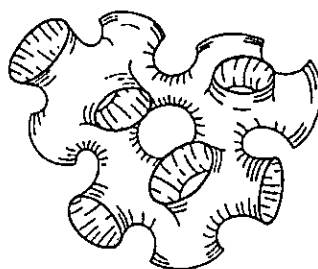


Figure 1.14 Schematic representation of the sponge phase ^[28]

1.4.4 Nomenclature

The notation of phases utilised is the same as in ^[20], where a uniform system has been adopted. L, I, H, V and L_α refer to the micellar isotropic, micellar cubic, hexagonal, bicontinuous cubic and lamellar phases respectively. The suffixes to these letters refer to the normal phase (1) and inversed phase (2). L_3 refers to the sponge phase. Rb, Mh and Bc are used for the ribbon, mesh and bicontinuous cubic phases respectively, with space groups ^[31] appended in brackets, as in V_1 (Ia3d) for the bicontinuous cubic

phase with an Ia3d space group. Space groups provide a mathematical description of the symmetry inherent in a structure.

1.4.5 Diagrams

Phase diagrams show the possible phases of a system under given conditions. For a surfactant-water system, the most important factors in determining the phase of a liquid crystal are the concentration and temperature. Therefore, two dimensional diagrams are required to show which areas belong to which phases, with the lines in between representing the phase boundaries. The abscissa of the phase diagram is concentration, whilst the ordinate is temperature. To help understand the constraints on phase diagrams, the Gibbs Phase Rule is introduced ^[9]. The equation of state for a one component system is $F(V,n,p,T)=0$. An example of this is the ideal gas equation where $(pV/nRT)-1=0$. Three independent variables, from the temperature T , pressure p , volume V and number of moles n , give the equilibrium state. Therefore, $\rho=f_{\rho}(n,p,T)$. As $\rho=n/V$, we can write $\rho=f_{\rho}(n,p,T)=f_{\rho}(p,T)$, where one intensive quality of a system (in this case density) is a function of two intensive variables (pressure and temperature in this case). The intensive variables are independent of the size of the system. All intensive qualities in a one component system are a function of two intensive variables.

F , the number of degrees of freedom, is the number of independent intensive variables that remain after possible constraints are taken into account. For a one component system with no other constraints, $F=2$. If there are two phases P , α and β and they are at equilibrium, $F=1$ as T and p are no longer independent. For a two component system, another intensive variable is added, the mole fraction of the second component. Therefore $F=3$ if there are no other constraints. These observations are generalised to enable them to be applied to systems with any number of components C , and the result is a relation known as the Gibbs Phase Rule:

$$F+P=C+2 \quad (1.5)$$

Figure 1.15 shows a typical phase diagram, showing standard and intermediate phases and boundaries, and in the location and shape that they are likely to occur, but for most surfactants not all of these phases would appear for one system. For ionic systems, the phases are largely insensitive to temperature, so the phase boundaries are

mostly vertical, however for non-ionic systems, the phases are quite sensitive to temperature due to the dehydration of the ethylene oxide head groups at higher temperatures, so the phase boundaries are mostly horizontal [17,18]. Some regions are biphasic, where two different liquid crystal phases coexist. If the mixture's concentration and temperature is such that it lies on a phase boundary, then both of the phases either side of the line are present in the sample. If the mixture lies on an intersection of three phases, then three phases will coexist. At a low concentration, a water rich phase will be present just above the CMC, shown as w in Figure 1.15. H_1 , H_2 , L_1 and L_α represent the hexagonal, inverted hexagonal, micellar and lamellar phases respectively. In between the hexagonal and lamellar phases, a cubic or intermediate mesh phase may form. At high surfactant concentration, a surfactant rich region occurs such as a liquid surfactant containing some water, or a solid gel phase for surfactants with longer chains. This region is labelled x .

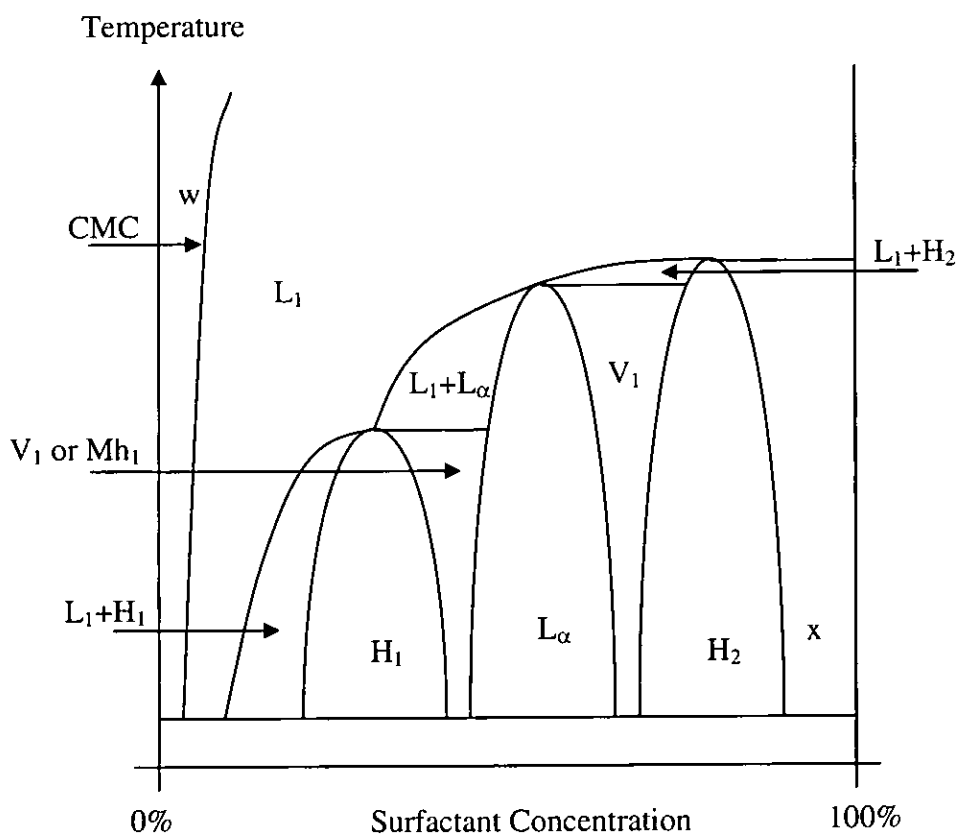


Figure 1.15 A (simplified) typical phase diagram (not all phases would be present for any one system). Water rich and surfactant rich regions are denoted by w and x respectively.

In general, all phases are thermodynamically stable, and the same phase sequence is observed upon heating and cooling for a sample of fixed concentration, but some systems have been noted to have a slightly different phase sequence depending on the thermodynamic history of the sample, giving rise to metastable phases. One such example of this is the rhombohedral mesh phase in the $C_{16}E_6$ /water system, which will be discussed later.

1.5 Previous Work

1.5.1 Binary Systems

A detailed study on the $C_{16}E_6$ /water system was carried out by Fairhurst et al ^[19,32]. This work produced a phase diagram of the system, and identified the phase sequences upon heating and cooling. Significantly, these phase sequences on heating and cooling differed. Upon cooling, the rhombohedral mesh phase formed from the random mesh phase, instead of the bicontinuous phase that formed in that region on heating from the hexagonal and gel biphasic region. Figure 1.16 shows phase diagrams of the $C_{16}E_6$ /water mixture upon cooling (left) and heating (right). It was concluded that the interlayer correlation in the rhombohedral mesh phase arose from the head group overlap forces between each bilayer (see section 1.4.1). This caused the mesh layers to stack in an ABC arrangement, allowing the furthest separation between head groups of different layers, which is most energetically favourable given the head-group overlap forces.

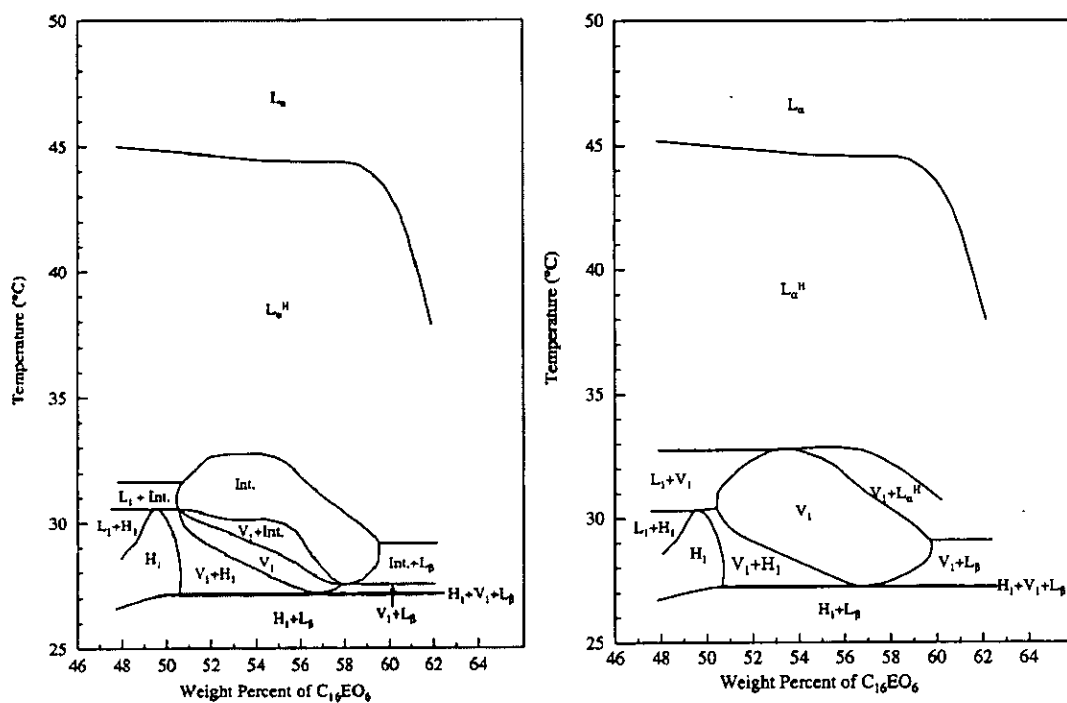


Figure 1.16 Phase diagram upon cooling (left) and heating (right) for $C_{16}E_6$ from reference ^[19]

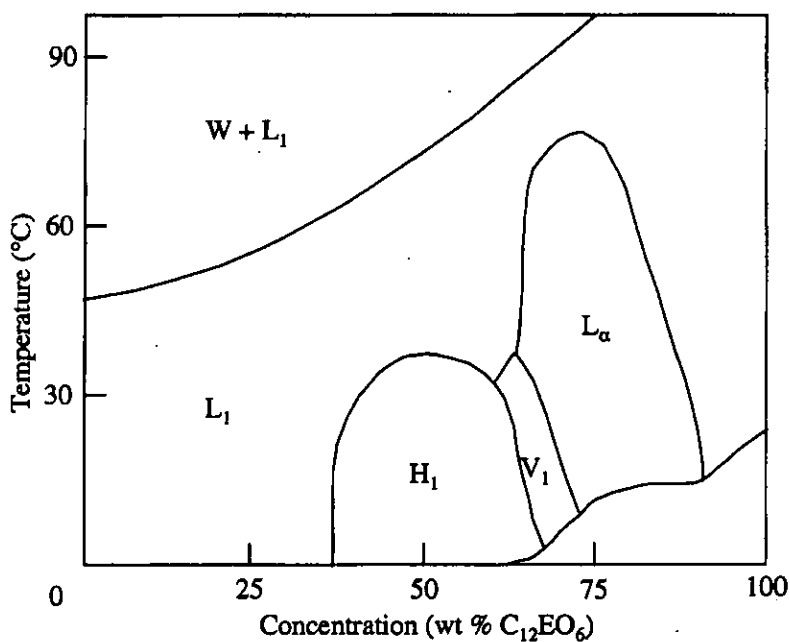


Figure 1.17 Phase diagram for $C_{12}E_6$, taken from reference ^[33].

One of the first important works on non-ionic polyoxyethylene surfactants was by Mitchell et al ^[24]. This research identified the phase behaviour of a large range of these surfactants, including $C_{12}E_6$, $C_{14}E_6$ and $C_{16}E_6$. A phase diagram of $C_{12}E_6$ was shown, taken from ^[33], and is reproduced in Figure 1.17. This phase diagram shows

that between 60% and 70% by weight of surfactant, the phase sequence is: hexagonal; cubic; lamellar. The paper also hypothesised that as the temperature of a mixture decreases for a non-ionic polyoxyethylene surfactant, the head-groups become more hydrated, and as a result each head group has a larger effective surface area. This is likely to be the phenomenon that drives phase changes.

1.5.2 Intermediate Phases

Some work has been carried out on ionic surfactants that exhibit the intermediate mesh phase. Luzzati et al were working on anhydrous soaps of divalent cations of group II when they discovered two novel phases ^[34]. Using data obtained from SAXS, they found sharp reflections corresponding to the space groups $R\bar{3}m$ and $I422$. These have rhombohedral and tetragonal symmetries respectively, and were given 3 and 4 connected mesh structures respectively. Another tetragonal phase was discovered by Kékicheff and Tiddy, working on LiPFO ^[23]. A phase diagram was produced showing an intermediate phase occurring between 70-75% by weight LiPFO for temperatures between 20-30°C. The intermediate phase was established by identifying reflections from SAXS data and optical microscopy, exhibiting a parabolic focal conic (PFC) texture. A model of the tetragonal mesh phase was made consisting of cylindrical rods connected with cuboids. The model made with the same volume fraction as experimentally showed a good correlation with the lengths of the alkyl chains, showing that the proposed structure fits well with the dimensions of the phase. It was suggested that as the tetragonal phase has both positive and negative surface curvature, the phase is more of an intermediate phase between the lamellar and bicontinuous cubic phases than the lamellar and hexagonal phases. It was also speculated that the low concentration boundary of the tetragonal phase is where the separation between the layers is too large to sustain the ordering of pores between layers, and the high concentration boundary of the phase is due to the area of the water filled defects being too small for the tetragonal phase to form.

Puntambekar et al ^[35] observed large regions of intermediate phase while studying an ionic fluorocarbon surfactant/water system. This included an immense region of the random mesh phase and a large rhombohedral mesh phase region. The other phase present in this system is a lyotropic nematic phase, consisting of disc-shaped micelles, so therefore all of the phases present have non uniform curvature. The ratio of the lattice parameters for the rhombohedral phase is consistent with those obtained from

other rhombohedral phases in other systems, indicating that there may be some universality of the structure. Kékicheff and Cabane ^[36] reported four intermediate phases in between the hexagonal and lamellar phases in the SDS/water system. The phase sequence is: hexagonal; 2-D monoclinic; rhombohedral; bicontinuous cubic; tetragonal mesh; lamellar. The dimensions of the lattice parameters for each phase change in a reasonably continuous fashion. Blackmore and Tiddy ^[37] tried penetration scans for a variety of cationic surfactants, finding that increasing the alkyl chain length destabilises the bicontinuous cubic phase in favour of the intermediate phase. Lengthening the alkyl chain will increase the electrostatic forces in addition to decreasing the flexibility of the chain. Lengthening the chain moves the interfacial surface away from the surface of mean curvature and destabilises the system. Some ribbon intermediate phases were also found in some of the cationic surfactants studied.

Henriksson et al ^[38] studied the intermediate phases present in the $C_{16}TACl$ /water system, finding the phase sequence: hexagonal; ribbon; rhombohedral mesh; bicontinuous cubic; tetragonal mesh; lamellar. The 2H NMR Quadrupolar splitting is lower for the rhombohedral phase than that of the hexagonal phase, as expected for a rhombohedral structure. Holmes et al ^[39] carried out a study on CsPFO, finding that there is a random mesh phase present. It was suggested that this structure has ribbon like water filled defects in the lamellae, which are uncorrelated between the layers. The change between the discotic nematic phase and the random mesh phase is said to be driven by a decrease in surface curvature at lower temperatures, favouring the mesh phase.

Much work has also been carried out on non-ionic surfactant systems. Funari et al ^[40] investigated $C_{22}E_6$, finding the random mesh phase. This acted as an intermediary phase between the lamellar and hexagonal phases with no other intermediary phases present. The presence of the random mesh phase over the cubic phase is attributed to decreased alkyl chain flexibility. The onset of the random mesh phase from the lamellar phase was marked by a first order transition. Three models were suggested for the structure of the water filled defects, ribbons, disks and holes, although all models fitted well with the experimental results. Burgoyne et al ^[14] carried out research on the long chain non-ionic surfactant $C_{30}E_9$. An intermediate phase was found which was suggested to be a rhombohedral phase. This paper addressed the question of whether its structure was either a three or six connected mesh structure.

The $R\bar{3}m$ space group allowed both structures. These structures are stacked in an ABC (three connected) and an ABAB (six connected) stacking fashion. Primitive rod and box models were designed for both rhombohedral structures in order to calculate geometrically structural dimensions. An incorrect SAXS indexing led to the belief that the six connected structure matched theoretical figures, despite the high surface curvature that the six connected structure possessed. Leaver et al ^[41] continued these experiments on both the $C_{16}E_6$ and $C_{30}E_9$ systems and carried out more thorough structural models for the $R\bar{3}m$ intermediate mesh phase. After re-indexing the scattering data from SAXS and calculating the appropriate cell dimensions, it was found that the three connected mesh structure was favoured over the six connected structure. It was also discussed in this study that the longer the alkyl chain, the more stable the intermediate phase over the cubic phase, as explained above. It was suggested in this study that as the rhombohedral mesh phase is not a minimal surface structure like the cubic phase is, then longer, stiffer chains will move the surfactant-water interface further from the minimal surface to a point where a mesh phase becomes the more energetically stable phase. In a later study ^[13] $C_{30}E_9$ was shear aligned and brought into the intermediate phase, where SAXS measurements were carried out. The structure was once again found to have a rhombohedral symmetry with a space group of $R\bar{3}m$. The transition from the hexagonal to rhombohedral mesh phase was discussed, and it was suggested that the transition was due to the balance of the head group overlap forces and the decreasing surface area per head-group due to the dehydrating of the head-groups at higher temperatures. It was proposed that the transition from the hexagonal phase forms from the modulation of the cylinders equal to the node separation in the rhombohedral mesh phase, and subsequent connections between cylinders to form the mesh structure. Another polyoxyethylene non-ionic surfactant $C_{16}E_6$ has also been the subject of much research. This surfactant is different in that it has a meta-stable rhombohedral mesh phase. Funari et al ^[42] delineated a phase diagram showing a cubic phase on heating and an intermediate phase on cooling. This phase reverts back to the cubic phase if left at a constant temperature for a period of time, showing that the cubic phase is more stable here than the intermediate phase. Fairhurst et al ^[32] continued investigation upon the surfactant by producing a detailed phase diagram in the intermediate phase region. The cubic phase was attributed the space group $Ia3d$, and the intermediate phase was confirmed

to have a layered mesh structure due to its parabolic focal conic texture, and a rhombohedral structure due to the nature of its SAXS results. The random mesh phase was assumed to consist of a flat bilayer with uncorrelated water filled defects. The formation of the rhombohedral phase from the random mesh phase takes place with little change in quadrupolar splitting or layer spacing, indicating that the phase transition is due to the onset of long range order of the defects. It is expected that the epitaxy of the mesh phases and the lamellar phase share the same $(00l)$ plane, but the epitaxy between the intermediate and cubic phases remains as yet unknown. Three models were suggested for the rhombohedral phase, rod-box, simple rod and minimal surface curvature models. All of these fitted well with the experimental results. A decrease in concentration in the intermediate phase did not affect the size of the nodes, it just served to lengthen the connecting rods, and increase the interlayer separation. Models were also formed for the bicontinuous cubic phase, and transitions between the two phases were discussed, and the hexagonal to rhombohedral mesh phase transition was also discussed, where it was found that the bicontinuous cubic and mesh phases differ little in their optimum structures. The head group overlap force is reported to cause a puckering between the layers in the rhombohedral mesh phase.

Much work has also been carried out on diblock copolymers. Amphiphilic diblock copolymers can be amphiphilic, exhibiting surfactant like properties. These can be seen as surfactant molecules with longer chains. Diblock copolymers exhibit phase structures in aqueous solution or even in just a diblock copolymer melt. These phase structures are remarkably similar to those encountered in traditional surfactant systems, and much work has been done not only experimentally, but also theoretically, where models have helped the understanding of the phases and their transitions. Laradji et al ^[43] considered the stability of the ordered phases in diblock copolymer systems using a theory of anisotropic fluctuations, within a mean field theory simulation. It was found that upon cooling from the lamellar phase to the hexagonal phase, an unstable intermediate phase forms. This begins as a lamellar phase with an undulated surface, which grows into a rhombohedral mesh phase, forming from a nucleation and growth mechanism. This is an unstable phase and upon heating from the hexagonal phase, the lamellar phase forms with no intermediary mesh phase. This is equivalent to the $C_{16}E_6$ system, where a cubic phase forms on heating instead of having no intermediary phase in the diblock copolymer system.

Chastek and Lodge ^[44] studied the transition between the bicontinuous cubic phase from the mesh phase. This transition occurs after leaving the mesh phase at a constant temperature, showing that the bicontinuous cubic phase is more stable than the mesh phase for this diblock copolymer system. One transition took around 20 minutes, but this time varies depending on the temperature and concentration of the sample. The growth of the bicontinuous cubic phase from the mesh phase occurs isotropically from grains that grow at a constant velocity. A similar study by Hamley et al ^[45] looked at the transition between the lamellar and the bicontinuous cubic phases. The average composition for the diblock copolymer used was $\text{CH}_3\text{OE}_2(\text{dE})_{18}\text{B}_{10}$. SAXS and SANS (small angle x-ray/neutron scattering) were performed, and the results showed that again, the intermediate mesh phase occurs. From the lamellar phase, defects appear first in a random fashion before packing in in a hexagonally closed pack way. On heating from the bicontinuous cubic phase to the lamellar phase, no mesh phase was observed. Also the mesh phase left at a constant temperature reverted back to the more stable bicontinuous cubic phase. The Self Consistent Field Theory ^[46] was used to model the situation. This model showed the epitaxy of the lamellar mesh and bicontinuous cubic phases. Work using Monte Carlo simulations revealed that the mesh phase occurred first with randomly ordered defects that gradually order hexagonally. These findings were consistent with the results from SAXS and SANS.

1.5.3 The addition of oil

Oil may be added to the surfactant/water binary system to form a ternary system. These ternary systems, although historically regarded as thermodynamically unstable, have shown to be thermodynamically stable ^[47]. The hydrocarbon chains of the oil will be subject to the hydrophobic effect, as will the alkyl tail group. Therefore, the oil molecules will aggregate within the tail group of the liquid crystal. It is possible to form most of the binary lyotropic phases in ternary systems with added oil, although the phases have a certain tolerance to the addition of oil. Ninham *et al* showed that for ionic surfactants, microemulsions are formed at lower water content depending on the nature of the oil ^[48]. In this research, it was proposed that for oils with hydrocarbon chain lengths shorter than that of the surfactant, such as hexane, the oils would be able to reside in the region between the surfactant chains. These oils were named penetrating oils. In the lamellar phase, the addition of a penetrating oil does not greatly affect the thickness of the bilayer, but the oil increases the spaces between the

surfactant molecules, so the effective surface area per head group is increased ^[49]. Figure 1.18 shows a ternary system in the lamellar phase with a penetrating oil. Oils with chain lengths greater than that of the surfactant tail, cannot penetrate between the surfactant chains, reside in the inter layer region, thickening the bilayer. These oils are termed swelling oils. In the lamellar phase, swelling oils do not change the effective surface area per head group, but increase the height of each bilayer ^[49]. Figure 1.19 shows a ternary system in the lamellar phase with a swelling oil.

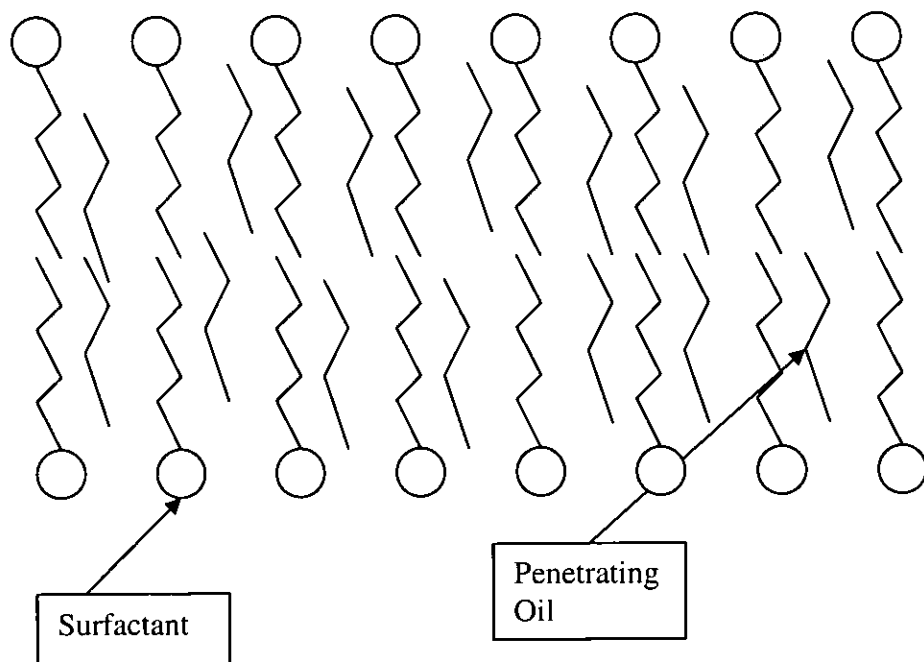


Figure 1.18 A penetrating oil, shorter than the alkyl chain of the surfactant.

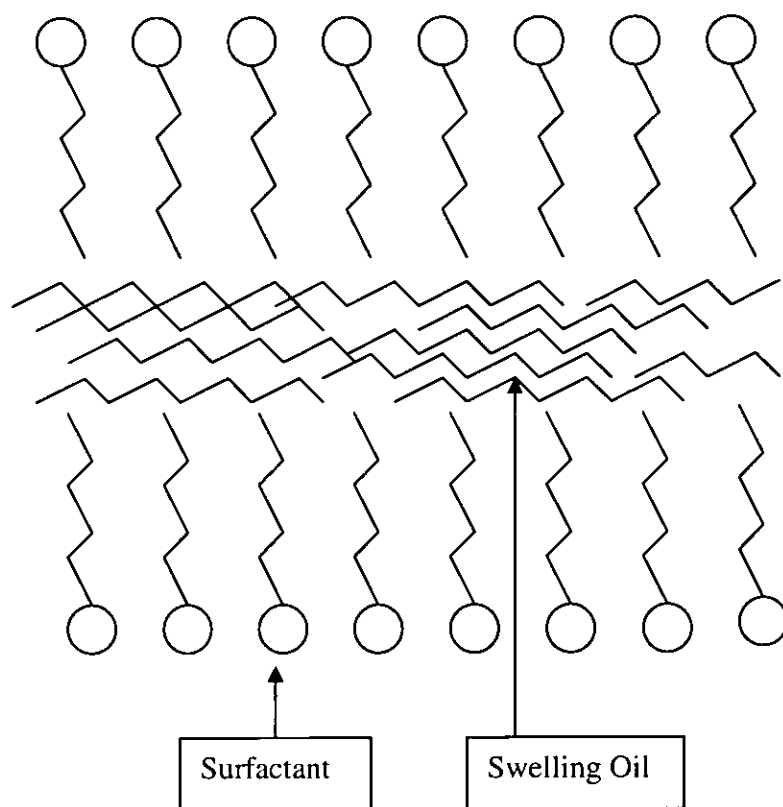


Figure 1.19 A swelling oil, longer than the alkyl chain of the surfactant.

The addition of oil into surfactant/water mixtures affects the formation of phases. Therefore, for a sample of a particular concentration, the phase sequence of a sample observed with oil upon heating will show phase transitions at temperatures lower than that of the equivalent binary system^[19]. This is because the addition of oil serves to increase the amount of alkyl chain region in relation to the head group region, reducing the mean curvature, inducing phases with a lower interfacial curvature^[49].

Wang investigated the effect of adding polymers to the $C_{16}E_6$ /water mixture. The behaviour of penetrating and swelling oils was investigated, and how it affected the phases^[49]. It was found that with increasing concentrations of oil added, irrespective of type, phases were destabilised at increasingly lower temperatures. This is because adding oil at a fixed alkyl chain volume fraction serves to decrease the mean interfacial curvature, resulting in the loss of phases with a high mean curvature, in favour of the lamellar phase, which has no curvature. When sufficient amounts of oil are added, even the lamellar phase is destabilised, and the system phase separates. It was also found that the addition of hexane increases the effective surface area per head group, as shown by NMR analysis.

This shows that hexene acts as a good penetrating oil. There is no significant change in either the surface area or Δv , for the addition of octadecane, showing that it acts as a good swelling oil. Figure 1.20 shows a phase diagram for the addition of oil to a $C_{16}E_6$ -water mixture.

Swelling and penetrating behaviour was also observed by Kunieda et al ^[28,50], where decane, *m*-xylene or squalene was mixed with $C_{12}E_n$, where *n*, the length of the head group, was varied. Decane acted as a swelling oil for both $C_{12}E_3$ and $C_{12}E_7$ surfactants, where the transitions L_a - H_2 and H_1 - I_1 were observed for $C_{12}E_3$ and $C_{12}E_7$ respectively.

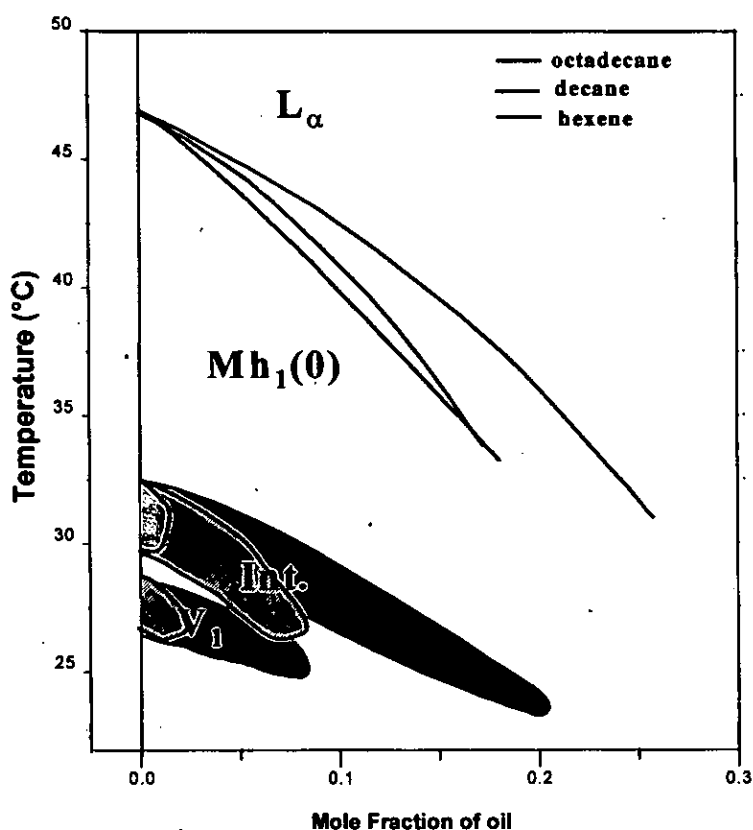


Figure 1.20 Phase diagram for addition of oils to $C_{16}EO_6$ -water mixture, taken from reference ^[49]. $C_{16}E_6$ /water/*l*-hexene (red), $C_{16}E_6$ /water/*n*-decane (blue) and $C_{16}E_6$ /water/*n*-octadecane (green), all on cooling.

Experiments by Denham ^[51] continued work on ternary systems by looking at surfactants with shorter alkyl chain lengths $C_{12}E_6$ and $C_{14}E_6$ and adding appropriate amounts of oil to simulate the conditions (i.e. alkyl chain volume and head group to water ratio) of a 55% by wt $C_{16}E_6$ /water binary system. Optical microscopy and NMR results revealed that the introduction of the oil helped induce intermediate phases

where in the $C_{12}E_6$ system none had been observed before and in the $C_{14}E_6$ system where the random mesh phase where the random mesh phase was only stable at lower temperatures. The quadrupolar splittings showed that behaviour of these ternary mixtures tended towards $C_{16}E_6$ /water behaviour, although the splitting values were lower than those for the binary sample. This suggests that there is another second order affect that takes place upon adding the oil. This is the first time that an intermediate phase has been found for the $C_{14}E_6$ system, and the binary system shows that the random mesh phase is present over a large temperature range. It has not as yet been elucidated whether the rhombohedral mesh phase exists for the $C_{14}EO_6$ /water binary mixture.

1.5.4 The addition of anaesthetics

Anaesthetics are agents that induce anaesthesia, where the sensations and/or pain are reduced. This includes general anaesthesia where a patient is unconscious, and cannot be woken by pain, and local anaesthesia, where the nerve impulses cannot transmit information. General anaesthetics are administered either by inhalation or intravenously. Inhalation anaesthetics are volatile amphiphilic compounds, whose potency is often linked to their hydrophobicity^[52-56]. Local anaesthetics are injected at their site of action and are therefore not dependent on transport via blood to reach their site of action. It is believed that anaesthetics operate by binding to fast sodium channels in the cell membrane^[57]. However, the exact operation of anaesthetics is still a matter of investigation and how they bind to the sodium channels is not entirely known. They either act directly on the sodium channel, or indirectly, affecting the cell membrane in the region of the channel, causing the channel to close. This latter hypothesis is partly built on the fact that anaesthetic molecules are largely amphiphilic in nature, where there are both a polar moiety and a non-polar moiety. This implies that it may penetrate into the interfacial region of the cell membrane, affecting its structure. Some examples of anaesthetic molecules are given in Figure 1.21.

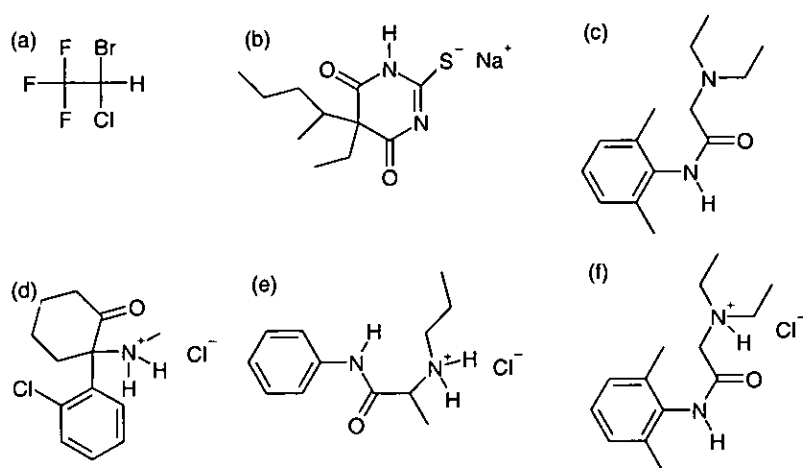


Figure 1.21 Typical Anaesthetic molecules (a) Halothane, (b) Sodium Thiopental, (c) Lidocaine (base form), (d) Ketamine hydrochloride, (e) Prilocaine hydrochloride and (f) Lidocaine hydrochloride.

[52,55,56]

Anaesthetics have been added to surfactant-water mixtures to investigate their affect on phase structures ^[58]. This revealed that anaesthetics, as expected, bind to the interfacial region of the phases, affecting the surface curvature of the phases. Six different anaesthetic agents were added, and the effect of each divided the anaesthetics into two types. Type I anaesthetics decreased the surface curvature of phases, destabilizing phases such as the cubic and mesh phase in favour of the lamellar phase. However type II anaesthetics increased the surface curvature of the mixtures, inducing mesh and cubic phases. At a physiological pH however, both types of anaesthetics decreased the surface curvature of the phases. Figure 1.22 shows these results in the form of a diagram.

It is hypothesised in ^[59] that the mechanism for general anaesthesia is via anaesthetic-induced alteration of the lipid bilayer lateral tension profile which gives rise to the monolayer spontaneous curvature. In the past, only a few anaesthetics have been tested for effects on membrane spontaneous curvature, but the behaviour of alkanols is promising, as they significantly alter the spontaneous curvature of model lipid systems. In this work, experiments were proposed to help test the validity of the proposed hypothesis. The action of anaesthetics is suggested to be prescribed by direct binding to the ion channels, or due to its effect on curvature. The latter option is attractive as the only common feature of most anaesthetics is the fact that they are amphiphilic.

Helfrich^[60] has worked on the mathematics of bending of thin layers, calculating the energy required to bend a layer a given deviation from its spontaneous curvature, expressed as energy per unit area:

$$\partial E = \left(\frac{k_c}{2} \right) \left(\frac{1}{R} - \frac{1}{R_0} \right)^2 \quad (1.6)$$

where R is the actual radius of curvature, R_0 is the natural radius of curvature of the monolayer and k_c is a constant of rigidity for the material. The spontaneous radius of curvature is a measure of the frustrated elastic curvature energy locked into bilayers.

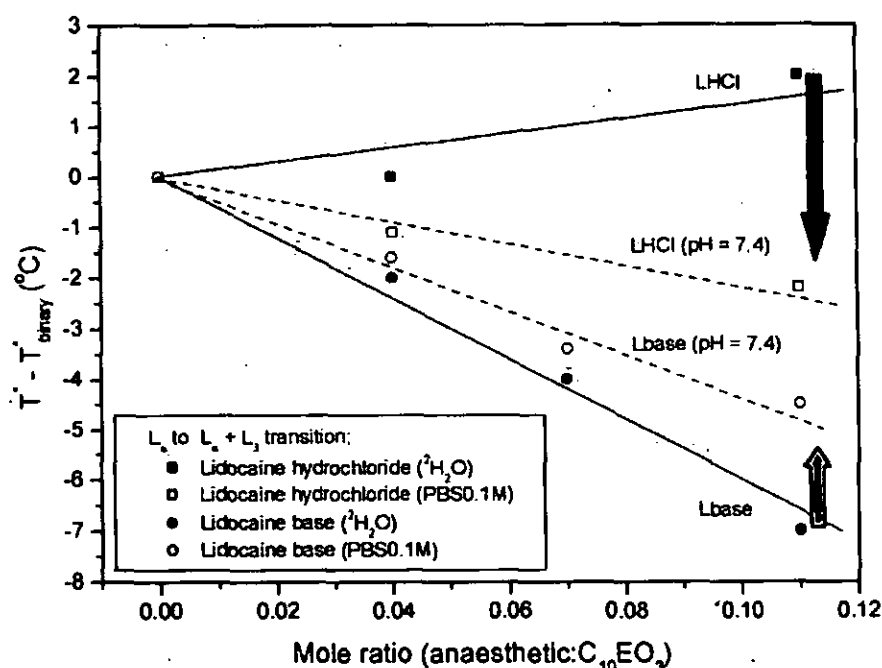


Figure 1.22 Effect of a type I anaesthetic (red) and type II anaesthetic (blue), taken from reference^[61].

It was surmised that anaesthetics may inhibit synaptic transmission by increasing synaptic membrane lateral pressure, therefore inhibiting phospholipid hydrolysis, membrane transduction and synaptic transmission^[62]. In this study, it was hypothesised that anaesthetics modulate the rate of phospholipase C hydrolysis of a lipid monolayer through effects on surface pressure. The experiments conclude that anaesthetics can reversibly inhibit synaptic transmission through their effects on synaptic membrane lateral pressure. This was found using surface pressure experiments performed with a monolayer, using a Wilhemy plate to determine surface pressure.

In [63], local anaesthetic – phospholipid interactions of 2 different anaesthetics and two different phospholipids were investigated by a monolayer technique. A film expansion resulting from the addition of the anaesthetics had the effect of fluidising the monolayer. The different results for the different anaesthetics suggest different possible mechanisms for anaesthesia.

Most local anaesthetics are tertiary amine compounds [64]. They exist in either cationic or uncharged forms, depending on the pH, and the distribution of these forms depends on the pK_a value of the anaesthetic and the pH of the aqueous solution [64]. The uncharged form of the anaesthetic has greater permeability across the membrane compared to the charged form [65,66]. Anaesthetics have a strong amphiphilic character due to their molecular structure, and therefore adsorption should take place at the interface [67-74]. The positively charged form normally interacts electrostatically with any negatively charged sites at or in the membrane, and the distribution of molecules is influenced by the potential created at the membrane surface [64]. Experiments increasing the concentration of local anaesthetics introduced to lipid monolayers showed that there was no change in surface pressure at a higher pH (10.5), but an increase in surface pressure with increasing concentration for lower pH (6.0) [64]. This led to the conclusion that the adsorption of local anaesthetics is better explained by a non electrostatic adsorption than electrostatic site binding model.

Volatile anaesthetics expanded a monolayer by 0.5% by area at constant pressure, and increased the surface pressure by 1 dyn/cm at constant area, after introducing 2.7×10^{13} anaesthetic molecules per square cm [75]. A discontinuity in a surface area-surface pressure plot indicated a phase transition from the liquid expanded to the liquid condensed phase. Anaesthetics decreased the latent heat and entropy change of the phase transition, implying that anaesthetics facilitate the melting of the membrane. The compressional modulus, a measure of the rigidity of the monolayer, was decreased by the anaesthetics. These findings support the theory of anaesthetics that the disordering and expansion of a membrane, with the release of structured water from the interface, is the basis of general anaesthesia.

In [76], the effect of volatile anaesthetics on the surface charge density in adsorbed monolayers was investigated by the electrocapillary method. It was found that the addition of anaesthetics decreased the surface charge density. Eyring et al [77] proposed that the entropy increase is caused by disruption of structure of water molecules in the

solvation shell around the protein. By high precision solution densimetry, volatile anaesthetics released water that was electrostricted at the surface charges of crystalline bovine serum albumin ^[78] and poly(L-lysine) ^[79] in aqueous solutions. It was also found that anaesthetics released part of water molecules bound to DPPC by differential scanning calorimetry. Klemm ^[80] proposed that the interfacial hydration is the cause of anaesthesia.

Studies on the Meyer-Overton rule ^[81-84] show that the potency of anaesthetics is correlated to their solubility in olive oil. However, other studies have shown that this is not the case for all anaesthetics ^[76]. In previous molecular dynamics work, the distribution of anaesthetics in a bilayer was determined ^[81-84]. Anaesthetics were found to increase S_a and decrease d_o , and also decrease the order parameter of the alkyl chain. In ^[76], a nonimmobiliser pair of halothane, C_2F_6 , was introduced to DMPC in a molecular dynamics simulation. It was found that it was distributed evenly along the hydrocarbon chain, with a small preference for the centre of the bilayer. There was a slight modification to the overall structure but no change in potential across the surface. This is compared to the results for the halothane model, where a large perturbation in the potential across the surface was observed.

It is generally accepted that anaesthetics induce anaesthesia by reversible inhibition of synaptic transmission ^[62]. In ^[85], a coarse grained model of a fully hydrated DMPC bilayer was simulated, and halothane was introduced. This showed an increase in S_a and a decrease in d_o .

A molecular dynamics simulation at constant pressure and temperature was performed of a lipid and halothane ^[86]. The results were compared to experimental data and simulations without the anaesthetic. This also showed an increase in S_a and a decrease in d_o . The volume increase of the bilayer was comparable to the volume of the added anaesthetic. There was no significant change in alkyl chain conformation.

1.6 Aim of the Study: Controlling the Phases

Researching the phase structures, and finding out what stabilizes and destabilizes them can help us find out how to control the phases. The phases of surfactant-water mixtures have a great potential for applications such as templating mesoporous structures, which in turn can aid the manufacture of nano-scale devices. However, it is not as simple as it sounds as the conditions under which templating can be performed normally require very specific conditions, and the phase structure needs to be fine

tuned to optimize the process. Therefore by introducing an additional component to the mixture, we are effectively increasing the degrees of freedom for the system, so that it is not just temperature and concentration that affects the phase structure, but the concentration and type of this third component. The addition of an oil or an anaesthetic molecule can provide just that, and as previous research shows, the effect of each of these molecules has a subtle but important effect on the interfacial region and the phase structure. This thesis will study the effect of adding small molecules to surfactant-water mixtures by making use of a mesoscale simulation program, which will be able to uncover more subtle effects of these small molecules.

1.7 References

1. Reinitzer, *Monatsch Chemistry*, **9** 421 (1888)
2. PJ Collins, M Hird, "Introduction to Liquid Crystals"; *Taylor & Francis*: (1997)
3. GW Gray, KJ Harrison, JA Nash, *Electron Letters*, **9** 6 (1973)
4. F Franks, "Water"; *Royal Society of Chemistry*: (1983)
5. GH Heilmeyer, L Zanovi, L Barton, *Proc. IEEE*, **56** 1162 (1961)
6. C Tanford, "The Hydrophobic Effect"; *Wiley Interscience*: (1973)
7. H Wennerstrom, B Lindman, *Physics Report (Review Section of Physics Letters)*, **52** 1 (1979)
8. PJ Collings, "Liquid Crystals - Nature's delicate phase of matter"; *IOP Publishing Ltd*: Princeton (1990)
9. D Evans, H Wennerstrom, "The Colloidal Domain: Where Physics, Chemistry, Biology and Technology Meet"; *VHC Publishers Inc*: New York (1994)
10. JN Israelachvili, DJ Mitchell, BW Ninham. *Journal of the Chemical Society-Faraday Transactions 2* **72** 1525 (1976)
11. PJF Gandy, J Klinowski. *Chemical Physics Letters* **321** (5-6) 363 (2000)
12. PJF Gandy, D Cvijovic, AL Mackay, J Klinowski. *Chemical Physics Letters* **314** (5-6) 543 (1999)
13. CE Fairhurst, MC Holmes, MS Leaver. *Langmuir* **12** (26) 6336 (1996)
14. J Burgoyne, MC Holmes, GJT Tiddy. *Journal of Physical Chemistry* **99** (16) 6054 (1995)
15. PJF Gandy, J Klinowski. *Chemical Physics Letters* **322** (6) 579 (2000)

16. JM Seddon, *Biochimie Biophysics Acta*, **1031** 1 (1990)
17. C Fairhurst, S Fuller, J Gray, MC Holmes, GJT Tiddy, "Handbook of Liquid Crystals"; *Wiley VCH*: Vol. 3 (1998)
18. MC Holmes, MS Leaver, "Phase Transitions in lyotropic liquid crystals". In *Phase Transitions in Complex Fluids*, AM Figueiredo Neto, P Toledano, Eds. *World Scientific*: Singapore (1998)
19. CE Fairhurst, "Intermediate Phases of Surfactant-Water Mixtures". PhD Thesis *University of Central Lancashire*, (1998)
20. MC Holmes. *Current Opinion in Colloid & Interface Science* **3** (5) 485 (1998)
21. MS Leaver, MC Holmes. *Journal de Physique 2* **3** (1) 105 (1993)
22. Y Rancon, J Charvolin. *Journal of Physical Chemistry* **92** (22) 6339 (1988)
23. P Kékicheff, GJT Tiddy. *Journal of Physical Chemistry* **93** (6) 2520 (1989)
24. DJ Mitchell, GJT Tiddy, L Waring, T Bostock, MP McDonald. *Journal of the Chemical Society-Faraday Transactions I* **79** 975 (1983)
25. U Olsson, P Strom, O Soderman, H Wennerstrom, *Journal of Physical Chemistry*, **93** 4572 (1989)
26. JC Lang, RD Morgan, *Journal of Chemical Physics*, **73** 11, 5849 (1980)
27. H Kunieda, K Shinoda, *Journal of Dispersion Science and Technology*, **3** 3, 233 (1989)
28. R Strey, W Jahn, G Porte, P Bassereau, *Langmuir*, **6** 1635 (1990)
29. M Jonstomer, R Strey, *Journal of Physical Chemistry*, **96** 5993 (1992)
30. K Fukuda, U Olsson, U Wurz, *Langmuir*, **10** 9, 3222 (1994)
31. T Hahn, "International Tables of Crystallography"; 4 ed. *Dordrecht: Kluwer Academic*: (1995)
32. CE Fairhurst, MC Holmes, MS Leaver. *Langmuir* **13** (19) 4964 (1997)
33. JS Clunie, JF Goodman, PC Symons, *Transactions Faraday Society*, **65** 287 (1969)
34. V Luzzati, A Tarieu, T Gulik-Krzywicki. *Nature* **217** 1028 (1968)
35. S Puntambekar, MC Holmes, MS Leaver. *Liquid Crystals* **27** (6) 743 (2000)
36. P Kekicheff, B Cabane. *Journal de Physique* **48** (9) 1571 (1987)
37. ES Blackmore, GJT Tiddy. *Journal of the Chemical Society-Faraday Transactions 2* **84** 1115 (1988)

38. U Henriksson, ES Blackmore, GJT Tiddy, O Soderman. *Journal of Physical Chemistry* **96** (9) 3894 (1992)
39. MC Holmes, P Sotta, Y Hendriks, B Deloche. *Journal de Physique II*, **3** (12) 1735 (1993)
40. SS Funari, MC Holmes, GJT Tiddy. *Journal of Physical Chemistry* **96** (26) 11029 (1992)
41. M Leaver, A Fogden, M Holmes, C Fairhurst. *Langmuir* **17** (1) 35 (2001)
42. SS Funari, MC Holmes, GJT Tiddy. *Journal of Physical Chemistry* **98** (11) 3015 (1994)
43. M Laradji, AC Shi, RC Desai, J Noolandi. *Physical Review Letters* **78** (13) 2577 (1997)
44. TQ Chastek, TP Lodge. *Macromolecules* **36** (20) 7672 (2003)
45. IW Hamley, V Castelletto, OO Mykhaylyk, Z Yang, RP May, KS Lyakhova, GJA Sevink, AV Zvelindovsky. *Langmuir* **20** (25) 10785 (2004)
46. K Lyakhova, "Mesoscale modelling of block copolymers under external fields". *University of Leiden*, (2005)
47. P Andre, BW Ninham, MP Pileni. *Advances in Colloid and Interface Science* **89** 155 (2001)
48. B Ninham, *Journal of Physical Chemistry*, **88** 5855 (1984)
49. Y Wang, "The Effects of Small Molecules & Polymer on the Phase Behaviour of C₁₆EO₆-Water Mixture". PhD Thesis *University of Central Lancashire*, (2001)
50. H Kunieda, K Ozawa, K Huang, *Journal of Physical Chemistry B*, **102** 831 (1998)
51. N Denham, "The Stability of the Intermediate Phases in Surfactant Water and Oil Ternary Mixtures". Unpublished Work, (2005)
52. M Hirai, RK Hirai, H Iwase, s Arai, S Mitsuya, T Takeda, H Seto, M Nagao, *Journal of Physics and Chemistry of Solids*, **60** 1359 (1999)
53. A Pohorille, MA Wilson, C Chipot, *Toxicology Letters*, **100-101** 421 (1998)
54. JR Trudel, "Role of membrane fluidity in anaesthetic action". In *Drug and Anaesthetic effects on membrane structure and function*, RC Aloia, Ed. *Wiley-Liss: new York* 14 (1991)
55. I Ueda, "Interfacial effects of anaesthetics on membrane fluidity". In *Drug and Anaesthetic effects on membrane structure and function*, RC Aloia, Ed. *Wiley-Liss: New York* 15 (1991)

56. A Yoshino, K Murate, T Yoshida, H Okabayashi, PR Krishna, H Kamaya, I Ueda, *Journal of Colloid and Interface Science*, **166** 375 (1994)
57. AL Goldin. *Annual Review of Physiology* **63** 871 (2001)
58. M Baciú, MC Holmes, MS Leaver. *Journal of Physical Chemistry B* **111** (4) 909 (2007)
59. SM Gruner, E Shyamsunder, *Annals New York Academy of Sciences*, **625** 685 (1991)
60. W Helfrich, *Z. Naturforschung*, **28** 693 (1973)
61. M Ardeleanu, "A Study of the effect of anaesthetic molecules on model membranes formed in surfactant/water mixtures". PhD Thesis *University of Central Lancashire*, (2004)
62. DM Goodman, EM Nemoto, RW Evans, PM Winter, *Chemistry and Physics of Lipids*, **84** 57 (1996)
63. H Mozaffray, *Thin Solid Films*, **244** 878 (1994)
64. S Ohki, H Ohshima, *Colloids and Surfaces B: Biointerfaces*, **5** 291 (1996)
65. JF Danielli, "The permeability of Natural Membrane"; *Cambridge University Press: Cambridge* (1943)
66. B Hille, *Journal of General Physiology*, **69** 475 (1977)
67. JC Skou, *Acta Pharmacology Toxicology*, **10** 297 (1954)
68. AM Shanes, NL Gershfield, *Journal of General Physiology*, **44** 345 (1960)
69. EK Rooney, AG Lee, *Biochimie Biophysics Acta*, **732** 428 (1983)
70. S McLaughlin, *Prog. Anesthesiol.*, **1** 193 (1975)
71. T Guilmin, E Goormaghtigh, R Braaseuer, J Caspers, JM Ruyschaert, *Biochimie Biophysics Acta*, **685** 169 (1982)
72. S Ohki, *Biochimie Biophysics Acta*, **777** 56 (1984)
73. A Seelig, PR Allegrini, J Seelig, *Biochimie Biophysics Acta*, **939** 267 (1988)
74. D Barthel, O Zschornig, K Lange, R Lenk, K Arnold, *Biochimie Biophysics Acta*, **945** 361 (1988)
75. I Ueda, DD Shieh, H Eyring, *Anesthesiology*, **41** 3, 217 (1974)
76. T Yoshida, H Okabayashi, H Kamaya, I Ueda, *Journal of Pharmaceutical Sciences*, **80** 852 (1991)
77. H Eyring, JW Woodbury, JS D'Arrigo, *Anesthesiology*, **38** 414 (1973)

78. A Shibata, H Kamaya, I Ueda, *Journal of Colloid and Interface Science*, **90** 487 (1982)
79. I Ueda, T Mashimo, *Physiological Chemical Physics*, **14** 157 (1982)
80. WR Klemm, *Alcohol*, **7** 49 (2008)
81. Z Fang, MJ Laster, P Ionescu, DD Koblin, J Sonner, EI Eger Jr, MJ Halsey, *Anesth. ANalg.*, **85** 1149 (1997)
82. L Kandel, BS Chortkoff, J Sonner, MJ Laster, E Eger, *Anesth. ANalg.*, **82** 321 (1996)
83. D Koblin, B Chortkoff, M Laster, E Eger, M Halsey, P Ionescu, *Anesthesiology*, **79** 1043 (1994)
84. S Taheri, M Laster, J Liu, EI Eger 2nd, MJ Hasley, DD Koblin, *Anesth. ANalg.*, **77** 7 (1993)
85. M Pickholz, L Saiz, ML Klein, *Biophysical Journal*, **88** 1524 (2005)
86. K Tu, M Tarek, ML Klein, D Scharf, *Biophysical Journal*, **75** 2123 (1998)

2 Computational Model

2.1 Introduction

In order to investigate the stability of various phases in surfactant-water systems, phase diagrams need to be established. Experimentally researching the phase diagrams of surfactants is both time consuming (because samples take a long time to prepare and analyse) and expensive (because high purities are required). An alternative to this is to employ a computer-based simulation to act as a model for surfactant-water systems. This model would enable a large region of phase space to be investigated quickly to determine general principles. In this chapter, the simulation method of our choice is introduced. The chosen method will then be further discussed and the necessary parameters will be chosen to set up a binary model. The aim of these simulations is to produce a reliable surfactant-water model that accurately produces a typical binary phase sequence. Then the model can be extended by adding further molecules such as oil and anaesthetic molecules.

2.2 Computer Simulations

Computer simulations use mathematical models for simulating the behaviour of complex systems, which cannot be solved analytically. There are many methods and we briefly mention only two of them before introducing the method we use in this work.

2.2.1 Molecular Dynamics

Molecular Dynamics (MD) simulation is a technique for computing the equilibrium and transport properties of a classical many-body system. The particles involved obey the laws of classical mechanics, which is a suitable approximation for many materials. The most important part of a molecular dynamics algorithm is the potential which determines the forces and therefore positions and momentum of the particles. This is also the most time consuming component of the algorithm.

In ^[1], a MD study of the surfactant $C_{12}E_2$ in a water solution was studied. A lamellar phase was produced, and the bilayer spacing and effective surface area per head group was found to be in agreement with x-ray scattering data. Much work has been done looking at micelles and the process of micellization, and ^[2] is one example, using a surfactant consisting of 3 or 4 head sites and 3 or 4 tail sites.

In ^[3] triblock copolymers were simulated in a dynamic mean field density functional theory simulation. Micellar, hexagonal, bicontinuous and lamellar phases were observed which is in good agreement with experiment.

Simulations have also been performed on block copolymers on thin films. The constraint of the film changes the types of phases observed. In ^[4], dynamic density functional theory was used to simulate an asymmetric block copolymer both in the bulk and in a thin film. In addition to the lamellae, mesh and hexagonal phases orientated parallel to the film, a hexagonal phase was found orientated perpendicular to the film. This phase is preferred when neither blocks of the copolymer wet the film surface. A hexagonal phase forming triblock copolymer was simulated in thin films ^[5]. The result was that it arranged itself into terraces of different heights, and each height corresponded to a different phase, including a mesh phase, and both parallel and perpendicular forms of the hexagonal phase.

2.2.2 Monte Carlo

Monte Carlo (MC) is a simulation method that uses probabilities and random movements rather than Newtonian time evolution to obtain an equilibrated simulation result. A simulation box is filled with particles in the same way as a molecular dynamics simulation, with a potential that is normally similar to a standard MD routine. However, instead of a particle potential calculation involving Newton's laws of motion, a completely different integration approach is implemented, as follows. There are many MC approaches but a common type, called Metropolis, will be considered for an example ^[6]. A particle is selected at random, and is moved to a new, test location. The energy of the system for the old and new location is compared, and the new location is accepted if the energy is lower than that of the old position. If the new energy is higher than the old location, the new position is accepted if and only if $e^{-\Delta E/kT}$ is greater than random number between 0 and 1, generated for each prospective movement, where ΔE is the change in energy of the proposed position, k is Boltzmann's constant and T is temperature. This means that the new configuration has a high probability of being accepted if the new energy is only slightly higher, but has a low probability of being accepted if the new energy is a lot higher. This will ensure that eventually an equilibrium will be established where the lowest energy is achieved. Although the route to equilibrium is unphysical (particles are effectively

instantaneously and arbitrarily transported from one position to another), but this has the advantage that the system is unlikely to get trapped in a local minima.

A Monte Carlo simulation of a surfactant-cosurfactant-oil-water system was carried out in ^[7]. The results here showed that for a certain system, there was an optimum chain length of surfactant for maximum emulsion stability.

In ^[8], the transition between the lamellar and bicontinuous phase was investigated using a Monte Carlo simulation for a diblock copolymer, and was compared to an x-ray scattering study. The transition was found to occur via a metastable mesh phase. The ordering of the pores was initially liquid like before developing a hexagonal order. The reverse transition occurs with no metastable mesh phase. The simulations reproduce the results of experiment.

2.2.3 Finite-size effects

The simulation box of any simulation is important. As the number of particles modelled is normally quite small, large scale behaviour is attempted to be induced by introducing periodic boundary conditions so that the box is effectively infinite. However, there are still some problems caused where bulk behaviour cannot be reproduced exactly. Below a critical size, these effects are significant and are known as finite-size effects.

A study was done in 2006 ^[9] investigating the effect of finite size on stress anisotropy. An important but artificial finite-size effect of interfacial area on surface tension is found in simulations on the canonical ensemble.

In a Monte Carlo study in 2002 ^[10], corrections of the pressure due to finite box-size effects were found. These corrections were inversely proportional to the thickness of the simulation box. A modification was proposed which allows the avoidance of these finite-size effects and to estimate the pressure for an infinite system when simulating in a finite box.

2.3 Selection of Simulation Method

The simulations that are required to be performed involve a large amount of molecules due to the supramolecular structures that they create, and also require long equilibration time scales due to nature of the formation of these structures. As the composition of the molecules involved is comparatively simple, it is suitable for this type of study to use coarse graining, as this will enable less simulation particles to model effectively more molecules. Having fewer particles implies that more time

steps can be iterated within a given time. Monte Carlo can be used for a coarse-grained system, although for this study it was considered that a physical regime was more appropriate. Dissipative Particle Dynamics (DPD) is a method that was designed specifically for use for modelling coarse grained hydrodynamic systems, such as surfactant-water systems.

DPD was introduced by Hoogerbrugge and Koelman in ^[11]. The forces due to molecules are given effective friction and fluctuating forces. This approach does not give a correct atomic description of the molecular motion, however it does have the advantage of producing correct hydrodynamic behaviour on large length and time scales. Therefore, DPD has been chosen for the modelling of surfactant-water systems and for the addition of small molecules.

2.4 Simulations Literature Review

The main algorithm of DPD was set up for simulating hydrodynamic phenomena. The physical basis was set up, which was shown both theoretically and in simulations that a quantitative description of isothermal Navier-Stokes flow is obtained with relatively few particles. However, in 1995, an important development in DPD was made ^[12]. The stochastic differential equations corresponding to the updating algorithm of DPD, and the corresponding Fokker-Planck equation were derived. It was shown that just a slight modification to the original algorithm is required before the Gibbs distribution is recovered as the stationary solution to the Fokker-Planck equation. Then, the temperature of the system is directly related to the noise amplitude via the fluctuation-dissipation theorem. However, the correspondingly modified, discrete DPD algorithm is only found to obey these predictions if the time step is sufficiently small. The set up for most DPD simulations has remained largely unchanged since then. On the basis of this model, numerous parameters need to be assigned appropriately before the model can be used. In 1997, Groot and Warren ^[13] critically reviewed DPD and established meaningful parameters, by creating an equation of state for DPD. Choice of an appropriate time step to reduce temperature variations was discussed, and choice of repulsion parameters was considered by comparing the fluid to water and mapping the compressibilities, and also comparing the Flory Huggins parameter to map the repulsive parameter. Additionally, they introduced the Euler integration scheme for the timestep, which allowed a larger timestep to be used with the same temperature rise. In 2000, Otter and Clarke ^[14] critiqued the temperature in DPD, comparing the

Euler integration scheme with the original one proposed by Hooebugge and Koelman.

In 2001, Groot and Rabone^[15] mapped Flory-Huggins parameters for surfactant-water systems, and also did a length scaling considering the volume of the bead they were simulating.

DPD was designed to model hydrodynamic behaviour of fluids, making it suitable for simulating surfactants in aqueous solution, and diblock copolymer melts. The most primitive type of DPD simulation of surfactants in aqueous solution has been using a dimeric model, where the surfactant has been modelled using two beads, connected in a chain. One of the beads represents the hydrophilic head, and the other the hydrophobic tail. In^[16], rigid dimers in a solution of monomers produced a phase diagram similar to the $C_{12}E_6$ experimental phase diagram. Using the same interaction parameters,^[17] studied the evolution of the surface between pure surfactant and solvent. In^[18], another study with a dimeric model achieved the standard lyotropic phases, micellar, hexagonal and lamellar, and in^[19], the same phases were achieved, although a mesh phase and bicontinuous phase were also observed.

Simulations have also been performed on block copolymers. In^[20], diblock and triblock copolymers were simulated using DPD and both types were able to form spherical micelles, cylindrical micelles and lamellar phases. In^[21], triblock copolymers were simulated using DPD and the standard phases were produced, and in addition, the mesh phase was also observed. The same phases were also shown to form using cyclic block copolymers in^[22]. In^[23], a star-diblock copolymer was modelled using DPD and gave the standard phases and also bicontinuous phases as well. In^[24], a triblock copolymer was modelled giving micellar, hexagonal, lamellar and reverse micellar phases. In^[25], a diblock copolymer was modelled giving micellar, hexagonal, gyroid and lamellar phases. In^[26], a diblock copolymer system was simulated using both Monte Carlo and DPD methods. The work focussed on the bicontinuous phase, which was simulated successfully using the DPD method. The basic structure of this phase was similar in the different types of simulation used.

In^[27], The surfactant $C_{12}E_5$ was modelled using 4 beads for the tail part, and 6 beads for the head part; one for each of the polyoxyethylene groups and a further one for the terminal OH group. Water was modelled using one bead. Results showed that the micellar and lamellar phases were obtained using this method. However, each bead represents an identical volume, so the assignment of the beads in the way that was

done was incorrect for the surfactant (see later for comparison of volumes of the hydrocarbon chain and the polyoxyethylene groups.) In ^[28], $C_{12}E_6$ was modelled, using a dimeric model. Although the use of two beads meant the model was fairly primitive, the volumes of tail and head part for $C_{12}E_6$ are similar, so the volumes in this case are comparable to experiment, and are therefore the simulation represents experiment better. It was found that the lamellar, hexagonal and micellar structures are stabilised depending on the strength of the water-head repulsion parameter. The standard phases were also stabilised in ^[29], using amphiphilic models A_1B_1 and A_1B_3 in two different solvents. A study has been done adding a third component to surfactant-water simulations, adding oil (decane) to the surfactant $C_{10}E_4$ ^[30]. The results were shown for a limited range of concentrations, and the components either phase separated, or the bicontinuous phase was observed.

DPD has also been used to investigate model lipid layers. In ^[31], the subtly different bilayer phases of double-tailed surfactants was investigated. A DPD model of a lipid bilayer has been compared to a full atomistic simulation, showing that the coarse grained simulation reproduces all of the basic features of lipids in water solution ^[32]. Groot and Rabone ^[15] also applied the DPD method to biological membranes. The membrane structure obtained matches quantitatively with full atomistic simulations and with experiments reported in the literature. Here, a phospholipid and the surfactant $C_{12}E_6$ were modelled using beads that represented roughly the same volume. On the volume scale they were mapping to, $C_{12}E_6$ consisted of 4 head and 4 tail beads, with one water bead representing 3 water molecules.

The aggregation of polymers and surfactant was studied in detail by Groot ^[33]. Fluorinated surfactants have also been modelled in DPD ^[34]. The fluorinated surfactant induces the lamellar phase at a lower concentration than the hydrogenated surfactant.

In most systems, the bilayer phase occurs when the tails of the surfactants do not interdigitate, however, in some instances, this interdigitation occurs. One DPD study ^[35] changed the temperature of the system and the head to head interaction parameter, and showed that in the low temperature range for high head to head interaction parameter, the interdigitated phase is favoured. Another study ^[36] considered under what conditions the interdigitated phase was induced. This also showed that interdigitation was favoured when the head to head interaction parameter was increased, and when the head group had an additional bead added.

2.5 Dissipative Particle Dynamics

DPD is a relatively new method of mesoscale simulation. Standard Molecular Dynamics is too computationally costly for complex fluids, as the number of particles and the number of time steps involved would be too large. DPD is coarse grained and therefore more computationally efficient. The regime is like Brownian motion for fluids, but differs in that momentum is conserved in DPD. Energy however, is not conserved in DPD.

The DPD model is proposed with N particles moving in a continuum domain of volume V . These particles or ‘beads’ represent a cluster or group of atoms or molecules. In a DPD simulation, one bead represents a specific volume. The system is completely defined by the positions r_i and momenta p_i for particles $i = 1, 2, \dots, N$. The system is updated in discrete time steps Δt . The time evolution of the particles is governed by Newton’s equations of motion:

$$\frac{dr_i}{dt} = v_i, \quad \frac{dv_i}{dt} m_i = f_i. \quad (2.1)$$

A demonstration of the DPD regime with a justification of its form follows.

The total force on a given particle i is:

$$F_i^T = \sum_{j \neq i} F_{ij}^C + F_{ij}^D + F_{ij}^R \quad (2.2)$$

where F_{ij}^C is a conservative force, F_{ij}^D is a dissipative force and F_{ij}^R is a random force. Pair additivity has been assumed. The conservative force is the force that will drive the separation between unlike components, and account for the hydrophobic effect in surfactant-water simulations. This force will be considered after the other two forces, which need to be considered in tandem.

Galilean Invariance requires that the dissipative and random forces depend only on combinations of $r_{ij}=r_i-r_j$ and $v_{ij}=v_i-v_j$. The requirement of Isotropy demands that the forces should transform under rotations as vectors. It is also required that the dissipative force is linear on the momentum and the random force is independent of the momentum. A simple form of these forces that satisfy these hypotheses is:

$$F_{ij}^D = -\gamma\omega_D(r_{ij})(e_{ij}v_{ij})e_{ij} \quad (2.3)$$

$$F_{ij}^R = \sigma\omega_R(r_{ij})e_{ij}\zeta_{ij} \quad (2.4)$$

Where $r_{ij} = |r_i-r_j|$, $e_{ij}=(r_i-r_j)/r_{ij}$, and ζ_{ij} is a Gaussian white noise term with $\zeta_{ij} = \zeta_{ji}$ and $\langle \zeta_{ij}(t) \rangle = 0$. The brackets indicate that the value is of the time averaged value of $\zeta_{ij}(t)$.

ω_D and ω_R are weight functions that ensure that F^R and F^D vanish when r_{ij} becomes greater than r_c , a cut off distance for the forces. The sum is over all particles within a cutoff radius r_c . The cutoff radius is implemented to reduce the computational time in summing negligible interactions, and mimics the nature of real intermolecular interactions, which in general only have noticeable effects within nearest neighbours. γ and σ are the friction coefficient and the amplitude of noise respectively, representing the amplitude of the forces.

By substituting F^R and F^D into Newton's Second Law, a set of Langevin equations is obtained, which are written in the mathematically well-defined form of stochastic differential equations:

$$\begin{cases} dr_i = \frac{p_i}{m_i} dt \\ dp_i = \left[\sum_{j \neq i} F_{ij}^C(r_{ij}) + \sum_{j \neq i} -\gamma \omega_D(r_{ij}) (e_{ij} \cdot v_{ij}) e_{ij} \right] dt + \sum_{j \neq i} \sigma \omega_R(r_{ij}) e_{ij} \zeta_{ij} dt \end{cases} \quad (2.5)$$

where m_i is the mass of the particle. The Fokker-Planck equation that corresponds to this set of differential equations can be derived. This is detailed in ^[12], following standard methods from ^[37]. By considering the resulting Fokker-Planck equation and the conditions under which the steady state solution is the Gibbs canonical ensemble, the following two relations are found:

$$\omega_R(r) = \omega_D^{1/2}(r) \quad (2.6)$$

$$\sigma = (2\gamma k_B T)^{1/2} \quad (2.7)$$

where σ is a noise term, k_B is Boltzmann's constant and T is the temperature of the system. This is the fluctuation dissipation theorem for the DPD method.

From the above relation, and using a simple form for the weight function $\omega_R = (1-r_{ij})$, F^D and F^R can now be defined as:

$$F_{ij}^D = \begin{cases} -\gamma(1-r_{ij})^2 (\hat{r}_{ij} \cdot v_{ij}) \hat{r}_{ij} & (r_{ij} < r_c) \\ 0 & (r_{ij} \geq r_c) \end{cases} \quad (2.8)$$

$$F_{ij}^R = \begin{cases} \sigma(1-r_{ij}) \zeta_{ij} \hat{r}_{ij} & (r_{ij} < r_c) \\ 0 & (r_{ij} \geq r_c) \end{cases} \quad (2.9)$$

Another function needs to be set up for F^C , the conservative force. This will involve a repulsion parameter, a . This parameter will perform two functions in the simulation. It will provide the natural repulsion between all beads to account for the compressibility

of the system. A value for a that will ensure that the system behaves as a realistic fluid will be considered shortly. Also, this repulsion parameter will also provide the repulsion between unlike particles. The value for this part of the repulsion parameter will also be considered later. There will also be a weight function on this force as for the dissipative and random forces to ensure they only act within the cutoff distance r_c . There are no specific requirements for the form of the weight function as for F^D and F^R , and the simple form $(1-r_{ij})$ will be used. The conservative force is therefore a soft repulsion given by:

$$F_{ij}^C = \begin{cases} a_{ij}(1-r_{ij})\hat{r}_{ij} & (r_{ij} < r_c) \\ 0 & (r_{ij} \geq r_c) \end{cases} \quad (2.10)$$

where a_{ij} is the interaction parameter between particle i and j , and r_{ij} is the separation between particle i and j . a is a unitless parameter which gives a strength for the repulsion between particle i and j . This parameter is a measure of the compressibility of the fluid, and later this parameter will be mapped onto the compressibility of water to find suitable values of a for like components. Also, to mimic the hydrophobic effect between two moieties, a will be larger, giving a stronger repulsion.

2.6 DPD Parameters

2.6.1 Time evolution & Temperature Stability

To advance the set of positions and velocities, a modified version of the velocity-Verlet algorithm is used^[38]. This was introduced by Groot and Warren^[13], to increase the efficiency of the DPD algorithm by enabling greater temperature stability for larger time steps, increasing the efficiency of the algorithm.

Δt is the time step and λ is a constant associated with the time integration, a factor that is said to account for some of the additional effects of the stochastic interactions. The unit of time, τ , is set to $r_c(m/k_B T)^{1/2}$.

The time step Δt should be chosen as large as possible without compromising the accuracy of the model. This is because the larger the time step, the more movement of the particles occur in one time step, allowing for a quicker simulation. However, if the timestep is too large, then the temperature of the system will not remain constant. This is because the temperature is only set at the initialisation stage of the simulation. This is done by ensuring that when the particles are randomly introduced into the box, they are given a random position, and a random velocity so that the average velocity of the

particles will ensure that the temperature T of the system overall is the desired T , given by $k_B T = \langle v^2 \rangle / 3$. The fluctuation-dissipation relation will ensure that the temperature will remain at approximately this value within a certain error without the need for any direct temperature control. However, if the timestep is too large, then the error margin for temperature deviation becomes significant, so there is a limit to the timestep value. Using $\lambda = 0.65$ the time step for a simulation at $1 k_B T$ can be up to 0.06 with only a temperature rise of 1% [15]. Therefore, to optimise the model, the time step Δt will be chosen as 0.06 and λ will be 0.65.

The noise term σ also affects the temperature stability and temperature relaxation time [ref]. When the noise amplitude σ is reduced, the speed at which the system reacts on temperature variations is reduced. When it is increased, a slow increase in $k_B T$ is found up to $\sigma=8$, beyond which the temperature grows rapidly and the simulation itself may become unstable. As a compromise, $\sigma=3.67$ was chosen to ensure relatively fast temperature responses whilst reducing the inherent temperature increases. With $k_B T=1$, this meant that $\gamma=6.75$.

2.6.2 Units

The DPD model is based on three fundamental dimensionless parameters, length, energy and mass. As these are dimensionless, they can be assigned for convenience, but they can be scaled to the real world for comparison. The unit of length, r , can be based on the cut off distance r_c , so $r_c=1$. The volumes of the beads are the same by definition, and the masses of the beads are therefore going to be similar. For simplicity the mass of all of the beads is 1, and the unit of energy, $k_B T = 1$. DPD units of length, energy and time are denoted by σ , ϵ and τ , respectively.

2.6.3 The Repulsion Parameter

As the DPD technique is based on soft sphere interactions the repulsion parameter a needs to be chosen while taking into account the compressibility of the system. An effective way of doing this is to map the compressibility of water onto the simulation beads. The definition of compressibility β is:

$$\beta = -\frac{1}{V} \frac{\partial V}{\partial p} \quad (2.11)$$

Where p is the pressure of the system and V is the Volume.

To make the comparison between experiment and simulation, a number density ρ will be introduced representing the number of molecules in a volume V :

$$\rho = V \frac{\partial \rho}{\partial V} \quad (2.12)$$

Substituting equation 2.12 into equation 2.11 and using the chain rule gives:

$$\beta = -\frac{1}{\rho} \frac{\partial \rho}{\partial p} \quad (2.13)$$

Rearranging and dividing by $k_B T$ on each side gives a relation between experimental values and simulation values:

$$\frac{1}{\beta \rho k_B T} = \frac{1}{k_B T} \frac{\partial p}{\partial \rho} \quad (2.14)$$

Where the left hand side values represent the experimental values and the right hand side values represent the simulation values. To find $\partial p / \partial \rho$, Groot and Warren [ref] simulated water using DPD beads and measured how the pressure of the system varied as a function of the bead density. They found that above a certain density, the following relation was found, and this is sometimes known as the equation of state for DPD, which is quadratic in density:

$$p = \rho k_B T + \alpha \rho^2 \quad (\alpha = 0.101 \pm 0.001) \quad (\rho > 2) \quad (2.15)$$

Differentiating equation 2.15 with respect to ρ gives:

$$\frac{\partial p}{\partial \rho} = k_B T + 2\alpha \rho \quad (2.16)$$

Substituting this into equation 2.14, with the compressibility of water being $4.5 \times 10^{-10} \text{ m}^2/\text{N}$ [39] and the number density of water molecules is $3.35 \times 10^{28} \text{ m}^{-3}$, reduces the equation to:

$$\alpha = 75 k_B T / \rho \quad (2.17)$$

For our model, we have already set $k_B T = 1$. ρ should be high enough so that equation 2.12 holds, but should also be as low as possible to minimise the computational time. Therefore the lowest density that the relation holds well for is $\rho = 3$. This means that for a simulation of bead density 3, the repulsion parameter for like beads should be chosen as 25 to model water. The interaction parameter that was chosen above models the compressibility of water.

2.6.4 Hydrophobic Repulsion

To model the hydrophobic effect, an excess repulsion is added for the interactions between water and tail beads, and head and tail beads. This excess or hydrophobic repulsion parameter will be denoted by Δa . Since the simulation system is quite incompressible, as we have modelled water, this model should be quite close to the Flory-Huggins lattice model. The Flory-Huggins lattice model is a mathematical function describing the thermodynamics of polymer solutions and takes into account the dissimilarity in molecular sizes in adapting the usual expression of entropy of mixing. Groot and Warren ^[13] mapped the Flory-Huggins model onto Δa using the free energy per lattice site F :

$$\frac{F}{k_B T} = \frac{\phi_A}{N_A} \ln \phi_A + \frac{\phi_B}{N_B} \ln \phi_B + \chi \phi_A \phi_B \quad (2.18)$$

Where ϕ_A and ϕ_B are volume fractions of the A and B components and N_A and N_B are the number of segments per A and B molecule, and χ is the dimensionless Flory Huggins parameter. χ is positive for two components that do not favour contact with each other, and negative for components that do favour contact with each other. If χ is positive and sufficiently large, the free energy develops two minima separated by a maximum.

The free energy density that corresponds to the pressure of a *single* component is:

$$\frac{f_v}{k_B T} = \rho \ln \rho - \rho + \frac{\alpha \rho^2}{k_B T} \quad (2.19)$$

For a *two* component system of chains:

$$\frac{f_v}{k_B T} = \frac{\rho_A}{N_A} \ln \rho_A + \frac{\rho_B}{N_B} \ln \rho_B - \frac{\rho_A}{N_A} - \frac{\rho_B}{N_B} + \frac{\alpha(a_{AA}\rho_A^2 + a_{AB}\rho_A\rho_B + a_{BB}\rho_B^2)}{k_B T} \quad (2.20)$$

Choosing $a_{AA}=a_{BB}=a$, assuming $\rho_A+\rho_B=\rho=constant$, setting $x=\rho_A/\rho$ and $a_{AB}=a+\Delta a$, equation 2.20 can be simplified to:

$$\frac{f_v}{\rho k_B T} \approx \frac{x}{N_A} \ln x + \frac{(1-x)}{N_B} \ln(1-x) - \frac{x}{N_A} - \frac{(1-x)}{N_B} + \frac{2\alpha\Delta a\rho}{k_B T} x(1-x) \quad (2.21)$$

By comparing equations 2.20 and 2.21 a correspondence between soft spheres and Flory-Huggins by $f_v/\rho = F$, where:

$$\chi = \frac{2\alpha\Delta a\rho}{k_B T} \quad (2.22)$$

To test this correspondence, Groot and Warren [ref] simulated different models with different Δa values. It was found that χ is in fact linear in Δa , but not in density. For $\rho = 3$, the following relation was found:

$$\chi = (0.286 \pm 0.002)\Delta a \quad (2.23)$$

Groot and Rabone^[15] used a water-hydrocarbon Flory Huggins parameter as 6, found where three water molecules are represented by one bead, and this is largely independent of temperature. Using this value gives $\Delta a = 21$. This will be used as a rough guide for preliminary simulations, but different Δa values will be investigated to find the optimum value.

2.7 Model

2.7.1 Length Scale

As DPD is a coarse-grained approach, one particle or “bead” in the model represents a cluster of atoms. Each DPD bead represents a volume, and it is this volume that determines the length scale of the simulation. A bead volume needs to be chosen so that each bead is capable of representing water, hydrocarbons and oxyethylene. Table 2.1 shows the density and volume for H_2O , $\text{CH}_3(\text{CH}_2)_{11}$ and $(\text{OCH}_2\text{CH}_2)_6\text{OH}$.

	Density (kgm^{-3})	Volume (nm^3)
H_2O	1000	0.030
$\text{CH}_3(\text{CH}_2)_{11}$	750 ^[40]	0.380
$(\text{OCH}_2\text{CH}_2)_6\text{OH}$	1123 ^[41]	0.420

Table 2.1 Densities and volumes for water, hydrocarbon and oxyethylene groups.

By choosing the DPD bead volume as 0.09nm^3 , each DPD bead represents the volume of three water molecules, the volume of a $(\text{CH}_2)_3$ group and the volume of 1.5 $\text{CH}_2\text{CH}_2\text{O}$ groups. The non-ionic surfactant C_{12}E_6 can therefore be conveniently modelled using 4 tail beads and 4 head beads connected in a single chain with harmonic bonds.

The simulated bead number density ρ was chosen as 3 as it is the lowest value (and hence computationally quickest) for which the DPD equation of state holds (see earlier). A diagram showing the excess pressure as a function of simulated density is shown in Figure 2.1. This is related to the volume of each bead by:

$$\rho = \frac{1}{V_B} \quad (2.24)$$

To relate this to a physical size, ρ can be redefined as the number of beads in a cube of size r_c . Therefore, the physical size of the interaction radius is given by:

$$r_c^3 = V_B \rho \quad (2.25)$$

Using $V_B = 0.09\text{nm}^3$ and $\rho = 3$, $r_c = 0.65\text{nm}$.

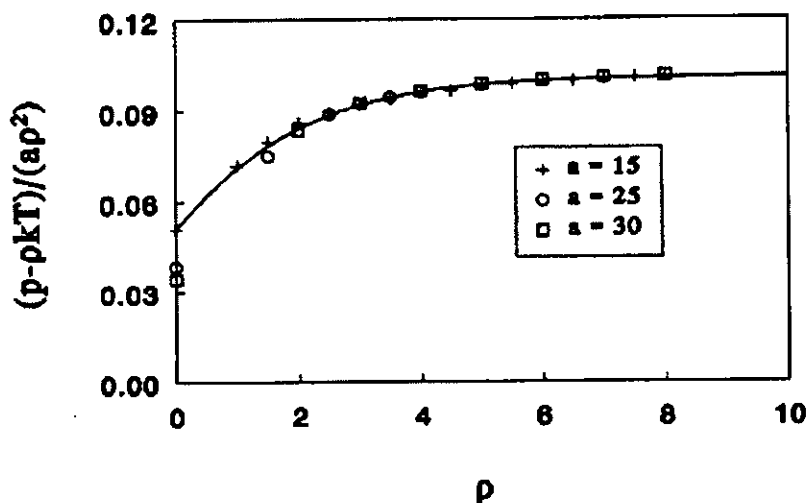


Figure 2.1 Excess pressure as a function of simulated density. The DPD equation of state holds above $\rho \approx 3$, where the graph becomes linear. Taken from ^[13].

2.7.2 Bonds

The beads in the surfactant are connected with bonds modelled using harmonic springs using a potential of type:

$$U_{bond}(r) = \frac{1}{2}k(r - r_o)^2 \quad (2.26)$$

Where r_o is the equilibrium bond length and k is the spring constant. The all trans length, where all of the carbon-carbon bonds are in their most stretched out form, of $C_{12}E_6$ is 3.57nm . Dividing this value by the number of beads representing a $C_{12}E_6$ molecule (8) gives 0.46nm . This is approximately $1r_c$ (0.64633nm).

Finally, the strength of the harmonic bonds should mimic the bond strength for carbon carbon bonds. For an accurate conversion, the vibrational frequencies of carbon carbon bonds can be used to calculate the spring constant for the harmonic bond equation. However, this would exceed the maximum force limit used to prevent any large forces disrupting the simulation, and a strength needs to be chosen that is just strong enough to constrain the bonds to 1% of their equilibrium length. To determine

this strength a series of test simulations were performed, the results of which are shown in the next chapter.

2.8 Simulation Hardware & Software

A coarse grained molecular dynamics program COGNAC v5 was used to perform all of the simulations, and is part of OCTA 2006^[42]. See Appendix A for information on how OCTA and COGNAC were used to simulate and analyse the models. Input and output files were created and modified with Gourmet, the graphical user interface for OCTA. All simulations were performed using an SGI Altix 3700 server at the University of Central Lancashire's High Performance Computing Facility.

Water beads and surfactant chains will be introduced arbitrarily into a simulation box with periodic boundary conditions. The physical size of the simulation box is determined by the number of beads.

2.9 References

1. S Bandyopadhyay, M Tarek, ML Lynch, ML Klein, *Langmuir*, **16** 942 (2000)
2. MA Floriano, E Caponetti, *Langmuir*, **15** 3143 (1999)
3. BAC van Vlimmeren, NM Maurits, AV Zvelindovsky, GJA Sevink, JGEM Fraaije, *Macromolecules*, **32** 646 (1999)
4. HP Huinink, JCM Brokken-Zijp, MA van Dijk, GJA Sevink. *Journal of Chemical Physics* **112** (5) 2452 (2000)
5. A Knoll, A Horvat, KS Lyakhova, G Krausch, GJA Sevink, AV Zvelindovsky, R Magerle. *Physical Review Letters* **89** (3) (2002)
6. MP Allen, DJ Tildesley, "Computer Simulation of Liquids"; Clarendon Press: Oxford (1993)
7. HH Pan, HR Li, DX Liu, SJ Han, *Molecular Simulation*, **29** 12, 797 (2003)
8. IW Hamley, V Castelletto, OO Mykhaylyk, Z Yang, RP May, KS Lyakhova, GJA Sevink, AV Zvelindovsky. *Langmuir* **20** (25) 10785 (2004)
9. ME Velazquez, A Gama-Goicochea, M Gonzalez-Melchor, M Neria, J Alexandre. *Journal of Chemical Physics* **124** (8) (2006)
10. MR Stukan, VA Ivanov, M Müller, K Binder, *Journal of Chemical Physics*, **117** 21, 9934 (2002)
11. PJ Hoogerbrugge, JMVA Koelman, *International Reviews in Physical Chemistry*, **19** 3, 155 (1992)

12. P Español, P Warren, *Europhysics Letters*, **30** 4, 191 (1995)
13. RD Groot, PB Warren, *Journal of Chemical Physics*, **107** 11, 4423 (1997)
14. WK Den Otter, JHR Clarke, *International Journal of Modern Physics C*, **6** 1179 (2000)
15. RD Groot, KL Rabone. *Biophysical Journal* **81** (2) 725 (2001)
16. S Jury, P Bladon, M Cates, S Krishna, M Hagen, N Ruddock, P Warren. *Physical Chemistry Chemical Physics* **1** (9) 2051 (1999)
17. P Prinsen, PB Warren, MAJ Michels. *Physical Review Letters* **89** (14) (2002)
18. E Ryjkina, H Kuhn, H Rehage, F Möller, J Peggau, *Angewandte Chemie-International Edition*, **41** 6, 983 (2002)
19. SL Yuan, ZT Cai, GY Xu. *Acta Chimica Sinica* **60** (2) 241 (2002)
20. XR Cao, GY Xu, YM Li, ZQ Zhang. *Journal of Physical Chemistry A* **109** (45) 10418 (2005)
21. B Abu-Sharkh, A AlSunaidi. *Macromolecular Theory and Simulations* **15** (6) 507 (2006)
22. HJ Qian, ZY Lu, LJ Chen, ZS Li, CC Sun. *Macromolecules* **38** (4) 1395 (2005)
23. Y Xu, J Feng, H Liu, Y Hu. *Molecular Simulation* **32** (5) 375 (2006)
24. SG Schulz, U Frieske, H Kuhn, G Schmid, F Muller, C Mund, J Venzmer. *Tenside Surfactants Detergents* **42** (3) 180 (2005)
25. RD Groot, TJ Madden. *Journal of Chemical Physics* **108** (20) 8713 (1998)
26. FJ Martinez-Veracochea, FA Excobedo, *Journal of Computational Chemistry*, **125** 104907 (2006)
27. SG Schulz, U Frieske, H Kuhn, G Schmid, F Muller, C Mund, J Venzmer. *Tenside Surfactants Detergents* **41** (5) 230 (2004)
28. H Nakamura, Y Tamura, *Computer Physics Communications*, **169** 1-3, 139 (2005)
29. C Huang, YJ Chiou, YK Lan, *Polymer*, **48** 877 (2007)
30. SG Schulz, H Kuhn, G Schmid, C Mund, J Venzmer. *Colloid and Polymer Science* **283** (3) 284 (2004)
31. M Kranenburg, B Smit. *Journal of Physical Chemistry B* **109** (14) 6553 (2005)
32. AP Lyubartsev. *European Biophysics Journal with Biophysics Letters* **35** (1) 53 (2005)

33. RD Groot, *Langmuir*, **16** 7493 (2000)
34. HY Sun, GY Xu, YM Li, YJ Chen. *Journal of Fluorine Chemistry* **127** (2) 187 (2006)
35. M Kranenburg, M Venturoli, B Smitt, *Physical Review e*, **67** 060901 (2003)
36. M Kranenburg, M Venturoli, B Smit, *Journal of Physical Chemistry B*, **107** 11491 (2003)
37. CW Gardiner, "Handbook of Stochastic Methods"; *Springer-Verlag*: Berlin (1983)
38. MP Allen, DJ Tildesley, "Computer Simulation of Liquids"; *Clarendon*: Oxford (1987)
39. "Handbook of Chemistry and Physics"; 47 ed. *Chemical Rubber Company*: (1966)
40. TS Khasanshin, AP Shchamialiou, OG Poddubskij. *International Journal of Thermophysics* **24** (5) 1277 (2003)
41. "Research Chemicals, Metals and Materials", *Alfa Aesar* (2008)
42. OCTA. www.octa.jp. Last Accessed 12/9/2008.

3 DPD Binary System – Parameter Setting

3.1 Introduction

It is now necessary to elucidate some further parameters of the model, and in doing so, highlight some of the restrictions and limitations of the model. In the previous chapter, parameters were obtained by comparison with theory and experiment. In this chapter, parameters were chosen by performing simulations to elucidate the most appropriate values. The optimum bond strength was found by performing a series of simulations at different bond strengths. The optimum hydrophobic interaction parameter was found by investigating a range of values and selecting one which gives a phase sequence closest to what is found experimentally. This gave the basic model for a binary surfactant-water system. The effect of box size was also investigated to determine if there were any finite-box size effects.

3.2 Experimental Results

The aim of the binary simulations of $C_{12}E_6$ is to develop a model that produces results as close as possible to experiment. A $C_{12}E_6$ water system has been investigated by Clunie et al ^[1]. A phase diagram was produced, and is shown in Figure 3.1. This phase diagram shows that the most dominant phases are L_1 , H_1 and L_α , with a small region of V_1 lying in between the H_1 and L_α phases. At room temperature, the phase sequence upon increasing concentration is:

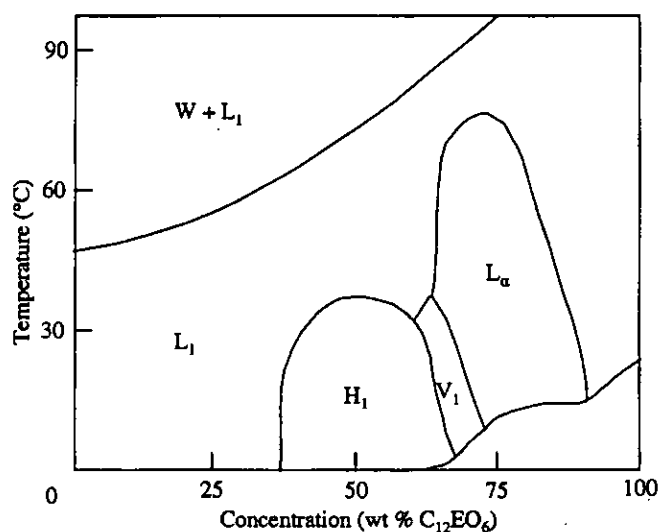
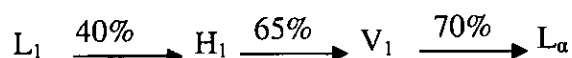


Figure 3.1 Phase diagram for $C_{12}E_6$, taken from reference ^[1].

3.3 Bond Strength k

A set of simulations were performed to determine the optimum bond strength k for the harmonic bonds of the surfactants. This value could be mapped from the vibrational frequencies of carbon-carbon bonds from infra-red spectroscopy, and using the following equation that relates frequency of vibration with the spring constant:

$$f = \frac{1}{2\pi} \sqrt{\frac{k}{m}}$$

where f is the frequency of oscillation, k is the spring constant and m is the mass of the two atoms that are connected by the bond. The vibrational frequencies for carbon-carbon bonds are $5 \times 10^5 \text{ Hz}$ and $2 \times 10^5 \text{ Hz}$ for the symmetric and asymmetric bond frequencies respectively [2]. However, for a coarse grained model, each DPD bond would consist of several bonds coupled together, so this coupling would need to be taken into account if the bond strength was mapped directly from the vibrational frequencies. As this coupling is a non-trivial problem, the choice of bond strength can be instead chosen from a phenomenological perspective.

It was decided that an appropriate way to determine a suitable spring constant is to find the lowest value of k that yields a value equilibrium bond length of $1 r_c$ (0.646nm, see section 2.7.1) with a low standard deviation, in this case chosen to be 1%.

A simulation of 3051 C_{12}E_6 molecules consisting of 4 tail beads and 4 head beads connected in a single chain were arbitrarily introduced into a simulation cube of side 14.5nm. All of the parameters were as chosen in chapter 2, where $\Delta a = 15$. Three different k values were chosen, 10, 100 and $200 \epsilon \sigma^{-2}$. The mean and standard deviation bond lengths were measured from 50 bonds, and the results are shown in Figure 3.2.

It can be seen that at $k = 100 \epsilon \sigma^{-2}$, the equilibrium bond length is within 1% of $1 r_c$. The standard deviation also decreases significantly from $k = 10 \epsilon \sigma^{-2}$ to $k = 100 \epsilon \sigma^{-2}$. The mean and error in bond lengths do not change significantly for spring constant values higher than $100 \epsilon \sigma^{-2}$, so $k = 100 \epsilon \sigma^{-2}$ will be chosen.

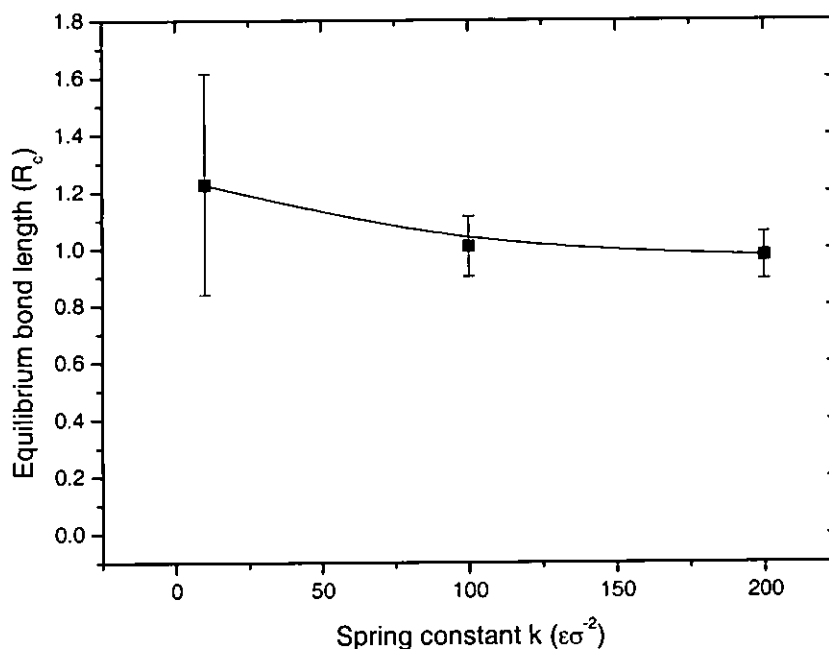


Figure 3.2 Average bond length as a function of bond spring constant. Errors show the standard deviation of the bond length. Line is a guide to the eye.

3.4 Phase Sequence & Phase Definitions

A series of simulations has been performed at different concentrations to determine a preliminary phase sequence. Based on reference ^[3], a theoretical excess repulsion parameter of $\Delta a = 21$ was chosen as a first approximation. This can be varied to optimise the model, but should give a good guide to the phases present. The numbers of waters and surfactants for each concentration were calculated using the molecular weight of $C_{12}E_6$ and water molecules so that each concentration can be represented by an equivalent percentage by weight $C_{12}E_6$. A simulation box of side 14.5nm was chosen, as this should include six lamellar repeat distances from corner to corner at a surfactant concentration of 100%, giving a reasonably large simulation cell. The size of the simulation box will be considered in more detail in section 3.6. Simulations were first performed for 100,000 time steps, but further time steps were undertaken if necessary until equilibrium is established.

To ascertain whether a simulation has reached equilibrium, the total energy as a function of time needs to be considered. The energy of the simulation decreases as the system gradually becomes more ordered, until equilibrium is established, where the phase structure is stable.

A typical Energy versus time plot is shown in Figure 3.3, showing a simulation for 90% surfactant and water system at a box size of 14.5nm, for 100000 time steps. This plot shows the batch average energy of 5000 time steps at 5000 time step intervals. Batch average energy is used to reduce the random variation in energy at instantaneous points. After the gradient of the plot becomes sufficiently close to zero, it can be said that the simulation has reached equilibrium. The simulation in Figure 3.3 becomes lamellar between 65 and 70 thousand time steps, so therefore, the simulation has reached equilibrium after this point, where the gradient of the plot is close to zero. The equilibration of the phases will be considered in this way, in order to ensure that they are fully equilibrated.

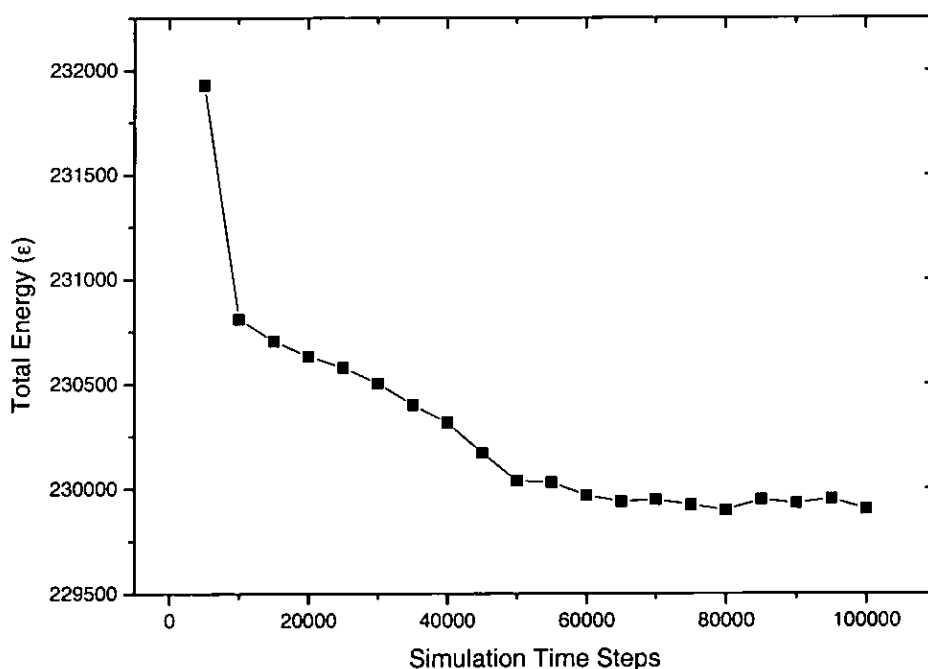


Figure 3.3 A Total energy v time plot for a typical simulation. Line is a guide to the eye.

After the simulations were performed, the phase structures were identified by observing a visualisation of the model using the graphical user interface of the OCTA program. There are two main types of visualisation available. One is a ball-stick model that represents each bead by a ball, with different types of beads (tail, head, water etc) as a different colour. Lines or “sticks” between these dots represent bonds. This gives the most information about the location of the molecules, but as the model contains thousands of molecules this visualisation is not clear, especially for three-dimensional structures. However, a two-dimensional structure, when viewed

perpendicular to the plane, will appear reasonably clear. The other type of visualisation shows an iso-density surface where the local bead density of tail and head beads is 0.5, i.e., at the interfacial region. Although this gives no detail of the molecules, it conveniently shows the phase structure for even complex phases, and this visualisation method was used to identify phase structures.

The results of these simulations from 50-95% by weight concentrations of surfactant in 5% graduations are shown as iso-density surfaces (showing the interface region) in Figure 3.4. Detailed structures of the two-dimensional phases, the hexagonal and lamellar phases, can be seen in Figure 3.5, showing a ball-stick model of the surfactants with the water beads. From these figures, it can be seen that the water beads pack within the head region, as expected.

At 50 and 55%, there is aggregation of the surfactants into elongated micelles, and the phase is therefore defined to be a cylindrical type phase. However, as the cylinders have no particular orientation with respect to each other or show any inter-aggregate order, this phase will be referred to as a disordered hexagonal phase (dH_1). Increasing the concentration to 60%, the cylinders elongate completely forming infinite cylinders. These cylinders are arranged in a hexagonal fashion, so this is the hexagonal phase (H_1). On increasing the concentration to 65%, the structure changes into interconnected cylinders arranged in an irregular fashion. The interconnections are largely threefold, in the same way that most bicontinuous structures are, so this phase is defined to be a bicontinuous phase. Three-connected structures have the lowest interfacial curvature that allows three dimensional structures to form. This does not show any distinct order, unlike bicontinuous phases in literature, so this phase will be referred to as a disordered bicontinuous phase (dV_1). At 80% some layer-like patterns appear. However, this phase is also disordered, with pores and interconnections between the layers. The sponge-like phase studied experimentally [4] is loosely based on a lamellar phase with interconnections between the layers so this phase is defined to be a sponge phase (L_3). At 85%, there are layers that have water filled defects or pores, so this phase is the mesh phase (Mh_1). From 90-100%, the phase is lamellar (L_α).

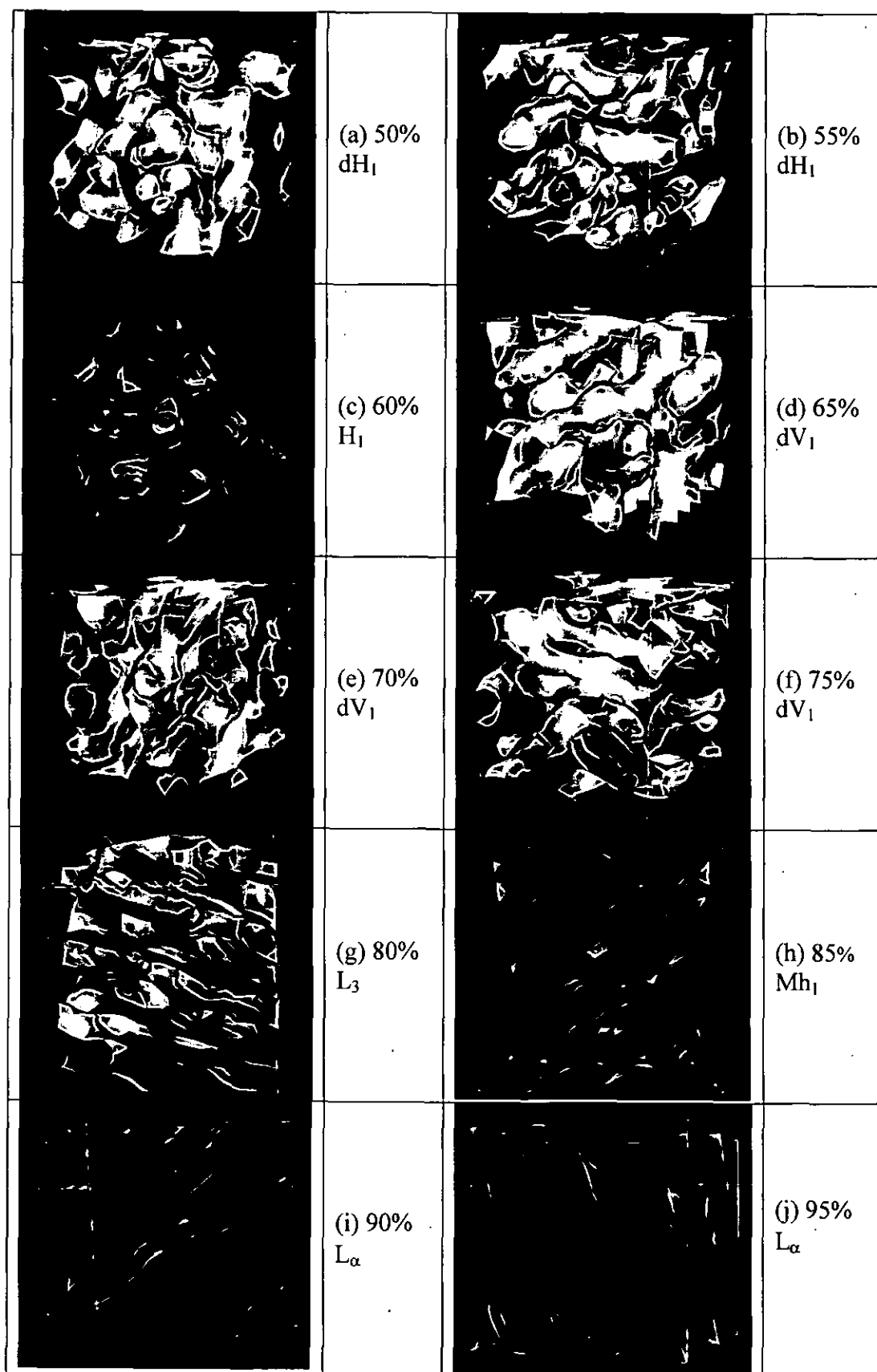


Figure 3.4 Isodensity surface images of $C_{12}E_6$ -water simulations after 100,000 time steps showing the interface between the head and the tail region.

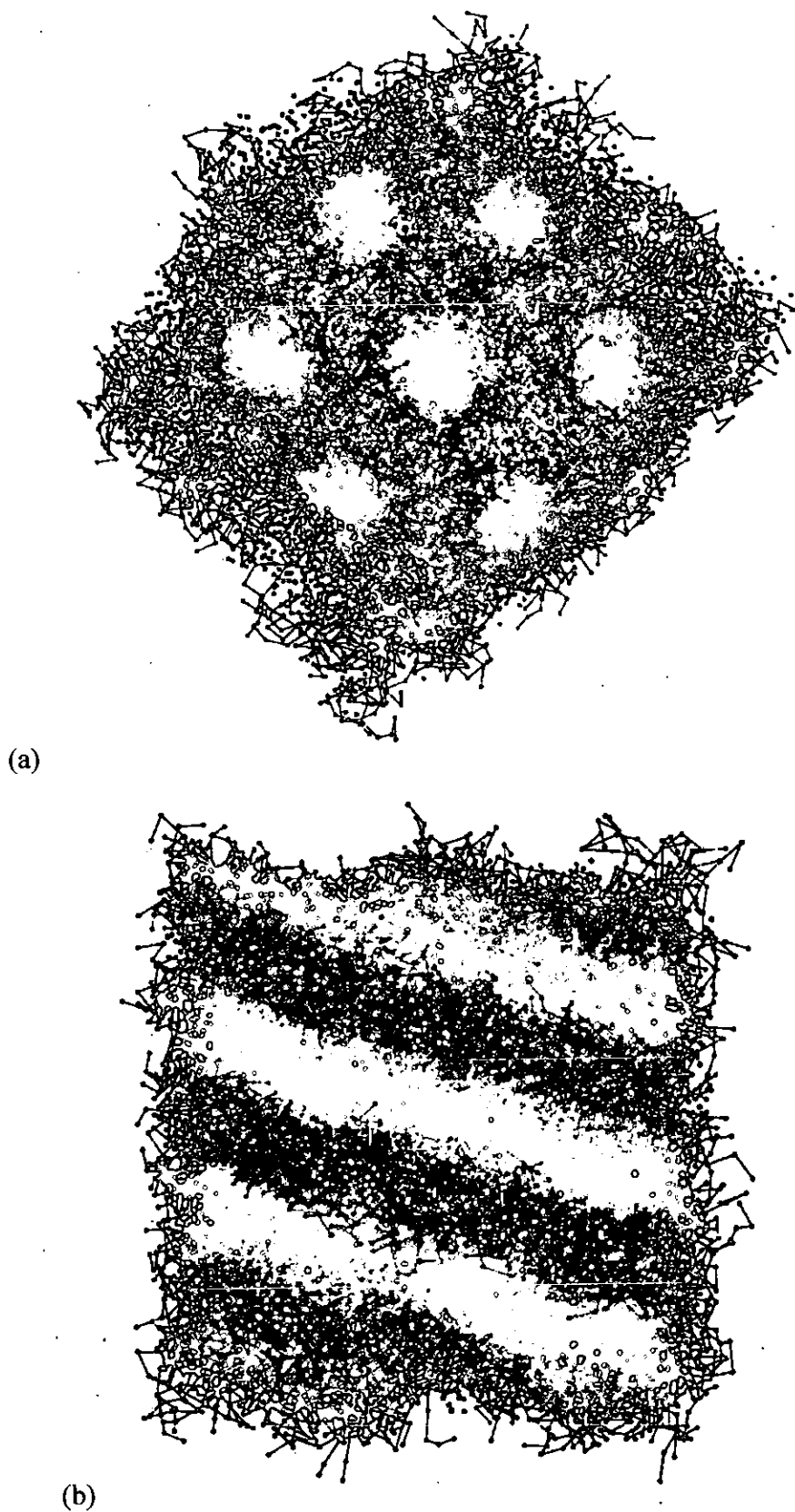


Figure 3.5 Bead-stick images of (a) H_1 phase, 60% and (b) L_α phase (90%). Dark blue represents head beads, light blue represents water beads and red represents tail beads.

3.5 Δa Phase Diagram

To determine which Δa value produces the best model (producing the best set of phases that compares well with experiment), a set of simulations was performed with different Δa values and The surfactant-water concentrations, resulting in a 2D phase diagram. For a simulation cube of side 14.5nm, concentrations between 50 and 100% by weight $C_{12}E_6$ were simulated for $\Delta a = 10, 15$ and 20 ($a_{ij} = 35, 40$ and 45 respectively). Simulations were performed until equilibrium was attained, and the results are shown in Figure 3.6.

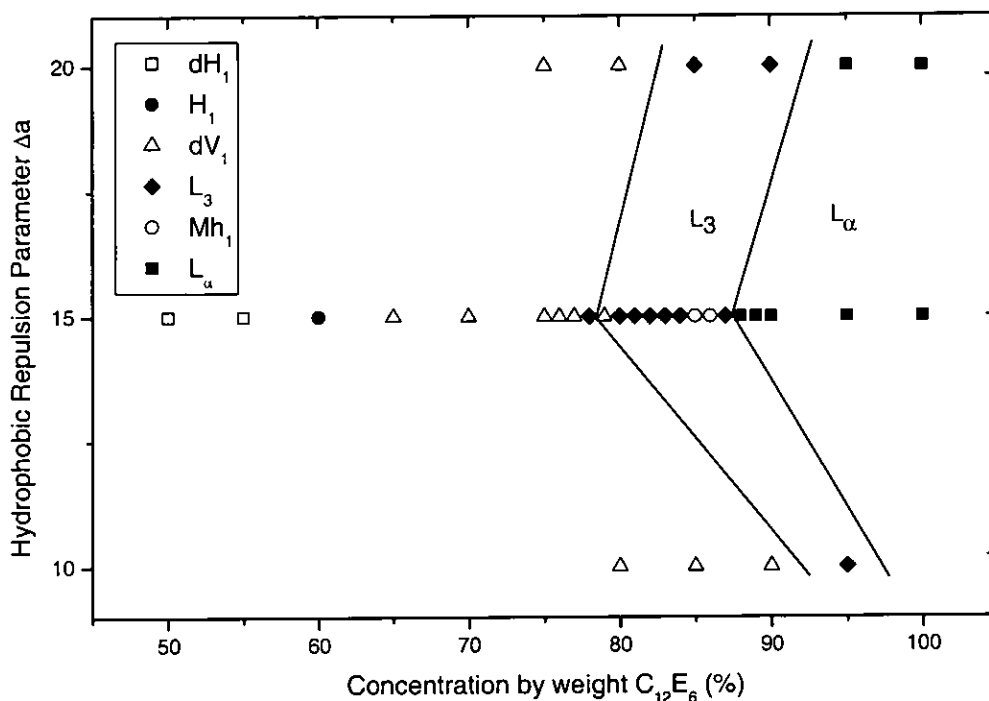


Figure 3.6 Phase Diagram showing phase sequence with different hydrophobic interaction parameters. Lines are a guide to the eye.

From Figure 3.6, it can be seen that the lamellar phase is most stable for $\Delta a = 15 \pm 5$. For $\Delta a = 10$, the excess repulsion is too low, so there is insufficient hydrophobic force for the lamellar phase to form until high concentrations. For $\Delta a = 20$, the excess repulsion seems to be too strong, and a sponge-like phase L_3 becomes stable where a lamellar phase should be found if the parameters were relaxed enough to allow it to form. The excess repulsion will therefore be chosen as $\Delta a = 15$ ($a_{ij} = 40$).

3.6 a_{BB} Phase Diagram

The above model represents a simplistic model for the interactions that drive the formation of the phases, where water beads interact with the head groups in exactly the same way as other water beads. Neglecting the fact that the head groups are part of a chain that makes the surfactant, the head and water beads are indistinguishable. In an effort to improve this by some degree, the head group to head group interaction parameter was considered. Polyoxyethylene chains readily form hydrogen bonds with water molecules^[4]. This is so much the case that it is more energetically favourable for water molecules to mix in between oxyethylene molecules in a polyoxyethylene-water mixture. This implies that the interaction parameter between head groups should be set slightly higher. A set of simulations were performed with varying concentrations using $\Delta a = 15$, changing a_{BB} , the repulsion parameter for head to head interactions from 25 (current value) to 35 (close to the hydrophobic repulsion parameter). The results of these simulations are shown in Figure 3.7.

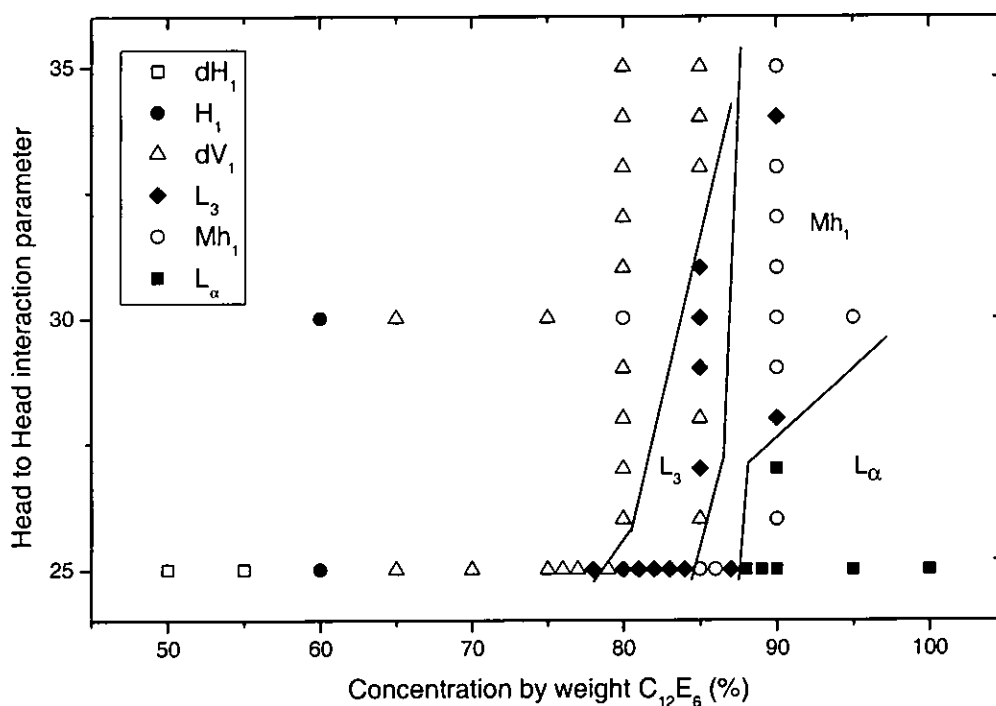


Figure 3.7 Phase Diagram showing phase sequences for different head to head interaction parameters. Lines are a guide to the eye.

Figure 3.7 shows that as the head to head interaction parameter is increased, phases with layer-like structure (sponge, mesh and lamellar) are destabilised in favour of phases that have positive surface curvature (e.g. bicontinuous). For example, with $a_{BB}=25$, the lamellar phase is present at 90%, but on increasing a_{BB} to 30, the lamellar phase is still not stable at 95%. It seems apparent that at these higher concentrations, where there are fewer water beads, there is a stronger repulsion between the head groups than the tail groups, which discourages the formation of layer like phases. As in experimental systems, the lamellar phase is quite stable, even at lower concentrations, it is appropriate to choose a_{BB} where these layer-like phases are most stable, so $a_{BB}=25$ will be chosen.

3.7 Box Sizes

To investigate the effect of the box size on the phases produced, a set of simulations were performed from 50-100% varying size from 8.75nm to 25nm. Simulations were performed for at least 100,000 time steps, although for some of the larger simulations more time steps were required. Again, simulations were all checked to ensure they fulfil the equilibrium criteria described in section 3.4. Figure 3.8 shows the results from this set of simulations.

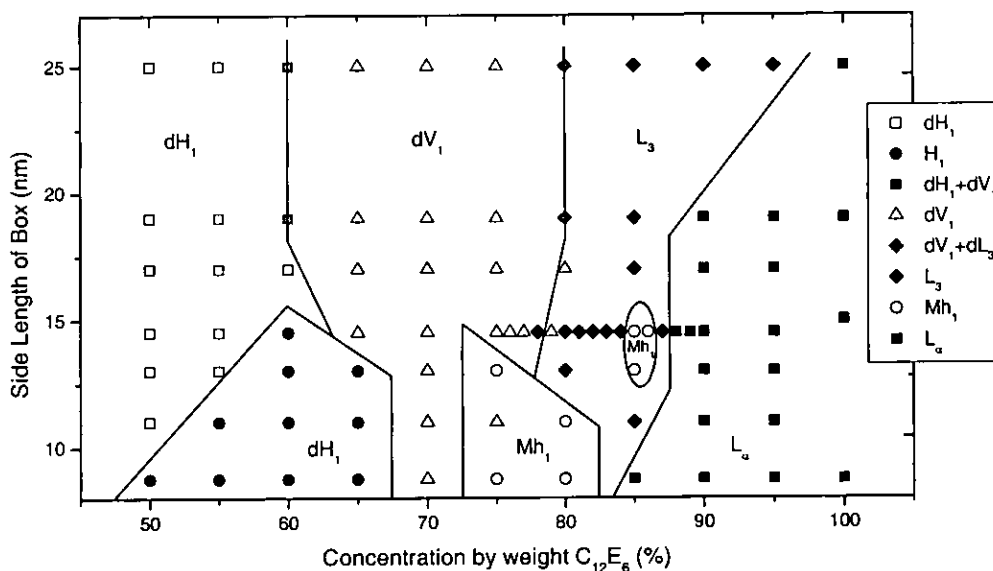


Figure 3.8 Phase Diagram showing phase sequence for different box sizes. Lines are a guide to the eye.

Starting from small size (8.75nm), the phase sequence is very clear, and the structures show a high degree of inter-aggregate order. The phase sequence is $H_1 \xrightarrow{67.5\%} dV_1 \xrightarrow{72.5\%} Mh_1 \xrightarrow{82.5\%} L_\alpha$. However, as the box size increases, the stability of these ordered phases decreases. The mesh phase region is not stable at box sizes larger than 11nm, and the hexagonal phase is not stable at box sizes larger than 13nm. In place of the H_1 phase, a dH_1 phase becomes dominant, and in place of the Mh_1 phase, the L_3 phase becomes dominant. Also the dV_1 phase becomes dominant over a larger concentration range; at 17nm it is stable from 60 to 80%. The stability range of the lamellar phase remains largely the same, 90% and higher, except for 25nm, where the lamellar phase is not stable until 100%. At 13 and 14.5nm there is a small region of a mesh phase between L_α and L_3 . This phase has fewer pores than the main mesh phase region, and is more like the random mesh phase ($Mh_1(0)$).

From this phase diagram it can be seen that the size of the simulation cell has a significant effect on the results of the simulation. The changes seem to be reduced as the box size increases above 17nm, above which the phase sequence remains fairly constant, however this is after the majority of the ordered phases have been lost. The question that needs to be asked here is, whether the smaller box size induces the ordered phases, or whether the larger box size destabilises the ordered phases.

Simulation box sizes are generally considered in relation to the cut off distance for interactions. If the box size is of the same order as the cut off distance, then one bead may have an interaction with itself, due to periodic boundary conditions. As an absolute minimum, a box size of at least three cut off distances is normally chosen. The cut off distance for these simulations is 0.65nm, and the smallest box size is 8.75nm, more than an order of magnitude higher than the cut off distance.

However, even at large box sizes compared to the cut off distances, finite box-size effects occur due to the periodic boundary conditions, as the phase structures have repeat distances much larger than the cut off distance. The box size should be at least twice the repeat distance for the phase structures. If both were of the same order, then the structure would be effectively interacting with the same part of the aggregate structure due to the boundary conditions. The repeat distance for the lamellar phase in these simulations is approximately 4nm, so the box size should be at least 8nm. One final consideration is that the boundary conditions limit the number of possible orientations of the phases, effectively quantizing the values for the repeat distances.

The smaller the box size is, the larger the quantization effect. This effect will be considered further in the next chapter.

In order to choose an appropriate box size, a compromise must be made between a large box where ordered phases are less stable and a small box where there are too few repeat distances of phases inside the simulation cell. 14.5nm has been chosen here as the H_1 phase is still stable and Mh_1 phases are stable, but where there is still enough for approximately 5-6 repeat distances of the lamellar phase.

3.8 Summary

All of the necessary parameters have been selected appropriately for the model, and has been applied to a binary system, and has shown that a model surfactant-water system can replicate the phases of the experimental system for a non-ionic system. On increasing surfactant concentration, the hexagonal, bicontinuous cubic, sponge, mesh and lamellar phases were present. The effect of box size was investigated and found that the size of the box had an impact on the phase diagram. An optimum box size was chosen to ensure that the phases were not too restricted by the boundary conditions if the box was too small, or whether ordered phases became destabilised at large box sizes.

The model can be extended by retaining these parameters and adding a third component to the model. In chapter 4, the ternary system with added oil will be investigated, and in chapter 5, the ternary system with added anaesthetics and alcohols will be considered. Table 3.1 shows a table summarising all of the parameters selected for the model from chapter 2 and 3.

Parameter	Value
Δt Time step	0.06τ
R_c cut off distance	0.65nm
$k_B T$ Reduced energy scale	1
a repulsion parameter for like beads	25
ρ number density of beads	3
Volume per bead	0.09nm^3
Length of bond	0.65nm
k spring constant for harmonic bonds	$100\epsilon\sigma^{-2}$
Δa Excess repulsion for unlike beads	15
Box side length	14.5nm

Table 3.1 Parameters and values selected for the model

3.9 References

1. JS Clunie, JF Goodman, PC Symons, *Transactions Faraday Society*, **65** 287 (1969)
2. "Infrared Band Handbook"; *Plenum Press*: (1963)
3. RD Groot, KL Rabone. *Biophysical Journal* **81** (2) 725 (2001)
4. K Rendall, GJT Tiddy. *Journal of the Chemical Society-Faraday Transactions I* **80** 3339 (1984)

4 Oil Addition

4.1 Introduction

In this chapter, the addition of small molecules to the surfactant water system is investigated. As established earlier in section 1.5.1, the addition of oil has one of two extreme behaviours ^[1,2]. Short chain oils (shorter than the alkyl tail of the surfactant) can be penetrating, whereby the oil sits between the tails and increases the effective surface area per surfactant head group but has little effect on the lamellar spacing (see Figure 1.16). Oils that are longer than the alkyl tail of the surfactant are swelling, whereby the oil forms an interlayer between the terminal CH₃ groups at the surfactant molecules of the bilayer. This increases the bilayer spacing while having no observable effect on the surface area per head group (See Figure 1.17).

4.2 Modelling Oil

The oils that were added are of a simple hydrocarbon nature, and possess the same qualities as the alkyl tail part of the surfactants modelled. Therefore it is convenient to model the oils in the same way as the tail beads of the surfactant, choosing exactly the same repulsion parameters, bond length and strength etc. For completeness sake, a penetrating oil (shorter than the surfactant tail), a swelling oil (longer than the surfactant tail), and finally an oil that has the same length as the surfactant tail were modelled. They were modelled in the same way as shown in the previous chapter, so that a chain of 3 hydrocarbons are represented by one DPD bead. Experimentally the addition of hexane, decane and octadecane has been studied in this laboratory ^[2] and these three oils were chosen as candidates to be modelled. Hexane (6 hydrocarbons), a penetrating oil, was modelled with two beads, octadecane (18 hydrocarbons), a swelling oil, was modelled with six beads and dodecane (12 hydrocarbons) was modelled with four beads. Schematics of these models are shown in Figure 4.1.

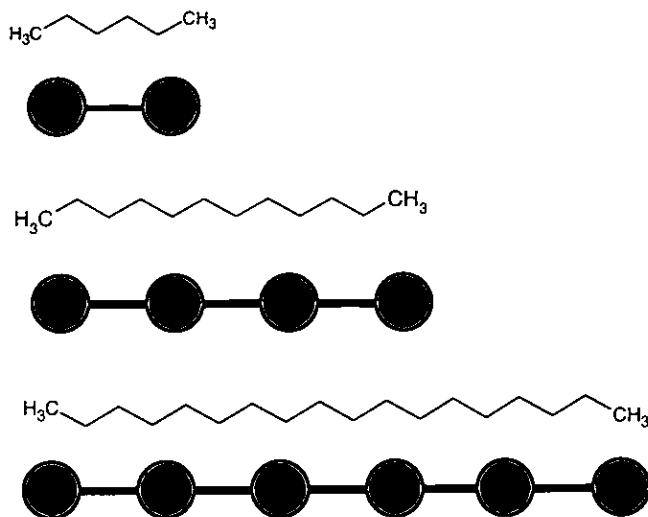
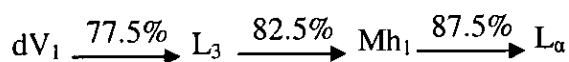


Figure 4.1 Molecular structure and DPD bead representation of the three oils added in the simulations.

4.3 Method

Oil was added to surfactant-water mixtures with five different surfactant to water mole ratios in the range from 0.12 to 0.75. This corresponded to the binary surfactant concentration by weight range of 75% to 95%, which exhibits the phase sequence:



The number of surfactant molecules, oil molecules and water beads in each simulation were calculated from the molecular weights of each of the molecules and the mole ratio of surfactant to water and the mole fraction of oil.

4.4 Oil Addition Results

4.4.1 Hexane

Hexane was added to 14.5nm and 8.75nm box sizes. This was to further test the impact of the box size investigated in the binary sequence by comparing the results of the addition of hexane for these box sizes. The phase diagrams showing the resultant phases from the addition of different mole fractions of hexane to different surfactant to water mole ratios are shown in Figure 4.2 (14.5nm simulation box) and Figure 4.3 (8.75nm simulation box).

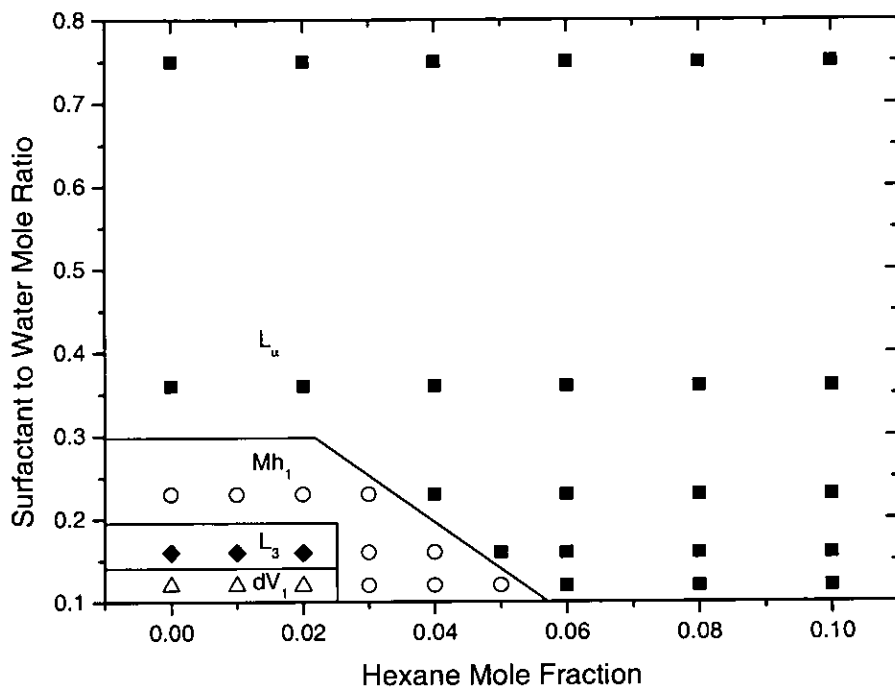


Figure 4.2 Phase diagram showing phases on increasing mole fraction of hexane (14.5nm box). Filled squares = L_∞ open circles = Mh_1 , filled diamonds = L_3 and open triangles = dV_1 . Lines are a guide to the eye.

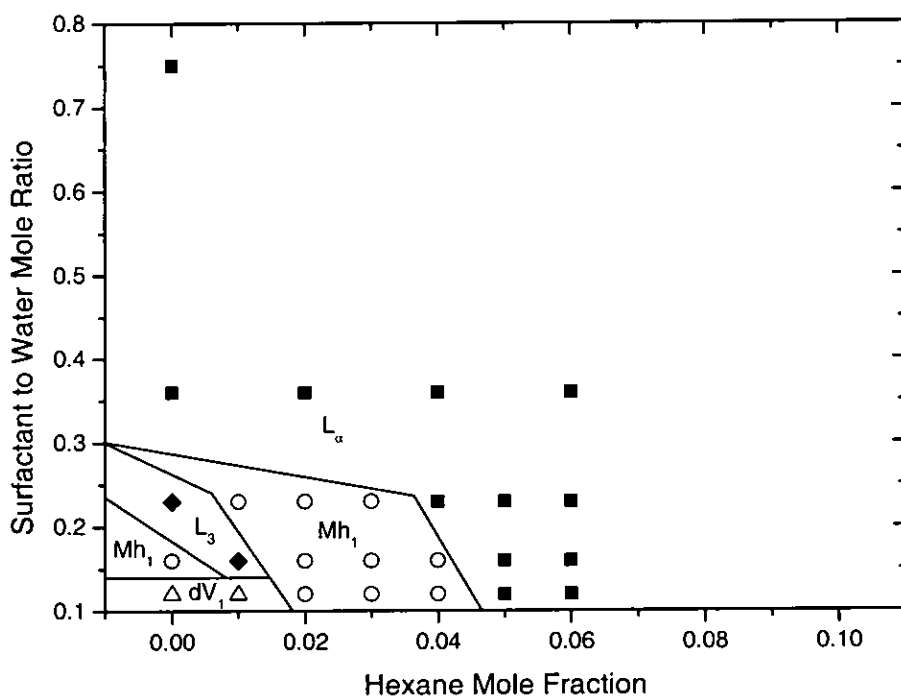


Figure 4.3 Phase diagram showing phases on increasing mole fraction of hexane (8.75nm box). Filled squares = L_∞ open circles = Mh_1 , filled diamonds = L_3 and open triangles = dV_1 . Lines are a guide to the eye.

For the 14.5nm box size, at $X_{sw} = 0.75$ and 0.36 , the addition of hexane has no effect on the phase structure, which remains as lamellar. At $X_{sw} = 0.23$, the mesh phase is stable until $\varphi_{hex}=0.03$, above which the lamellar phase becomes stable. This implies that the mesh phase is suppressed by the addition of hexane, and at sufficient hexane concentrations a lamellar phase is preferred. At $X_{sw} = 0.16$, the sponge phase is stable until $\varphi_{hex}=0.04$ where the mesh phase becomes stable. Above this concentration the lamellar phase is stable. This implies that the sponge phase is also suppressed by the addition of oil, allowing phases with less curvature to become more stable. At $X_{sw} = 0.12$, the disordered bicontinuous phase is stable but adding oil destabilises the dV_1 , L_3 and Mh_1 phases in favour of the lamellar phase. This shows that overall, adding hexane at various binary concentrations destabilises phases with more surface curvature in favour of those phases with less or no surface curvature.

For the 8.75nm box size, the same sequence of phases is observed on increasing hexane mole fraction. As the mesh phase is present in the binary phase sequence for the 8.75nm simulation box, the overall phase diagram is not the same, but comparing Figure 4.2 and Figure 4.3 shows that the phase boundaries are in similar positions. There are no qualitative differences in the phase diagrams for the different box sizes.

4.4.2 Dodecane

The phase diagram showing the resultant phases from the addition of dodecane to different surfactant to water mole ratios is shown in Figure 4.4.

At $X_{sw} = 0.23$, the mesh phase is destabilised by the lamellar phase at $\varphi_{dod}=0.02$. At $X_{sw} = 0.16$, the mesh phases becomes stable over the sponge phase at $\varphi_{dod} = 0.01$, and the lamellar becomes stable at $\varphi_{dod} = 0.03$. At $X_{sw} = 0.12$, the disordered bicontinuous phase is stable but the addition of dodecane destabilises the dV_1 , L_3 and Mh_1 phases in favour of the L_α phase. This shows that overall, as shown for hexane, that adding dodecane at various binary concentrations destabilises phases with more surface curvature in favour of those phases with less or no surface curvature.

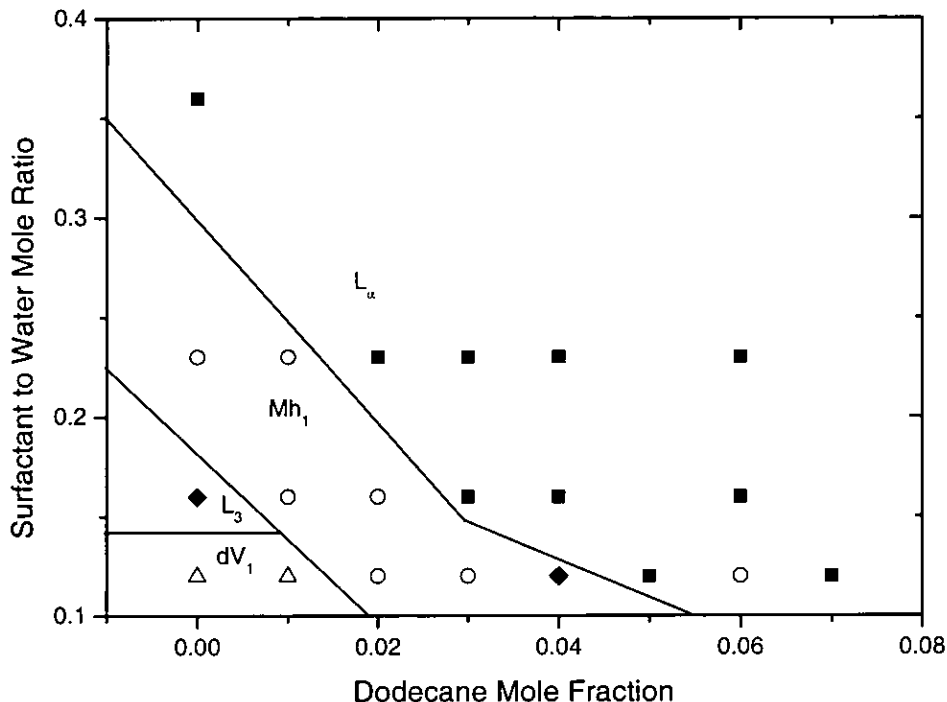


Figure 4.4 Phase diagram showing phases on increasing mole fraction of dodecane (14.5nm box). Filled squares = L_α , open circles = Mh_1 , filled diamonds = L_3 and open triangles = dV_1 . Lines are a guide to the eye.

4.4.3 Octadecane

The phase diagram showing the resultant phases from the addition of octadecane to different surfactant to water mole ratios is shown in Figure 4.5. Like the addition of dodecane, at $X_{sw} = 0.23$ the mesh phase is stable until $\phi_{oct} = 0.02$, where the L_α phase becomes stable. However, the phase sequence for the addition of octadecane at $X_{sw} = 0.16$ and $X_{sw} = 0.12$ are not as expected from experiment. At 0.16, the L_3 phase is stable until $\phi_{oct} = 0.05$, where the L_α phase is recovered (with no mesh phase found in between), and at $X_{sw} = 0.12$, the dV_1 phase remains stable even at $\phi_{oct} = 0.1$. This does not correspond with the experimental findings (reference [2], Figure 1.21) that the longer the molecule introduced, the lower the stability of phases with curvature.

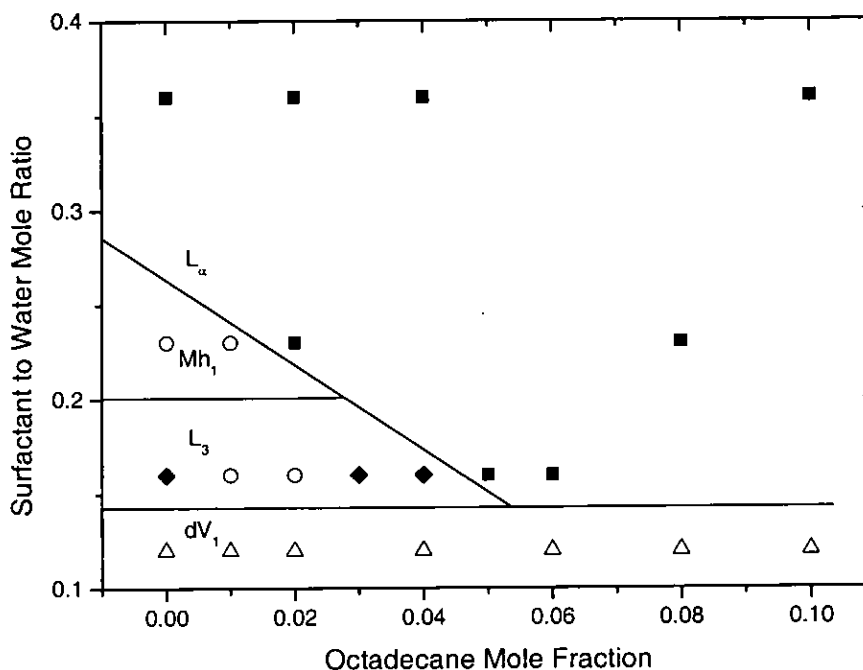


Figure 4.5 Phase diagram showing phases on increasing mole fraction of octadecane (14.5nm box). Filled squares = L_α , open circles = Mh_1 , filled diamonds = L_3 and open triangles = dV_1 . Lines are a guide to the eye.

4.4.4 Comparison of the Phase Diagrams

Comparing the phase boundaries of the addition of dodecane (Figure 4.4) with those for hexane (Figure 4.2) shows that the phases are destabilised at lower mole fraction of oil for dodecane than that for hexane. The boundary lines are steeper, and less molecules of dodecane are required to destabilise a certain phase than hexane molecules. This is consistent with experiment that shows the larger the molecule, the lower the mole fraction required to destabilise a given phase^[2]. This is to some extent due to the fact that the larger molecules have a larger volume, and will give a larger contribution to the alkyl chain volume fraction of the phase, thus effectively inducing a “higher concentration”, encouraging phases with lower surface curvature to form. To investigate this, the phase diagrams were drawn with oil volume fraction as the independent variable. These phase diagrams were overlaid on each other for ease of comparison and the result is shown in Figure 4.6. Isodensity images showing phase evolution upon the addition of hexane, dodecane and octadecane are shown in Figure 4.7.

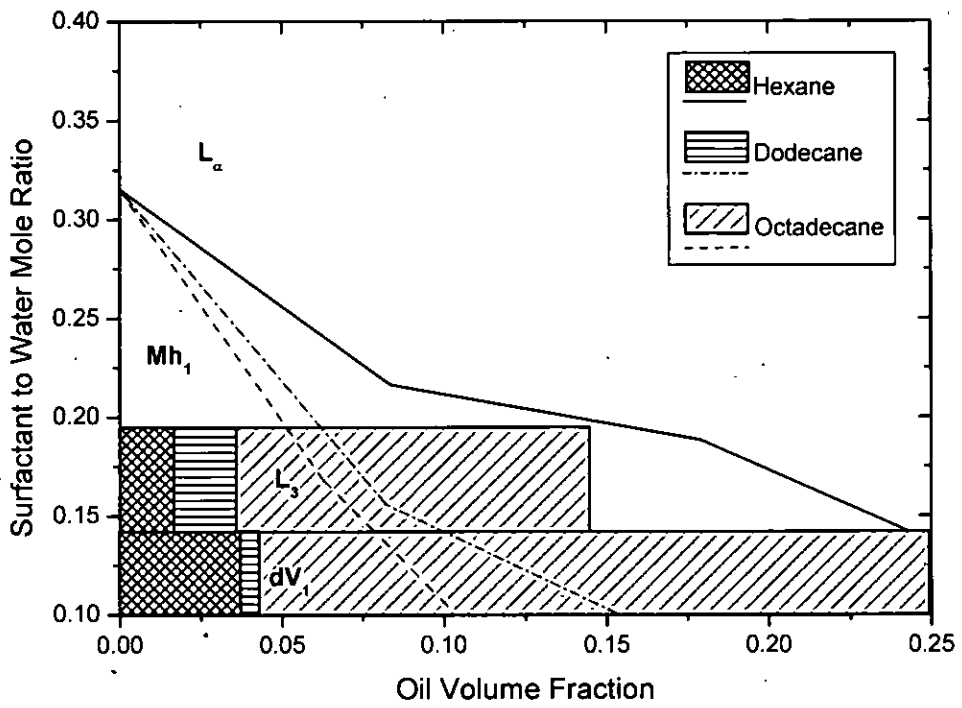


Figure 4.6 Composite Phase Diagram for all three oils as a function of oil volume fraction

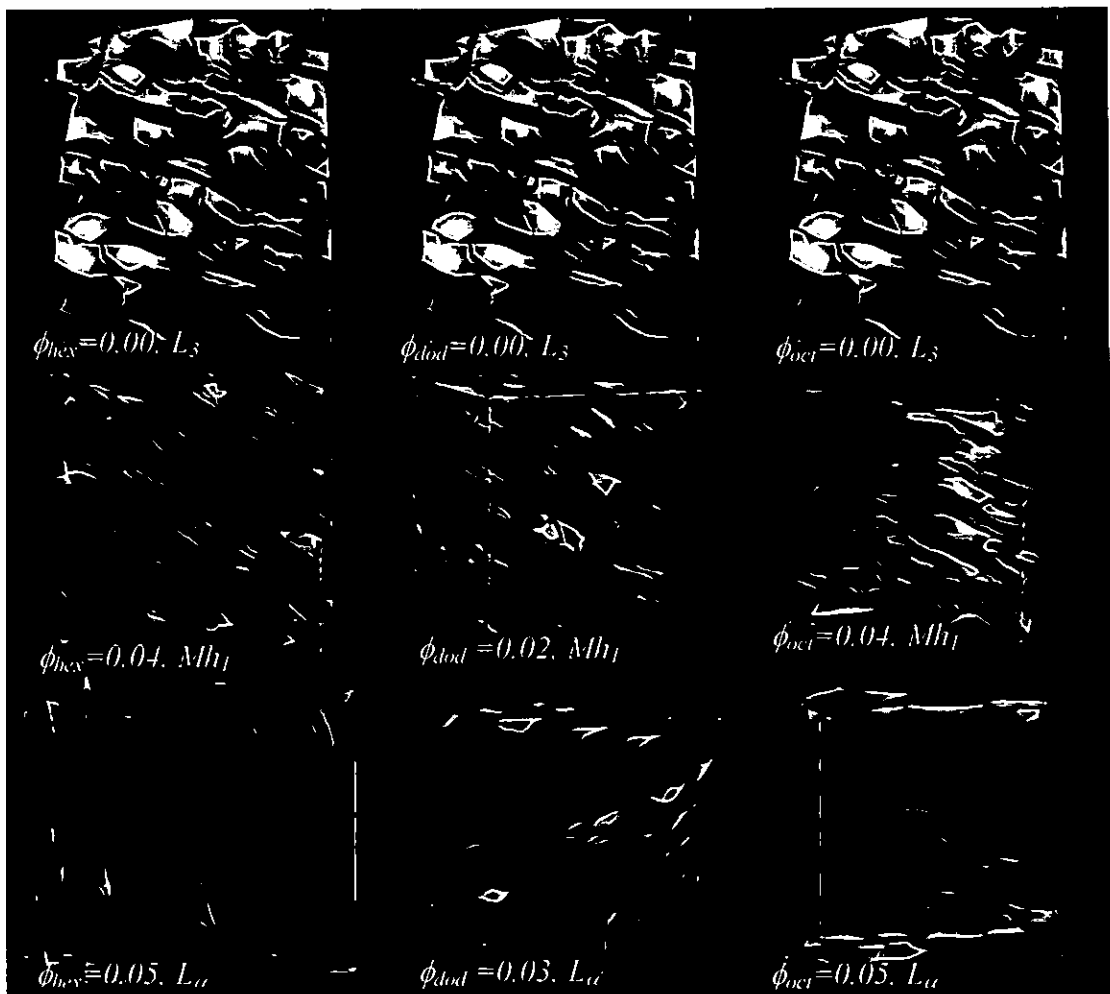


Figure 4.7 Isodensity images of phase structures on the addition of hexane (left), dodecane (middle) and octadecane (right) at $X_{sw} = 0.16$

Figure 4.6 shows that the phase boundaries for the addition of hexane and dodecane are now much more similar, with no significant differences. The only discernible difference is that the mesh to lamellar transition for dodecane is at slightly higher oil concentrations than for hexane at $X_{sw}=0.12$. As the phase boundaries for hexane and dodecane are similar, it may be that the phase changes that occur upon adding hexane and dodecane are due to the increasing volume of the alkyl chain bulking up the bilayer, where phases with less surface curvature are favoured.

However for octadecane, the phase transitions are at considerably higher oil concentrations than for hexane and dodecane. This is the case for all phase transitions. Therefore it is unlikely that the volume effect is driving the phase transitions for octadecane in the way it has for dodecane and hexane.

4.5 Analysis

4.5.1 d_0 Spacing and Oil Behaviour in the Tail Region

It is expected from experiment ^[2] that octadecane should behave as a swelling oil, whereas hexane should behave as a penetrating oil.

The swelling and penetrating behaviour can be quantitatively investigated by measuring the repeat distances of the lamellar phase as a function of the mole fraction of the oil added. This repeat distance or d_0 spacing (as adopted from x-ray scattering nomenclature) can be readily and conveniently measured from the simulation results. The most efficient way of doing this is by recording the orientation of the lamellar in relation to the box. This is done by counting how many repeat distances (d_0) are present with respect to each of the three dimensions of the simulation box. As periodic boundary conditions are in place, these numbers will all be integers. This limitation effectively quantizes the number of possible orientations, and therefore, the calculated d_0 spacings are also quantized. Let's say a lamellar has n_x repeats in the x direction, n_y repeats in the y direction and n_z repeats in the z direction (Figure 4.8a shows a lamellar phase with $n_x=3$, $n_y=2$ and $n_z=1$.) The x component of d_0 , will be L/n_x , where L is the side length of the simulation box. From this, the angle the x direction makes with the normal of the lamellar plane needs to be found, and simple trigonometry will provide the d_0 spacing.

To do this, let alpha be the angle between the x axis and the normal of the lamellae in the xy plane (see Figure 4.8b), and let beta be the angle between the x' axis and the true normal of the lamellae.

α and β can be calculated using the number of repeats in the y and z directions with the x direction thus:

$$\alpha = \arctan\left(\frac{n_y}{n_x}\right) \quad (4.1)$$

$$\beta = \arctan\left(\frac{n_z}{n_x} \cos(\alpha)\right) \quad (4.2)$$

Therefore the bilayer repeat distance can be defined as:

$$d_0 = \frac{L}{n_x} \cos(\alpha) \cos(\beta) \quad (4.3)$$

Therefore d_0 can be calculated if the size of the box is known and the number of repeat distances in each direction are recorded. This is a simple procedure, and averages out any undulations in the lamellar surface. Due to the finite size of L , and the discrete values n_x , n_y and n_z , d_0 is quantized. The degree of quantization is related to the size of the box, and as the size of the box used for the simulations is relatively small, this quantization effect needs to be taken into account when analysing the results for d_0 . This calculation for d_0 has been done for the addition of hexane, dodecane and octadecane in simulations at $X_{sw} = 0.75$ and oil mole fractions from 0.02 to 0.10 in 0.02 graduations. The results of these are shown in Figure 4.9.

This shows that the addition of hexane to the lamellar phase has no effect on the bilayer spacing. From 0.02 to 0.1 mole fraction, the orientation of the lamellar phase remains the same, and so the spacing is constant. However, as d_0 is quantized, the true d_0 value may slightly increase or decrease on increasing concentration. The addition of dodecane yields the same results until 0.08 mole fraction is added, where the orientation changes, indicating an increase in d_0 from 3.8 to 4.0nm. This shows that dodecane behaves as a swelling oil to some extent as after enough dodecane is added, d_0 rises.

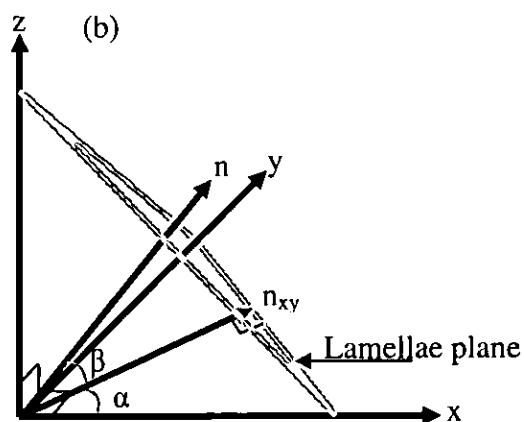
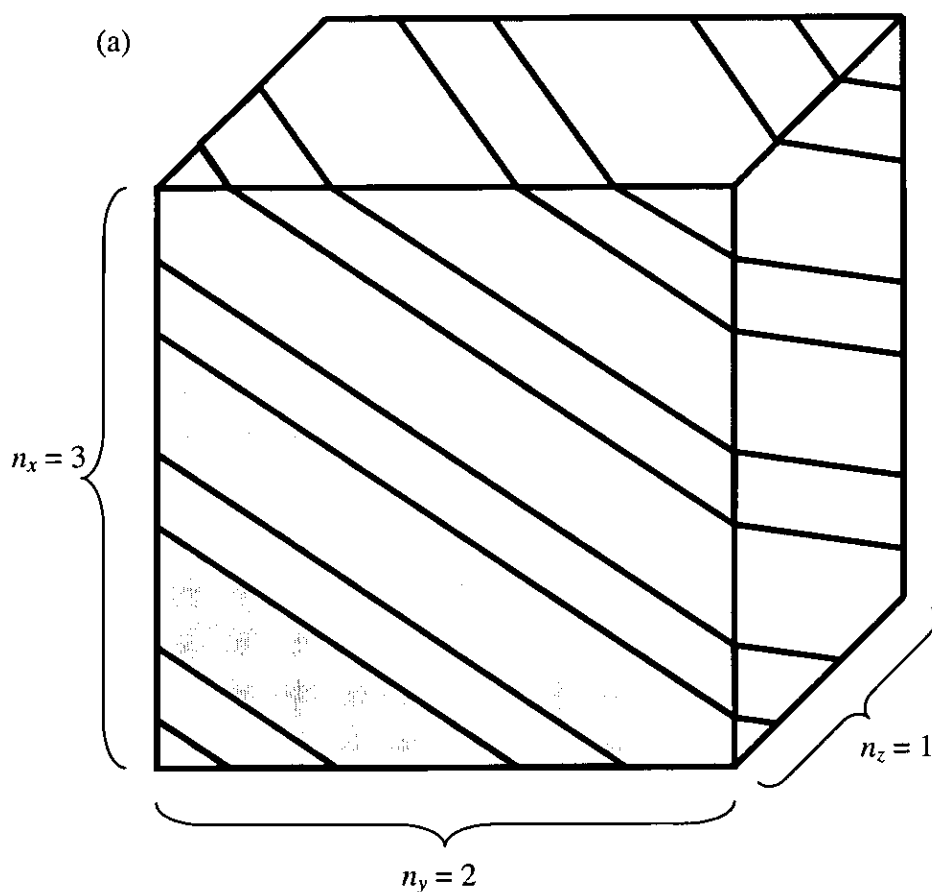


Figure 4.8 (a) Schematic of a simulation box with a lamellar phase orientated so that there are 3 repeats in the x direction, 2 repeats in the y direction and 1 in the z direction. (b) Schematic diagram showing the angles α and β , used to calculate d_0 . n_{xy} is a line normal to the lamellae plane residing in the xy plane. α is the angle between x and n_{xy} and β is the angle between n_{xy} and n , a line normal to the lamellae plane.

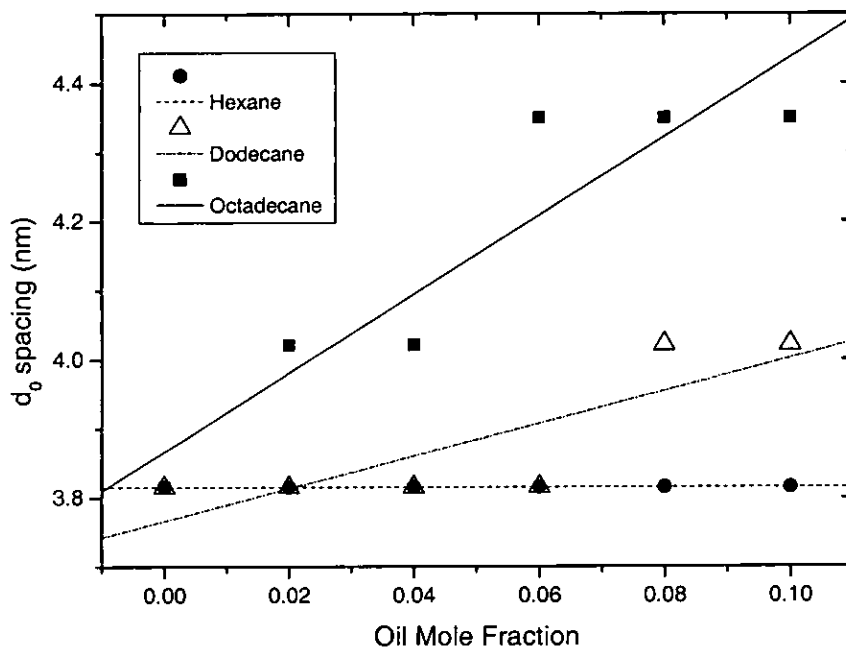


Figure 4.9 d_0 spacing as a function of oil mole fraction. Lines are least squares fit.

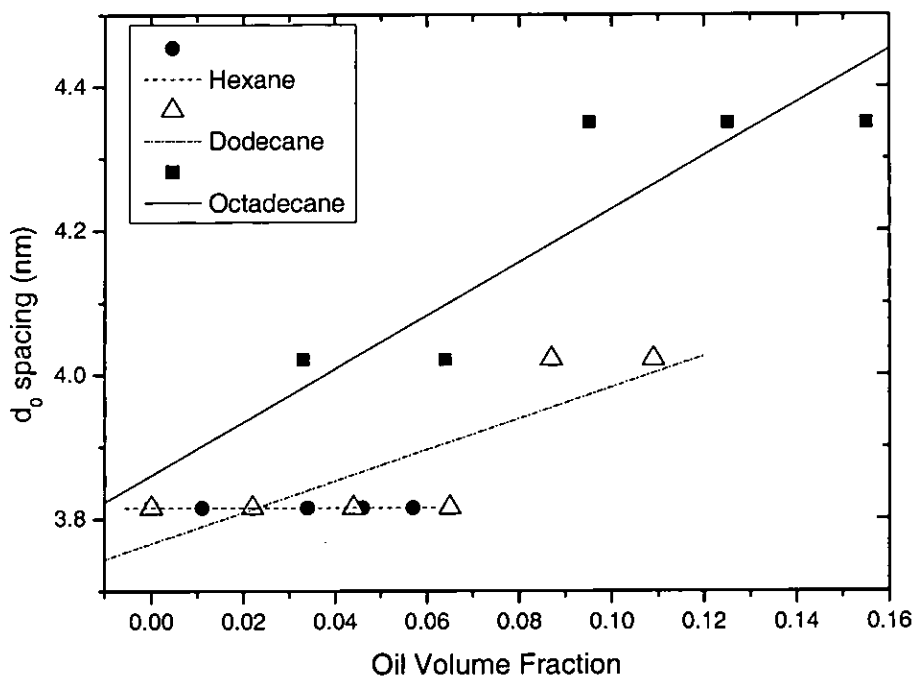


Figure 4.10 d_0 spacing as a function of oil volume fraction. Lines are least squares fit.

The addition of octadecane shows the most swelling behaviour, where at 0.02 and 0.04 mole fraction the spacing is increased to 4.0nm, and at 0.06 mole fraction it increases again to 4.3nm.

Figure 4.10 shows a composite graph of the d_0 spacings for each of the oils as a function of the volume fraction of oil. The gradients of the lines are still different, indicating that the effect of increasing the spacing is not entirely due to the volume of the oil beads expanding the layer. This implies that dodecane and octadecane behave increasingly like swelling oils, while hexane has little or no effect on the bilayer spacing. Figure 4.11 shows isodensity images of the lamellar phase on the addition of octadecane showing the different orientations of the lamellae with respect to the simulation box because of the swelling behaviour of octadecane.

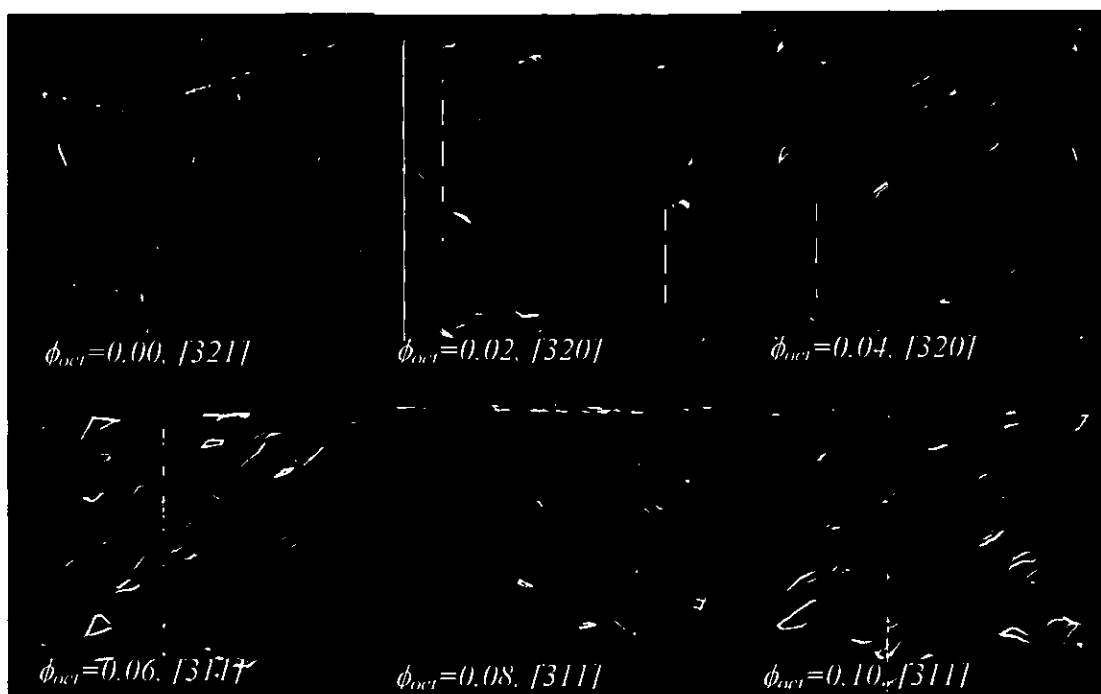


Figure 4.11 Orientations of lamellae in simulation box on increasing octadecane concentration. Orientation changes as lamellae thicken because of swelling behaviour of octadecane.

The effect of the oils on the bilayer can be investigated further by comparison to ideal penetrating and ideal swelling behaviour. Ideal penetrating behaviour assumes that the oil has no effect whatsoever on the hydrocarbon thickness of the bilayer, as the oils are situated in between surfactant tail chains. Ideal swelling behaviour assumes that the effective surface area per head group remains constant, as all of the oil is situated between the interlayer of the chain.

To derive an equation that gives d_0 as a function of oil concentration, the bilayer spacing d_0 is related to the bilayer (tail) thickness, d_{hc} and the alkyl chain volume fraction, φ_{alkyl} (components that reside in the bilayer, including the tail and the oil).

Firstly, derive an equation for φ_{alkyl} :

$$\phi_{alkyl} = \frac{v_t N_t + v_o N_o}{v_t N_t + v_o N_o + v_h N_h + v_w N_w} \quad (4.4)$$

Where v and N represent the volume and number of molecules of each constituent and the subscripts t , o , h , and w represent the tail, oil, head and water components respectively.

As $N_t = N_h$, and the oil to surfactant mole ratio $X_{os} = N_o/N_t$ and the surfactant to water mole ratio $X_{sw} = N_s/N_w$, the equation can be modified to:

$$\phi_{alkyl} = \frac{v_t N_t + v_o N_t X_{os}}{v_t N_t + v_o N_t f + v_h N_t + v_w N_t X_{sw}}$$

N_t now be eliminated, leaving:

$$\phi_{alkyl} = \frac{v_t + v_o X_{os}}{v_t + v_o f + v_h + v_w X_{sw}} \quad (4.5)$$

In the binary mixture, X_{os} is zero, so the equivalent binary equation is:

$$\phi_{alkyl}^0 = \frac{v_t}{v_t + v_h + v_w X_{sw}} \quad (7.6)$$

This derivation for d_0 for a penetrating oil uses the fact that it is assumed that the bilayer thickness remains constant, so $d_{hc} = d_{hc}^0$, where d_{hc}^0 is the bilayer thickness for the binary mixture.

$$d_0 = \frac{d_{hc}^0}{\phi_{alkyl}} \quad (7.7)$$

For a binary mixture the equation becomes:

$$d_0^0 = \frac{d_{hc}^0}{\phi_{alkyl}^0} \quad (7.8)$$

Substituting equation 4.8 into equation 4.7 gives:

$$d_0 = d_0^0 \frac{\phi_{alkyl}^0}{\phi_{alkyl}} \quad (4.9)$$

On increasing oil concentration, ϕ_{alkyl} increases, thus decreasing d_0 . This indicates that the ideal penetrating behaviour of the oil encourages the head and water part of the bilayer to contract, as d_{hc} is assumed to be constant.

To derive the corresponding equation for ideal behaviour of a swelling oil, it is the effective surface area per head group S_a that remains constant. This is related to the effective alkyl chain volume per surfactant $(v_t + v_o X_{os})$ and half the length of the tail region by:

$$S_a = \frac{2(v_i + v_o f)}{d_{hc}} \quad (4.10)$$

Substituting $d_{hc} = d_0 \phi_{alkyl}$ into equation 4.10 gives:

$$S_a = \frac{2(v_i + v_o X_{os})}{d_0 \phi_{alkyl}} \quad (4.11)$$

For ideal swelling behaviour, it is assumed that S_a is constant, and will be the same as S_a for the equivalent binary mixture, which is given by:

$$S_a^0 = \frac{2v_i}{d_0^0 \phi_{alkyl}^0} \quad (4.12)$$

Thus as $S_a = S_a^0$ for an ideal swelling oil, equations 4.11 and 4.12 can be combined to give:

$$d_0 = d_0^0 \frac{\phi_{alkyl}^0}{\phi_{alkyl}} \frac{(v_i + f v_o)}{v_i} \quad (4.13)$$

This ideal penetrating and swelling behaviour can now be compared to the simulation results to compare the d_0 spacing for hexane and octadecane against predicted values for ideal penetrating and swelling behaviour. This is shown in Figure 4.12.

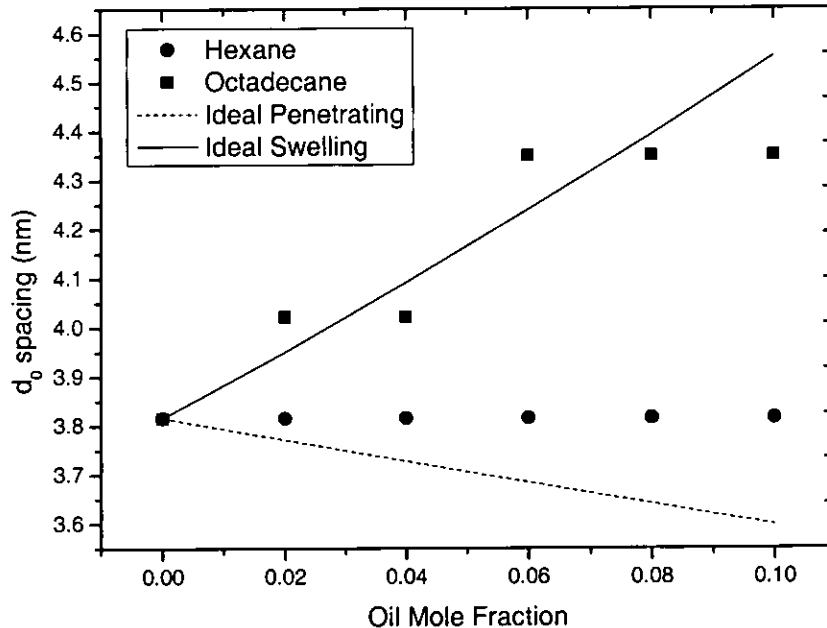


Figure 4.12 Ideal penetrating and swelling behaviour for hexane and octadecane respectively, compared to simulation results.

This figure shows that for hexane, there is no change in the d_0 spacing which differs from theory, which shows that the bilayer spacing should decrease on increasing

hexane concentration, and hexane therefore doesn't act completely as a penetrating oil. Although the d_0 values for hexane are quantized, the error bars for hexane, taken to be half the difference from one d_0 value to the next, lie above the ideal penetrating line, indicating that there would have been an orientation change if hexane were to have been behaving as an ideal penetrating oil. Octadecane simulation points lie pretty much on the curve predicted for ideal swelling behaviour.

Another comparison between theory and simulation results can be made for the surface area per head group (S_a) as a function of oil mole fraction. For octadecane which ideally behaves as a swelling oil, should have no effect on S_a , which in this case is assumed to be a constant. However, the penetrating hexane should increase S_a , and the amount it should increase ideally can be predicted.

Substituting equation 4.9 for d_0 for ideal penetrating oil into equation 4.10 for S_a gives:

$$S_a = \frac{2(v_i + fv_o)}{d_0^0 \phi_{alkyl}^0} \quad (4.14)$$

From this equation it is shown that ideal penetrating behaviour leads S_a to increase on increasing oil concentration.

S_a values for hexane and octadecane were calculated from equation 4.10 and were compared to the theoretical values from equation 4.14 and are shown in Figure 4.13.

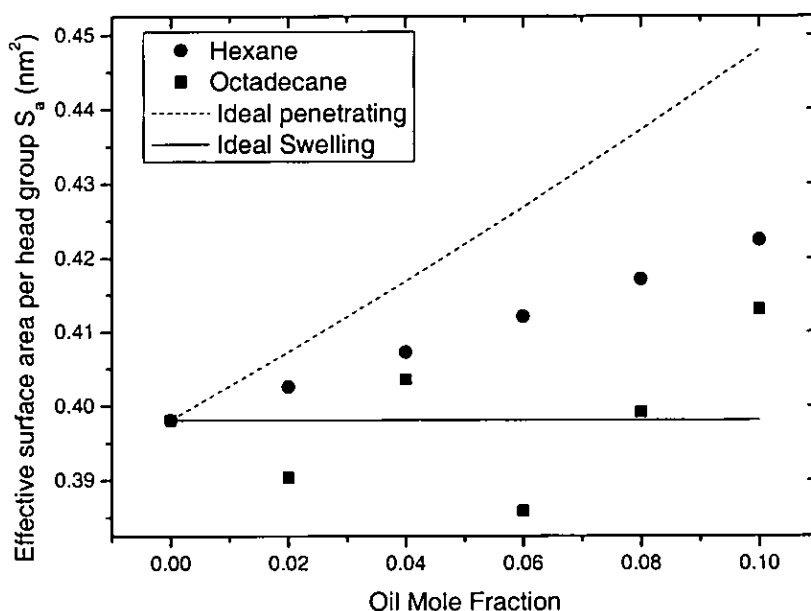


Figure 4.13 Surface area per head group for ideal penetrating and swelling behaviour

The Surface area for Octadecane addition remains constant, as expected from ideal swelling behaviour, so this shows that octadecane is a swelling oil. For hexane, there is a steady increase but not as high as ideal penetrating behaviour predicts.

It is known from previous work that hexane behaves as a penetrating oil and that octadecane behaves as a swelling oil^[1]. To elucidate whether dodecane behaves like a penetrating or swelling oil, d_0 and S_a values were calculated from simulation results and compared to ideal values for dodecane. Graphs showing d_0 and S_a are shown in Figure 4.14 and Figure 4.15 respectively.

Both of these graphs show that the dodecane behaves in intermediate between ideal penetrating and swelling behaviour, indicating that some dodecane molecules lie in the interlayer region while some dodecane molecules or at least part of them lie between the tails.

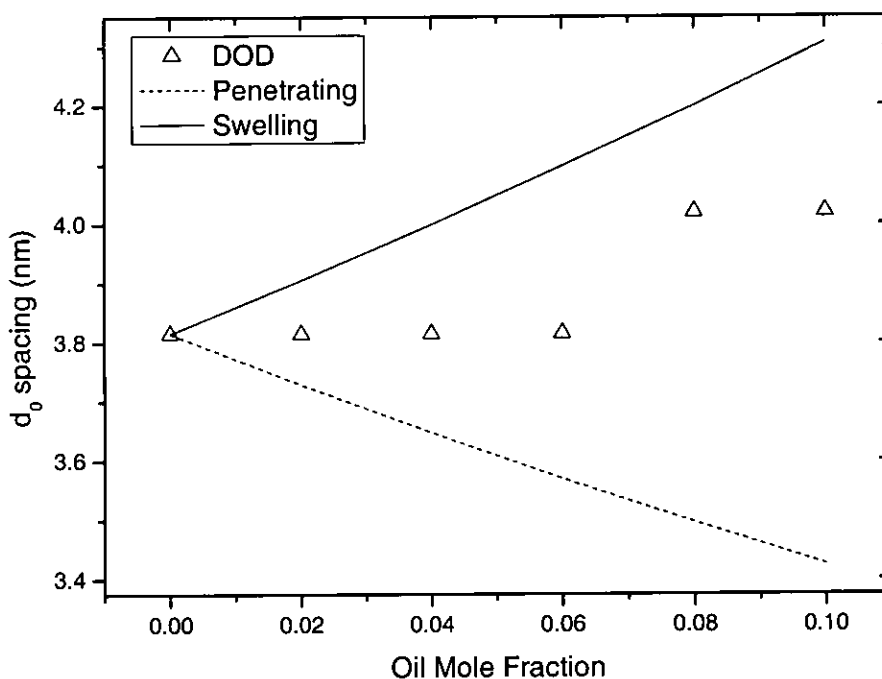


Figure 4.14 Ideal penetrating and swelling behaviour for dodecane

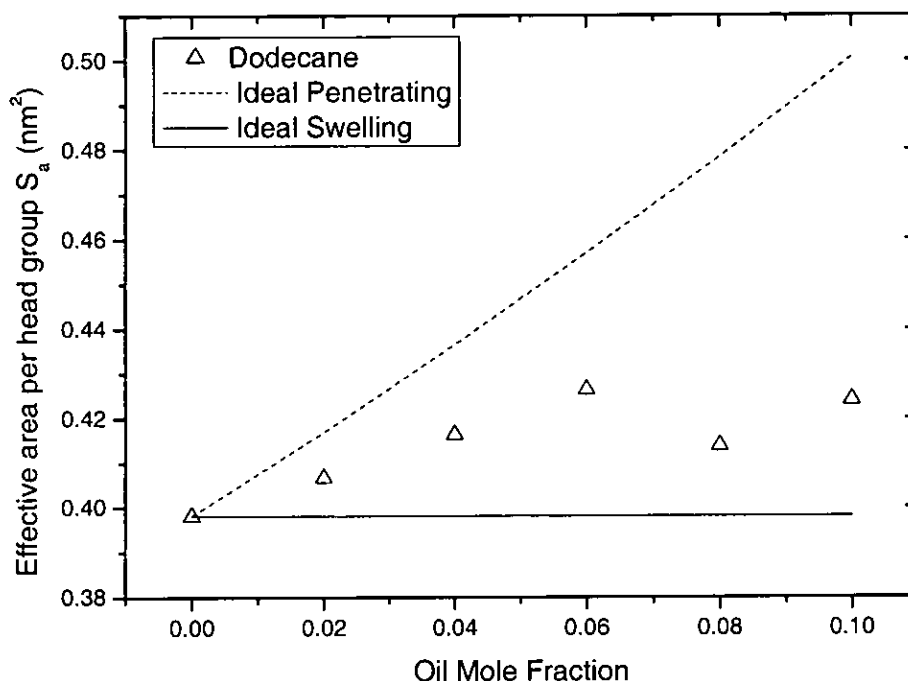


Figure 4.15 Surface area per head group for Ideal penetrating and swelling behaviour for dodecane

4.5.2 Probability Density Functions of Lamellar Phases

To investigate where the oils are located within the tail region, probability density functions of the lamellar phases were plotted for each of the three oils at differing concentrations of added oil. These were all taken at $X_{sw}=0.75$. To investigate extreme penetrating behaviour, a fourth oil, butane was simulated at $X_{sw}=0.75$, resulting in lamellar structures, so extreme penetrating and swelling behaviour can be investigated. These probability density function plots were created by taking the coordinates of every bead from the output file and using a program to read the coordinates and use them to create a density profile across the complete repeat distance for the tail, head, oil and water beads. A succinct description of the source code for the program, written in C++, appears in appendix B.

Figure 4.16 shows an example of the probability density functions produced for all types of beads across a single lamellar layer.

For all of the Probability density functions, the two largest peaks are for the tail and head beads. The oil bead peak is in the same position as the tail peak and the water peak is in the same position as the head peak.

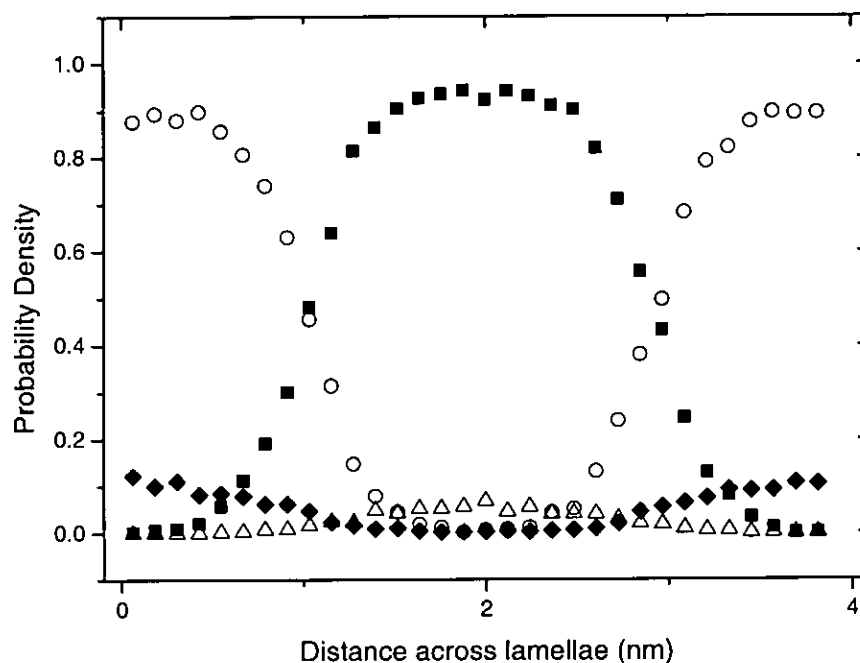


Figure 4.16 Typical probability density function across lamellar phase showing tail, head, water and oil beads. Graph shown is of 0.04 hexane mole fraction, $X_{sw}=0.75$. Filled squares = tail, open circles = head, filled diamonds = water and open triangles = oil beads.

To show how the addition of oil affects the probability distribution in the alkyl chain region, nested plots of the oil and tail probability density functions are presented in Figure 4.17.

As the concentration of butane and hexane increases, the oil bead peak gets taller, and the tail peak gets correspondingly shorter. The tail peak also flattens slightly at large concentrations of hexane. On increasing the concentration of dodecane the oil gets larger, and the dodecane peaks are larger than the hexane peaks for the same oil mole fraction. The tail peak gets shorter on increasing concentration, and at high concentrations the tail peak starts to split into two peaks. On increasing concentration of octadecane the tail peak again gets taller, and the octadecane peaks are larger than the dodecane peaks for the same oil mole fraction. As for dodecane, the tail peak gets smaller and splits into two.

A further set of nested plots have been plotted using the same data, plotting oil and tail probability density functions for a single oil concentration, showing the effect of the addition of different lengths of oil. These plots are shown in Figure 4.18.

Increasing the length of oil increases the size of the peak for the oil probability density, as expected. For the tails, at low concentration the longer oils decrease the

peak, and for higher concentrations the longer oils cause the peak to separate into two distinct peaks, indicating swelling behaviour. Shifts in peak locations are due to a change in lamellar repeat distance.

Using these probability density functions, the behaviour of the added oil can be analysed by considering the width of the oil and tail peaks, and how they change on increasing concentration for each of the three oils. This can be done by measuring the full width of the peak at half maximum height (FWHM), which was done using a curve fitting application on Origin, a scientific graphing and data analysis software package, fitting the curves to Gaussian curves. Peaks that were split into two were fitted using two individual Gaussian curves, and the overall width for these was considered to be the peak separation plus the average of the two FWHMs. Figure 4.19 shows the results for the oil peak widths and Figure 4.20 shows the results for the tail peak widths.

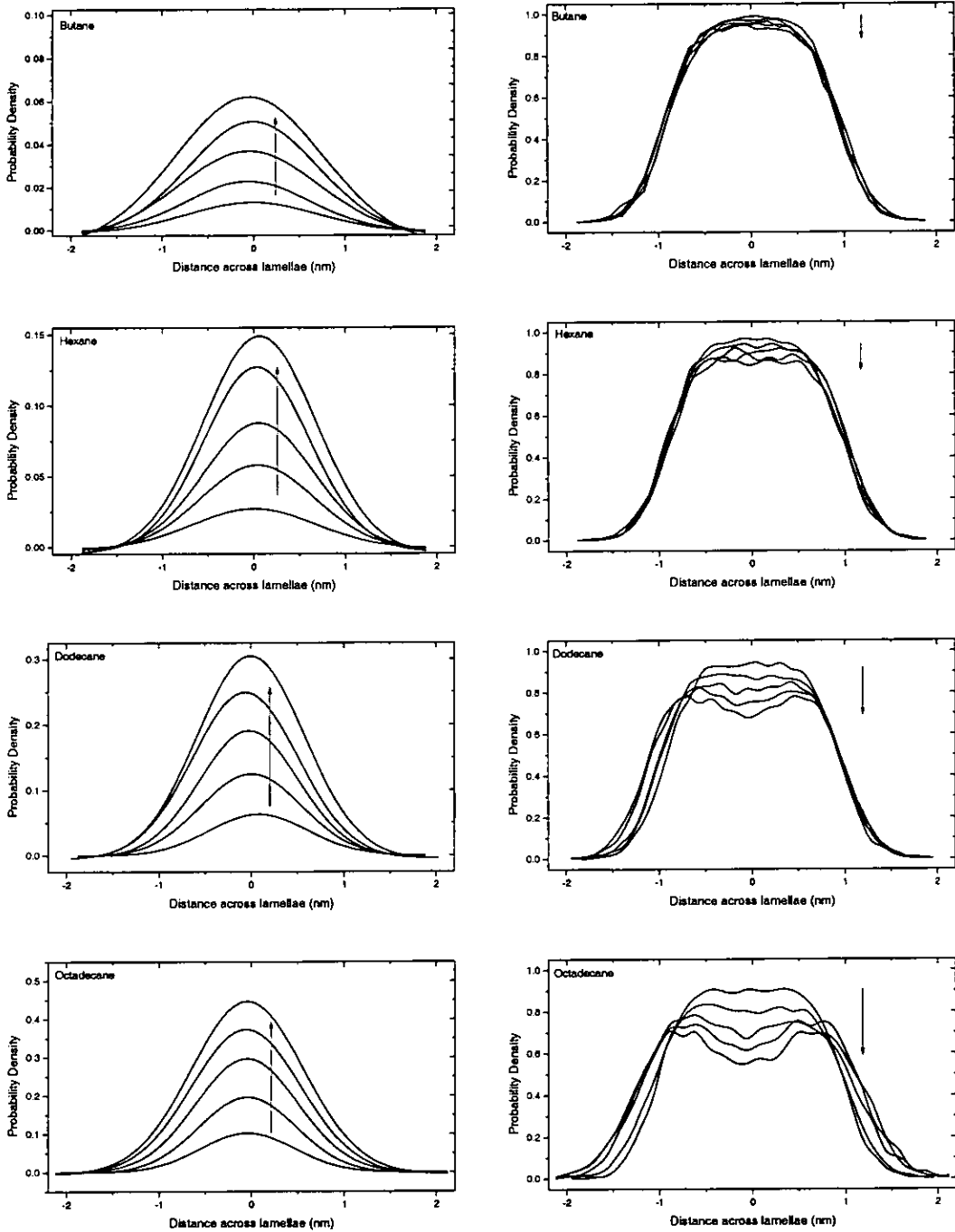


Figure 4.17 Probability density functions for oil (left) and tail (right) beads for oils. Arrows indicate increasing oil concentration.

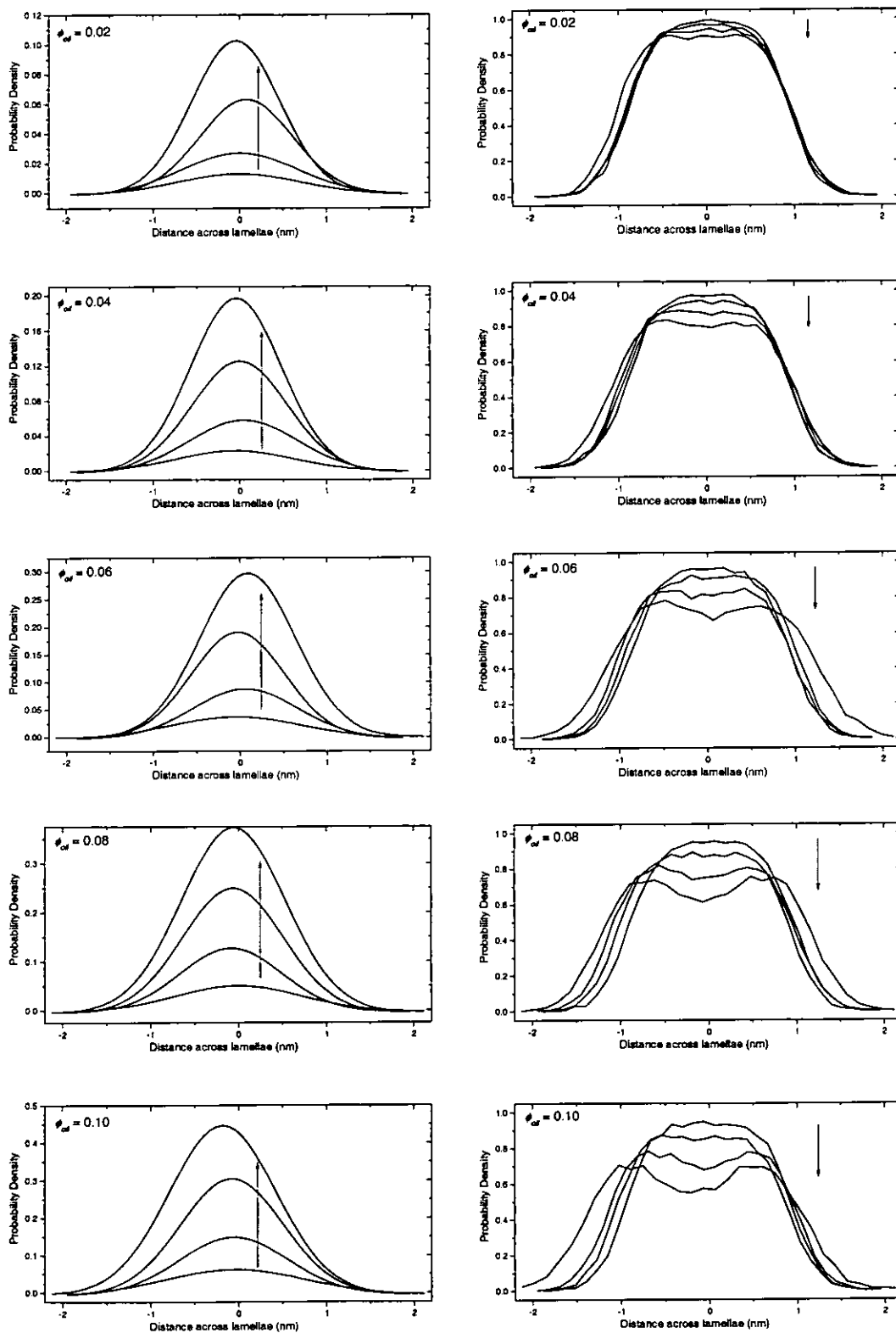


Figure 4.18 Probability density functions for oil (left) and tail (right) beads from low to high concentrations (top to bottom). Arrows indicate the increasing length of oil (butane, hexane, dodecane and octadecane).

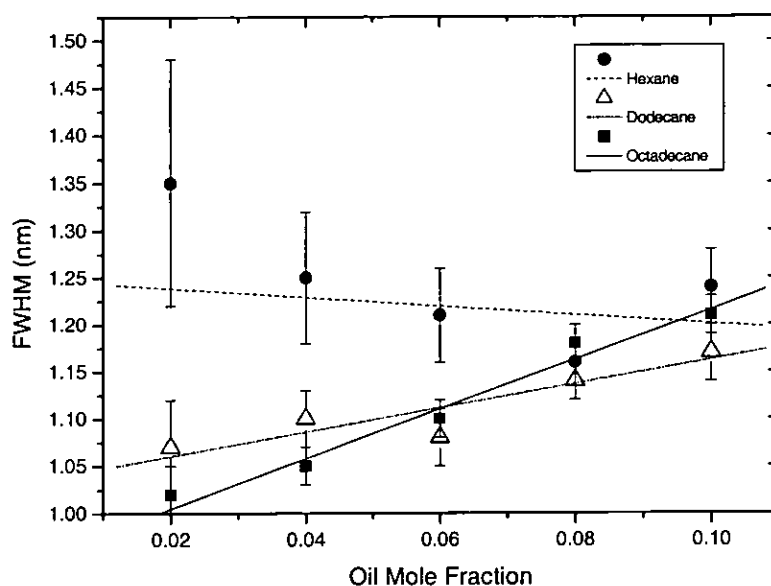


Figure 4.19 Oil FWHM for increasing oil mole fraction. Lines are least squares fit.

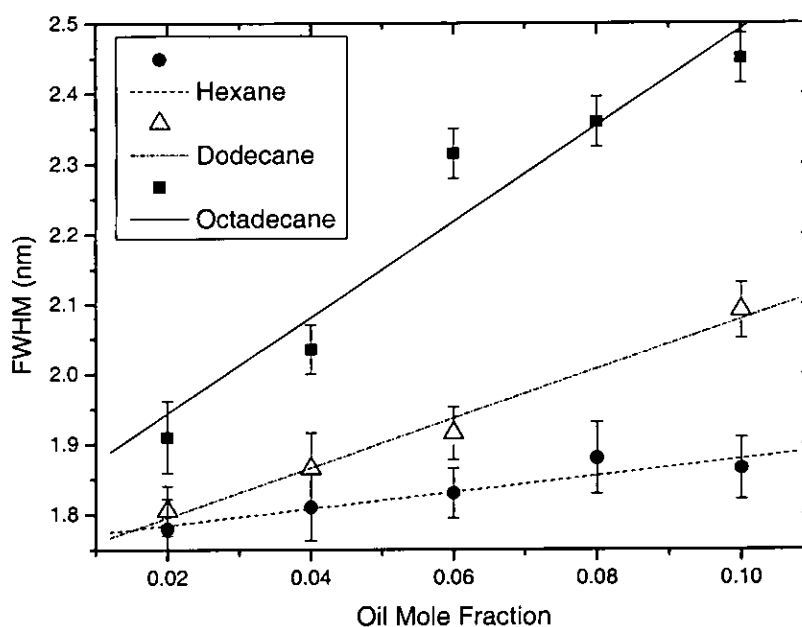


Figure 4.20 Tail FWHM for increasing oil mole fraction. Lines are least squares fit.

At low ϕ_{oil} , the hexane FWHM is relatively high, and higher than that of the dodecane or octadecane. High FWHM suggests that oil is more spread across the tail region, suggesting more penetrating behaviour. However, the oil FWHM for hexane decreases on increasing oil concentration, while the tail FWHM remains constant, suggesting that hexane behaves less like a penetrating oil at high concentrations. Dodecane has a lower oil FWHM at low concentrations, and octadecane has the smallest oil FWHM at

low concentrations. These low FWHM values suggest that the oil is spread over a narrow part in the centre of the tail region, suggesting swelling behaviour. For both dodecane and octadecane, increasing the concentration of oil increases the oil FWHM, but the gradient for octadecane is higher. Correspondingly, the tail FWHM for dodecane and octadecane also increase with increasing concentration, where the highest gradient is for the tail for the octadecane simulations, showing that the swelling behaviour doesn't change significantly at high concentrations.

4.5.3 Tail Bead Probability Density Functions

The behaviour of the oils can be further elucidated if probability density functions of the individual tail beads are plotted. For this the four tail beads are labelled 1 to 4, where bead 1 is the bead that includes the terminal CH_3 group, situated in the centre of the bilayer, bead 2 and bead 3 are the next beads up and bead 4 is closest to the interface region. These probability density functions were created using a modified version of the same program, and an example of these probability density functions is plotted in Figure 4.21, showing the probability density for each individual tail bead across a single lamellar layer. A succinct description of the source code for the modified program appears in appendix C.

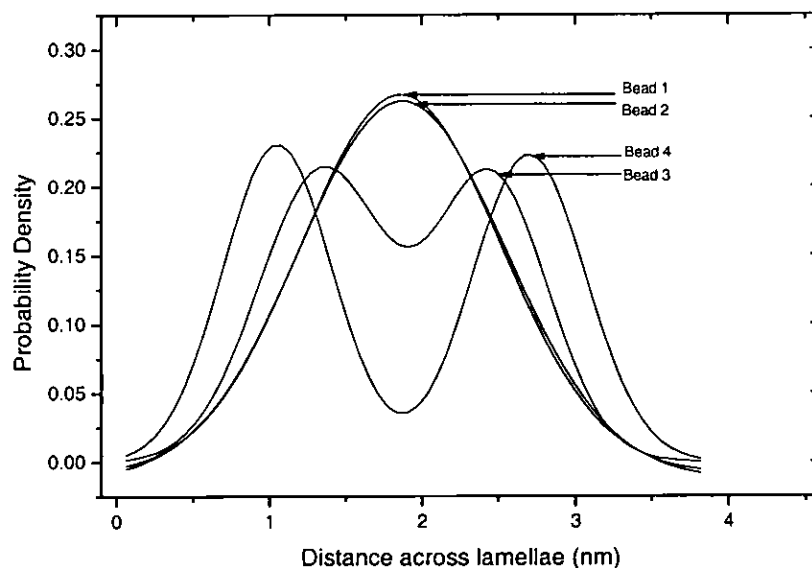


Figure 4.21 Tail Bead Probability Density Function example

In theory, the expected probability density functions for all of the beads should be two distinct Gaussian peaks, with a separation that increases from bead 1 to 4, as the distance between them across the layer increases. However, for all oils, beads 1 and 2

are single Gaussian peaks which cannot be resolved into two separate peaks. Beads 3 and 4 are resolved into two peaks. This indicates that the distribution of the tails towards the centre of the tail region is not as simple as expected.

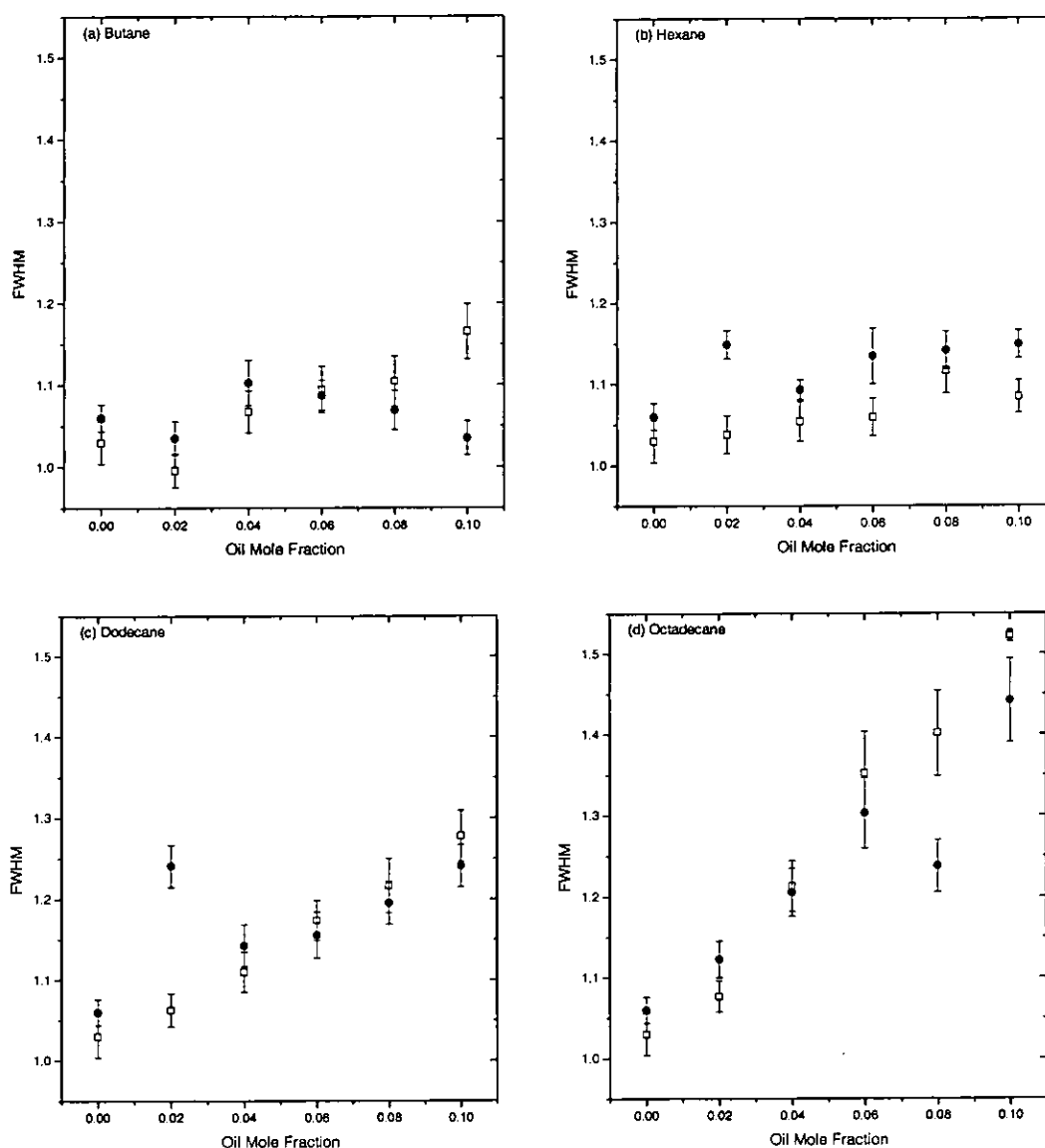


Figure 4.22 FWHM for beads 1 and 2 for (a) butane, (b) hexane, (c) dodecane and (d) octadecane. Filled circles = bead 1 and open squares = bead 2.

The distance between a bead on one tail and the same bead on the other side of the bilayer is related to the breadth of the peaks. For beads 1 and 2, the FWHM was measured, but for beads 3 and 4, which were considered as two separate peaks, the separation of the peaks was measured. The FWHM for beads 1 and 2 for the oils as a function of oil concentration is shown in Figure 4.22. The peak separation for beads 3 and 4 for the oils as a function of oil concentration is shown in Figure 4.23.

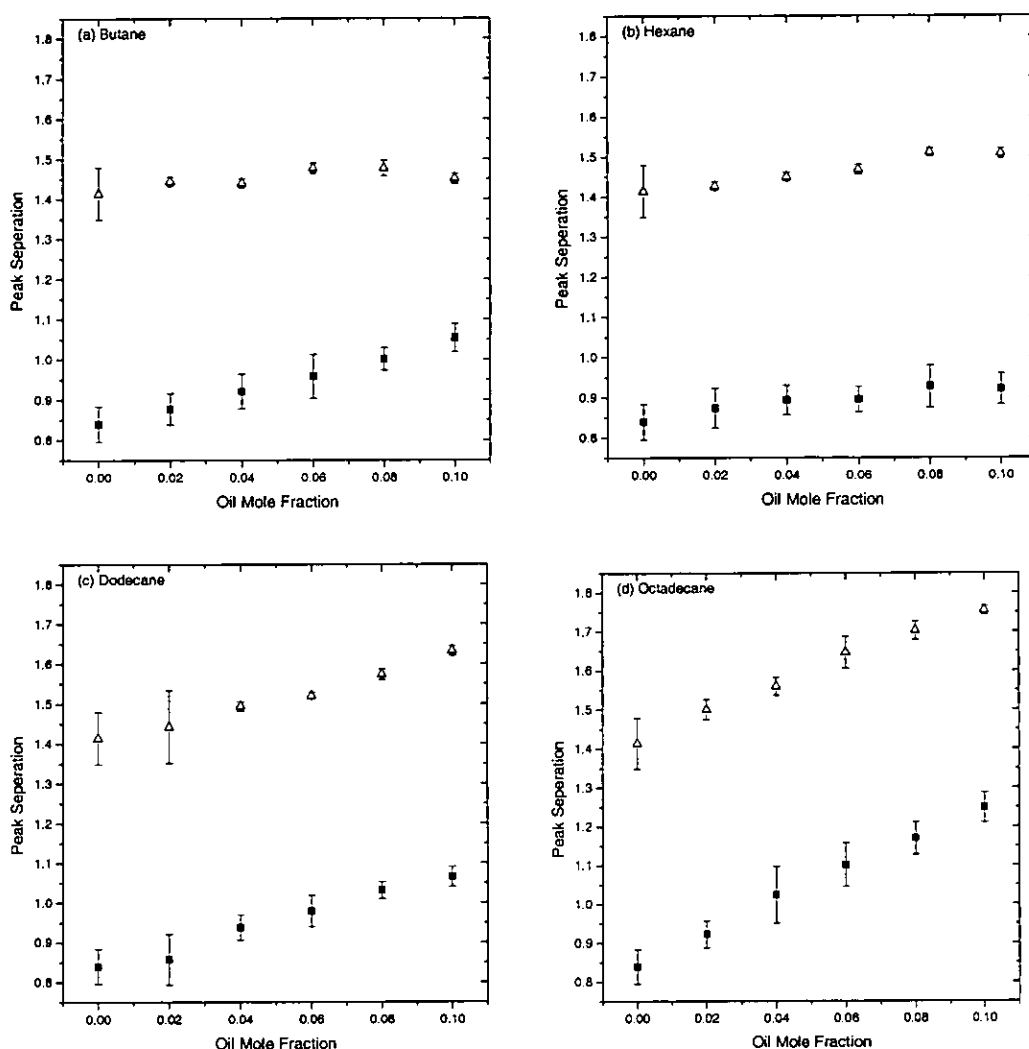


Figure 4.23 Peak Separation for beads 3 and 4 for (a) butane, (b) hexane, (c) dodecane and (d) octadecane. Filled squares = bead 3 and open triangles = bead 4.

Figure 4.22 shows that on increasing concentration beads 1 and 2 remain nearly constant for butane and hexane, but increase for dodecane and octadecane. This indicates that butane and hexane are not aggregating in the centre of the tail region, causing it to expand, while dodecane and octadecane must be aggregating in the centre of the tail region, causing the FWHM to increase for beads 1 and 2. This is further proof of the penetrating behaviour for shorter oils and swelling behaviour for longer oils.

However, it is noted that the FWHM for bead 1 is higher than that for bead 2 at low oil concentrations. This is counter-intuitive as the separation for bead 2 should be higher, leading to a wider peak. This is likely to be caused by the beads at the centre of the tail region to be packed such that the FWHM for bead 1 is higher than for bead 2. Two possible configurations are shown in Figure 4.24. The first configuration is

where the angle between beads 3, 2 and 1 is lower than 90 degrees, so that bead 2 effectively becomes the bead closest to the centre. Another configuration is that the tails overlap with each other sufficiently so that bead 1 on one tail is beyond bead 2 on a tail of the opposite side of the tail region. This is known as interdigitation of the tails.

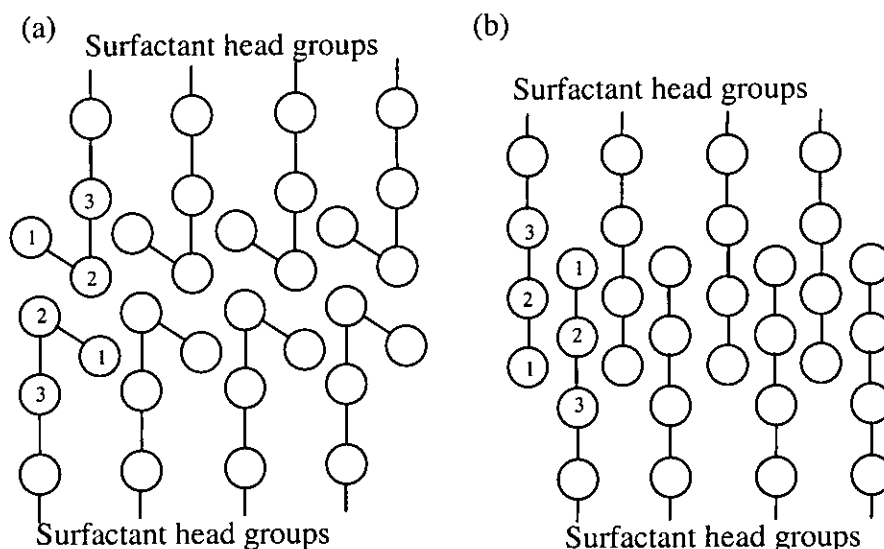


Figure 4.24 Two possibilities leading to wider peak for bead 1 than bead 2 in probability density function. (a) Angle between beads 3, 2 and 1 is less than 90° . (b) Interdigitation of tails.

On increasing concentration, the FWHM for beads 1 and 2 swap over for all oils except hexane. This indicates that the swelling oils, residing in the centre of the interlayer, may reduce this interdigitation effect.

Figure 4.23 shows the separation between beads 3 and 4 on increasing the oil concentration. For butane and hexane, there is little or no increase in separation on increasing oil concentration, but there is an increase for dodecane and octadecane. For bead 4, the separation increases from 1.42nm (no oil) to 1.44nm ($\phi_{but}=0.1$), to 1.50nm ($\phi_{hex}=0.1$), to 1.62nm ($\phi_{dod}=0.10$) and 1.77nm ($\phi_{oct}=0.10$). This further shows the swelling effect for long oils, and that there is more swelling behaviour for octadecane than for dodecane.

4.6 Comparison with Experimental Results

Having shown the results of the addition of different types of oil to the binary phase sequence, these results can now be compared to previous experimental work on the addition of oil to surfactant-water mixtures [2]. In the experimental work, hexane, decane and octadecane were added to the non-ionic surfactant $C_{16}E_6$, which is very similar to the surfactant being modelled, $C_{12}E_6$. The oils are also equivalent except for

decane (experiment) and dodecane (simulation), but are quite close, and are both of similar length to the tail length of the surfactants they are added to. Hexene and hexane are equivalent in this case as the simulation of hexane uses just two beads separated by a single, straight bond. This means that the simulated hexane model is rigid, so it therefore behaves more like hexene. However, as the model does not consider the bond angles or torsion angles of the alkyl chains, it was considered more appropriate to label the molecules in their most simple form, so hexane is used to describe the molecules comprising of two beads, equivalent to six hydrocarbons. Firstly, in order to qualify the comparison, a discussion on the equivalence of the temperature variable in the experimental work with the concentration variable in the modelling work needs to be made. Then the main findings of the experimental work will be highlighted, before a comparison of the results of the different types of oil in the simulation work before finally comparing and contrasting the results of experiment and simulation.

4.7 Temperature and Concentration Equivalence

In all oil addition work, in both experiment and simulation, the effects of the addition of oil are compared to the equivalent binary phase sequence. The present simulation work will be compared to the work on adding oil to $C_{16}E_6$, so the binary phase diagram of $C_{16}E_6$ needs to be considered. This differs upon heating and cooling so both phase diagrams, upon heating and cooling (Figure 1.19) need to be considered. For the experimental work, the phase sequence upon cooling from 45-28°C at 55% by weight $C_{16}E_6$ was used. (Phases were determined with the addition of oil upon cooling.) This phase sequence is L_α , $Mh_1(0)$, $Mh_1(R\bar{3}m)$, $Mh_1(R\bar{3}m)+V_1$ and V_1 . This phase sequence is exactly the same at 30°C, decreasing concentration from 62-52%.

So as the phase sequences change little whether concentration or temperature is being varied, it was most convenient to vary temperature as this meant fewer samples were made, and this in turn decreases error. However, it already has been shown that in the model developed using DPD, the temperature of the system has little effect on the phases. However, the binary phase sequence established from the developed model on increasing concentration is equivalent to the binary phase sequence in experiment both in varying concentration and temperature. One can therefore make the equivalence

that the concentration parameter in the simulation is effectively the same as the temperature parameter for experiment.

4.8 Experimental Findings

According to experimental work ^[2], the addition of oils to a surfactant and water mixture destabilised phases with surface curvature, and the longer the oil, the more pronounced the effect (figure 1.21). The simulation results also exhibit this for hexane and dodecane, where the phase transitions occur at lower mole fractions of dodecane than for hexane. However, the simulation results from octadecane show that phases with curvature remain stable at *higher* mole fractions of hexane instead of lower as expected from experimental work.

Hexene is the most penetrating oil and is situated between the surfactant chains causing the surface area per molecule to increase, but the bilayer spacing remains constant. For octadecane, the surface area per head group remained constant, while the bilayer spacing increased. (See Figure 4.25 and Figure 4.26 for d_0 values for hexane and octadecane respectively and Figure 4.27 shows S_a values for all three oils added.) Irrespective of the type of oil added, there was a loss of phases in favour of the lamellar phase at sufficiently high concentration, and ultimately phase separation. The $Mh_1(R\bar{3}m)$ phase was destabilised at low concentrations and this was thought to be due to the fact that the interlayer interaction is destabilised by the swelling of the alkyl chain region and the changing water layer thickness. The $Mh_1(0)$ phase has a wider range than the $Mh_1(R\bar{3}m)$ phase but smaller than the L_α phase, showing that the oils are affecting the rigidity of the interface, discouraging the formation of curved interfaces and water-filled defects. The L_α phase, which has no interfacial curvature, is only destabilised by phase separation.

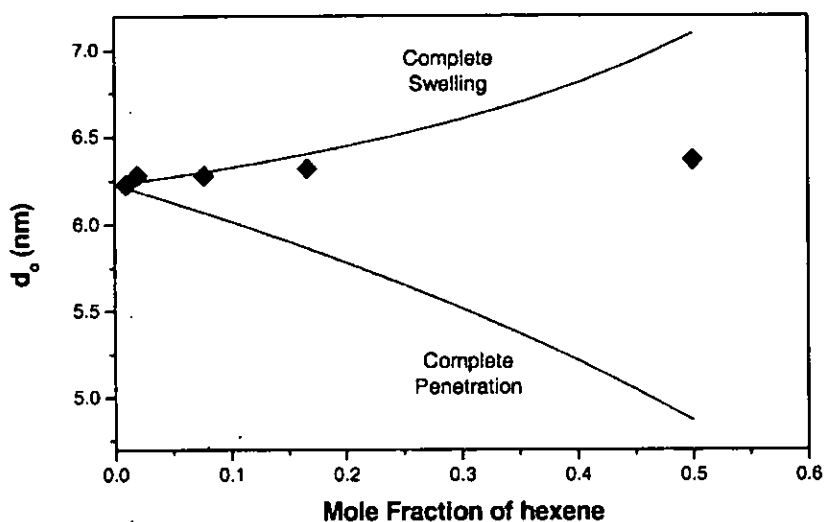


Figure 4.25 Lamellar spacing as a function of hexane mole fraction. Taken from [1,2].

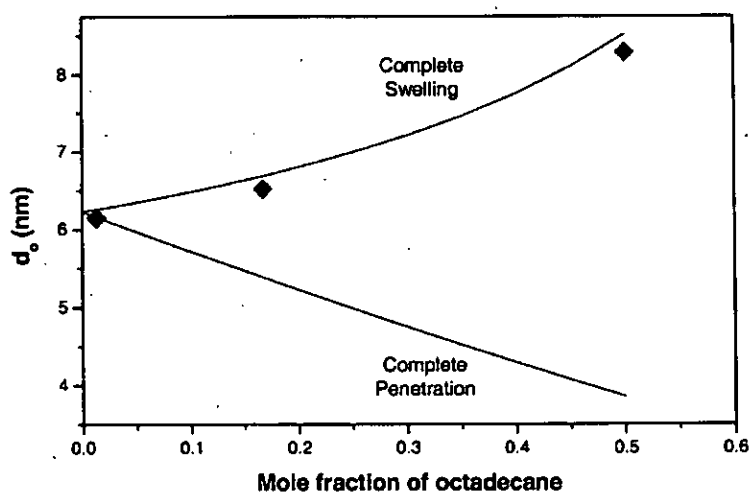


Figure 4.26 Lamellar spacing as a function of octadecane mole fraction. Taken from [1,2].

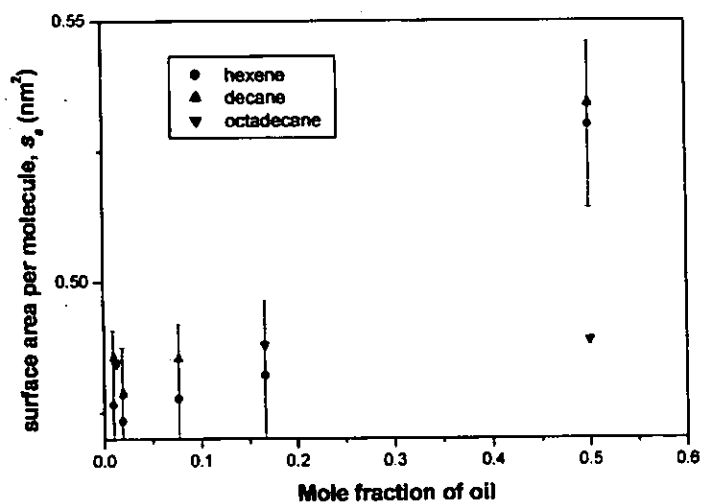


Figure 4.27 Surface area per molecule as a function of mole fraction of oil. Taken from [1,2].

5 Modelling Anaesthetics & Alcohols

5.1 Introduction

Anaesthetics are small molecules with amphiphilic properties. The addition of these molecules to surfactant and water mixtures should therefore result in the anaesthetics residing in the interfacial region. In this chapter a model anaesthetic has been created and added to the binary phases of $C_{12}E_6$ to investigate the effect of the addition of anaesthetic molecules to the interfacial curvature. This anaesthetic has then been modified by changing the interaction parameters. These results can then be compared to experiment.

5.2 Modelling Anaesthetics

As anaesthetic molecules are amphiphilic, the anaesthetic model will comprise a hydrophobic part and a hydrophilic part, like the surfactant model. The numbers of beads for these parts should also equate to the volume of the anaesthetic molecule (as in section 2.7.1). The shape and hydrophilicity of components of different anaesthetics changes so it is not easy to accurately model an anaesthetic in the same way as it was to model a single chain non-ionic surfactant. The first, most primitive model that was used was a rudimentary, generic amphiphilic molecule comprising one head bead and one tail bead connected together with a bond of the same type as the surfactant model bond. Figure 5.1 shows a schematic of the model anaesthetic.



Figure 5.1 Schematic showing generic anaesthetic molecule with one hydrophobic bead (red) and one hydrophilic bead (blue) connected with a bond.

5.3 Results

A phase diagram showing the phase structure upon addition of the anaesthetic to differing surfactant and water concentrations is shown in Figure 5.2. This shows that at $X_{sw}=0.36$ and 0.75 , L_α is stable until the mole fraction of anaesthetic (φ_{an}) = 0.08 and 0.10 respectively. At these concentrations, the mesh phase becomes stable. At $X_{sw} = 0.23$, the mesh phase is stable until 0.14 , when dV_1 becomes stable. At $X_{sw} = 0.16$, L_3 is stable until $\varphi_{an} = 0.02$ and dV_1 becomes stable at $\varphi_{an} = 0.08$. Overall, it is clear

that adding anaesthetic destabilises phases with lower interfacial curvature in favour of phases with higher interfacial curvature. Figure 5.3 shows isodensity images of phase evolution on the addition of anaesthetic.

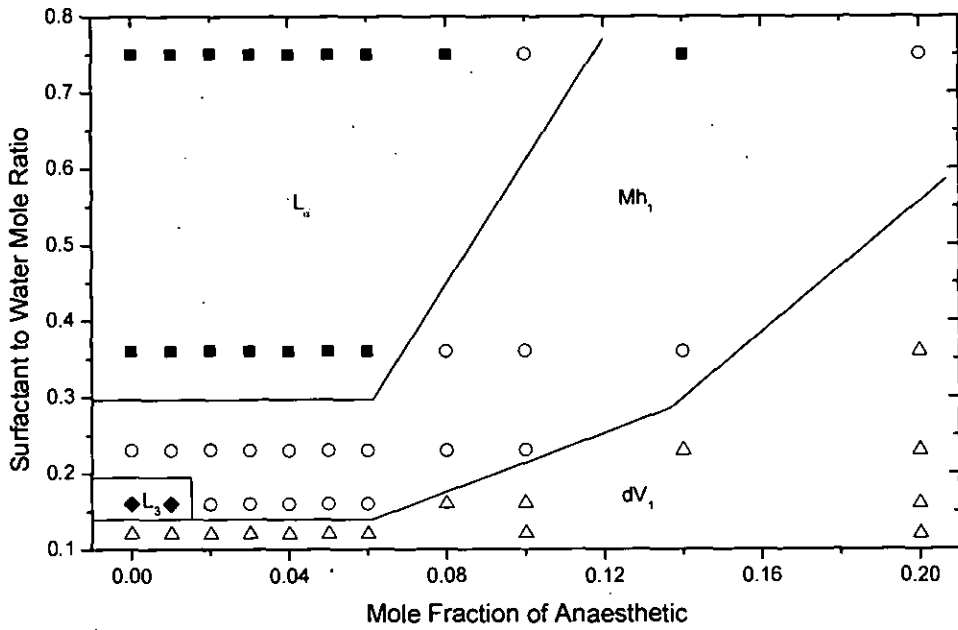


Figure 5.2 Phase diagram showing phases on increasing mole fraction of anaesthetic (14.5nm box) Filled squares = L_ω , open circles = Mh_1 , filled diamonds = L_3 and open triangles = dV_1 . Lines are a guide to the eye.



Figure 5.3 Isodensity images showing phase structures on the addition of anaesthetic at $X_{sw} = 0.16$

5.3.1 d_0 and S_a

d_0 and S_a values were calculated as in chapter 4, and graphs showing the lamellar repeat distance and the effective surface area per surfactant head group are shown in Figure 5.4 and Figure 5.5 respectively, compared to ideal penetrating and swelling behaviour. These graphs show that d_0 decreases as the concentration of anaesthetic increases, and S_a increases as the concentration of anaesthetic increases. The anaesthetic shows behaviour intermediate between ideal swelling and penetrating behaviour, and the form of these plots for the anaesthetic is very similar to that of hexane.

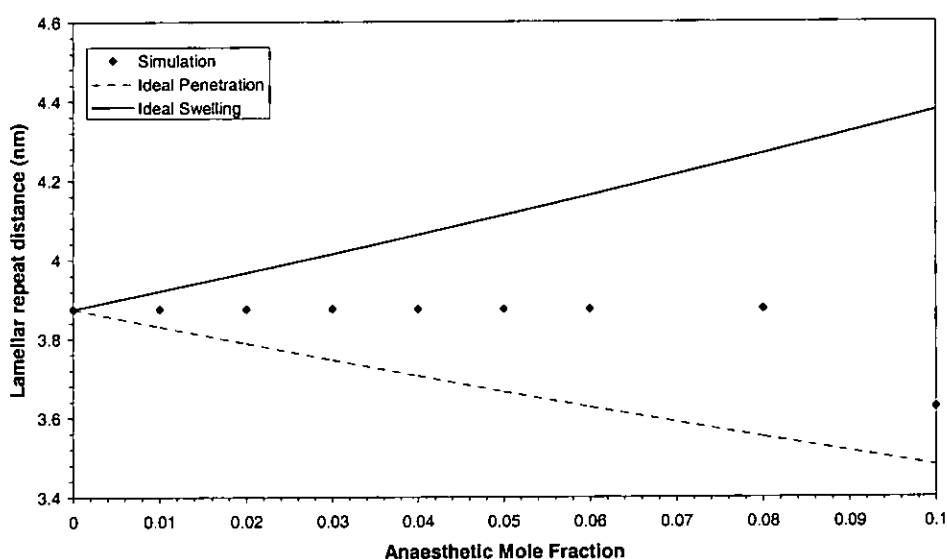


Figure 5.4 d_0 spacing as a function of anaesthetic mole fraction.

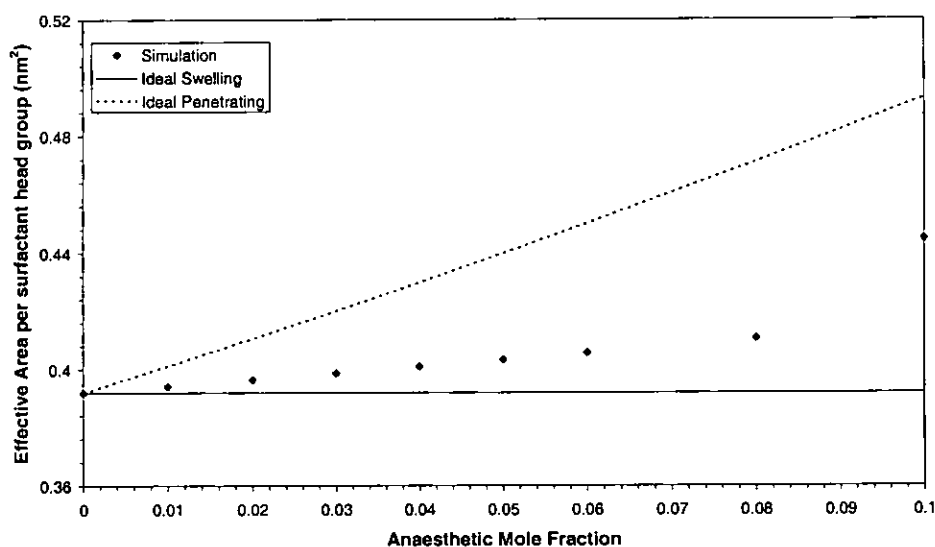


Figure 5.5 S_a as a function of anaesthetic mole fraction.

5.3.2 Probability Density Functions of Lamellar Phases

Probability density functions were produced across the lamellar phase at $X_{sw}=0.75$ and are shown in Figure 5.6. Figure 5.7 shows a composite of the probability distribution functions for the anaesthetic beads. The peaks of these distributions correspond with the interfacial region, showing that the anaesthetic molecules reside in the interfacial region as expected, because of their amphiphilic nature.

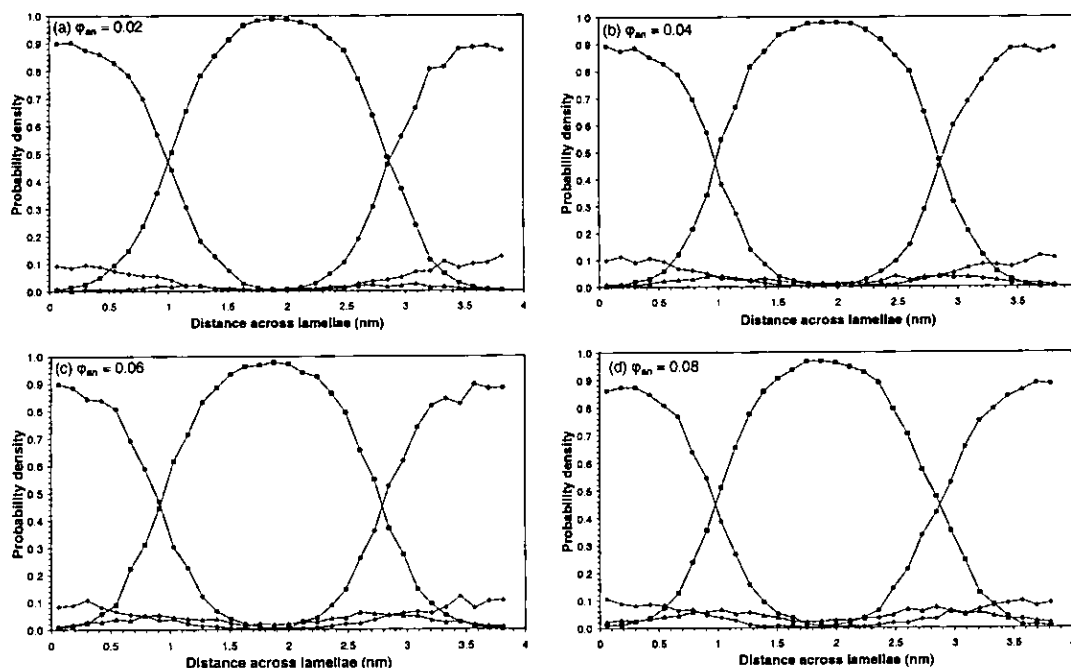


Figure 5.6 Probability density function of lamellar phase for $\varphi_{an} = 0.02$ (a), 0.04 (b), 0.06 (c) and 0.08 (d). Filled squares = tail, open circles = head, filled diamonds = water and open triangles = anaesthetic.

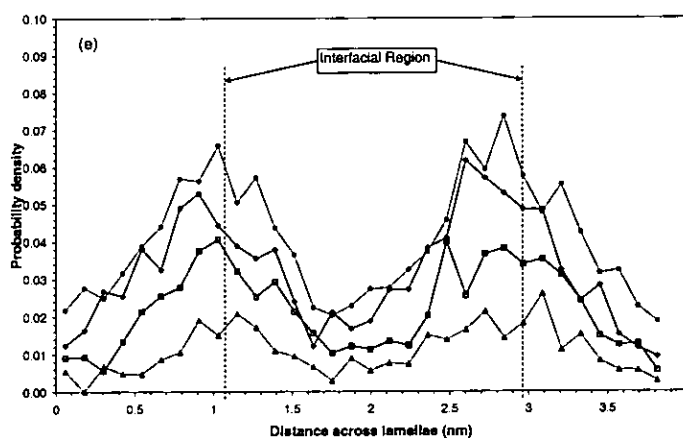


Figure 5.7 Composite probability density functions of lamellar phase for anaesthetic beads for $\varphi_{an} = 0.02$ (Filled triangles), 0.04 (open squares), 0.06 (filled diamonds) and 0.08 (open circles).

5.4 Modifying the Anaesthetic Parameters

The model anaesthetic, although generic in nature, has produced some useful results. However, the parameters of the model can be adapted in an attempt to improve the model, and investigate whether such changes will allow productive comparison to be made with experiment.

5.4.1 Modifying Anaesthetic Tail-Surfactant Tail Interaction Strength

One difference between the modelled anaesthetic and the anaesthetics used in experiment is that the anaesthetic tails are in general lipophobic^[1]. This means that the anaesthetic tails experience repulsive forces from hydrocarbon chains. To account for this behaviour, the repulsion parameter between the anaesthetic tail bead and the surfactant tail beads can be increased, mimicking this lipophobicity. Two more model anaesthetics have been used, identical to the first but with anaesthetic tail-surfactant tail interaction parameters of $a_{TsTa}=30$ and 35 (instead of $a_{TsTa}=25$ for the generic anaesthetic). The phase diagrams on increasing concentration of anaesthetic for anaesthetics with $a_{TsTa}=25, 30$ and 35 (showing the effect of the lipophobicity of the anaesthetic tail) at surfactant to water mole ratios of 0.16 to 0.36 are shown in Figure 5.8. The mole fraction of anaesthetic for each of these phase transitions is tabulated in Table 5.1 for anaesthetics with $a_{TsTa}=25, 30$ and 35 .

The effect of increasing the lipophobicity of the anaesthetic tail ($a_{TsTa}=30$ and 35) decreases phase transition concentrations, by considering that the $X_{sw}=0.23$ $Mh_1 - dV_1$ and $X_{sw}=0.36$ $L_\alpha - Mh_1$ phase transition concentration decrease as lipophobicity is introduced. This implies that increasing the lipophobicity of the anaesthetic tail increases the surface curvature of the phases.

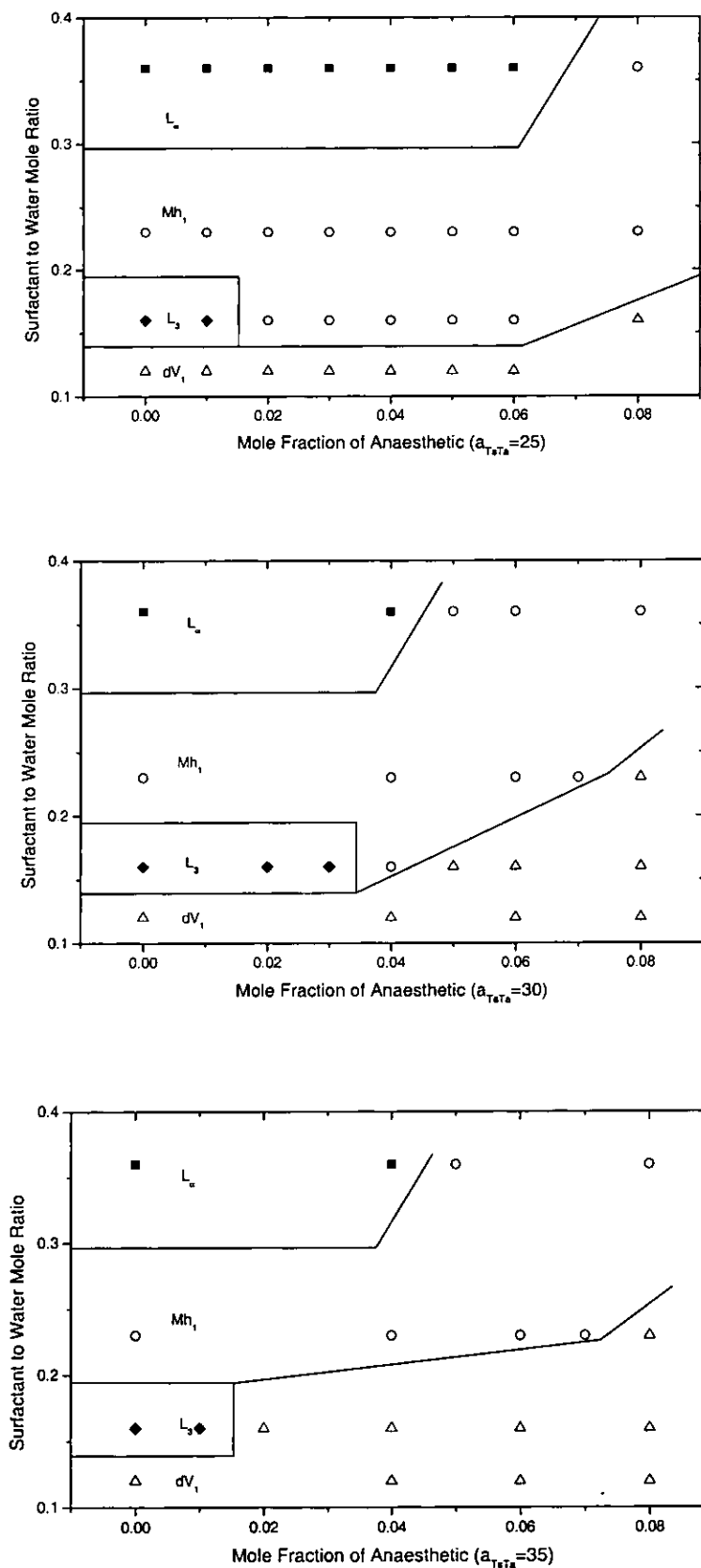


Figure 5.8 Phase diagram showing phases on increasing mole fraction of anaesthetics with $a_{T_a} = 25$, 30 and 35 (14.5nm box). Filled squares = L_α , open circles = Mh_1 , filled diamonds = L_3 and open triangles = dV_1 . Lines are a guide to the eye.

Surfactant tail - Anaesthetic tail repulsion parameter	$X_{sw}=0.16$ $L_3 - Mh_1$	$X_{sw}=0.16$ $Mh_1 - dV_1$	$X_{sw}=0.23$ $Mh_1 - dV_1$	$X_{sw}=0.36$ $L_\alpha - Mh_1$
25	0.015	0.065	0.115	0.075
30	0.035	0.045	0.075	0.045
35	0.015*	-	0.075	0.045

* $X_{sw}=0.16$, $L_3 - dV_1$ transition

Table 5.1 Phase transition concentrations on changing surfactant tail-anaesthetic tail repulsion parameter

5.4.2 Modifying Anaesthetic Head-Water Interaction Strength

According to [2], type I anaesthetics have polar moieties which displace water from between the ethylene oxide head groups, promoting their dehydration, inducing decreased surface curvature. This behaviour can be replicated in the model by increasing the repulsion parameter between the anaesthetic head group and water (a_{HaW}). This interaction parameter has been raised from $a_{HaW}=25$ to 30 and 35. Also from [2], type II anaesthetics carry a localised charge in their molecules. The association of the charged part of the molecule with the base of the head group region may affect interfacial curvature. This effect can be mimicked by decreasing a_{HaW} . This interaction parameter has been lowered from $a_{HaW}=25$ to 20 and 15.

The phase diagrams for anaesthetics with $a_{HaW}=15, 20, 25, 30$ and 35 (showing the effect of the repulsion of the anaesthetic head with water) also at surfactant to water mole ratios of 0.16 to 0.36 are shown in Figure 5.9. It can be seen that the form of these phase diagrams are the same as for the generic anaesthetic ($a_{HaW}=25$). However the phase transitions occur at different anaesthetic concentrations, so the different types of anaesthetics can be compared by investigating the following four phase transitions: L_3 to Mh_1 at $X_{sw}=0.16$; Mh_1 to dV_1 at $X_{sw}=0.16$; Mh_1 to dV_1 at $X_{sw}=0.23$; L_α to Mh_1 at $X_{sw}=0.36$. The mole fraction of anaesthetic for each of these phase transitions is tabulated in Table 5.2 for anaesthetics with $a_{HaW}=15, 20, 25, 30$ and 35.

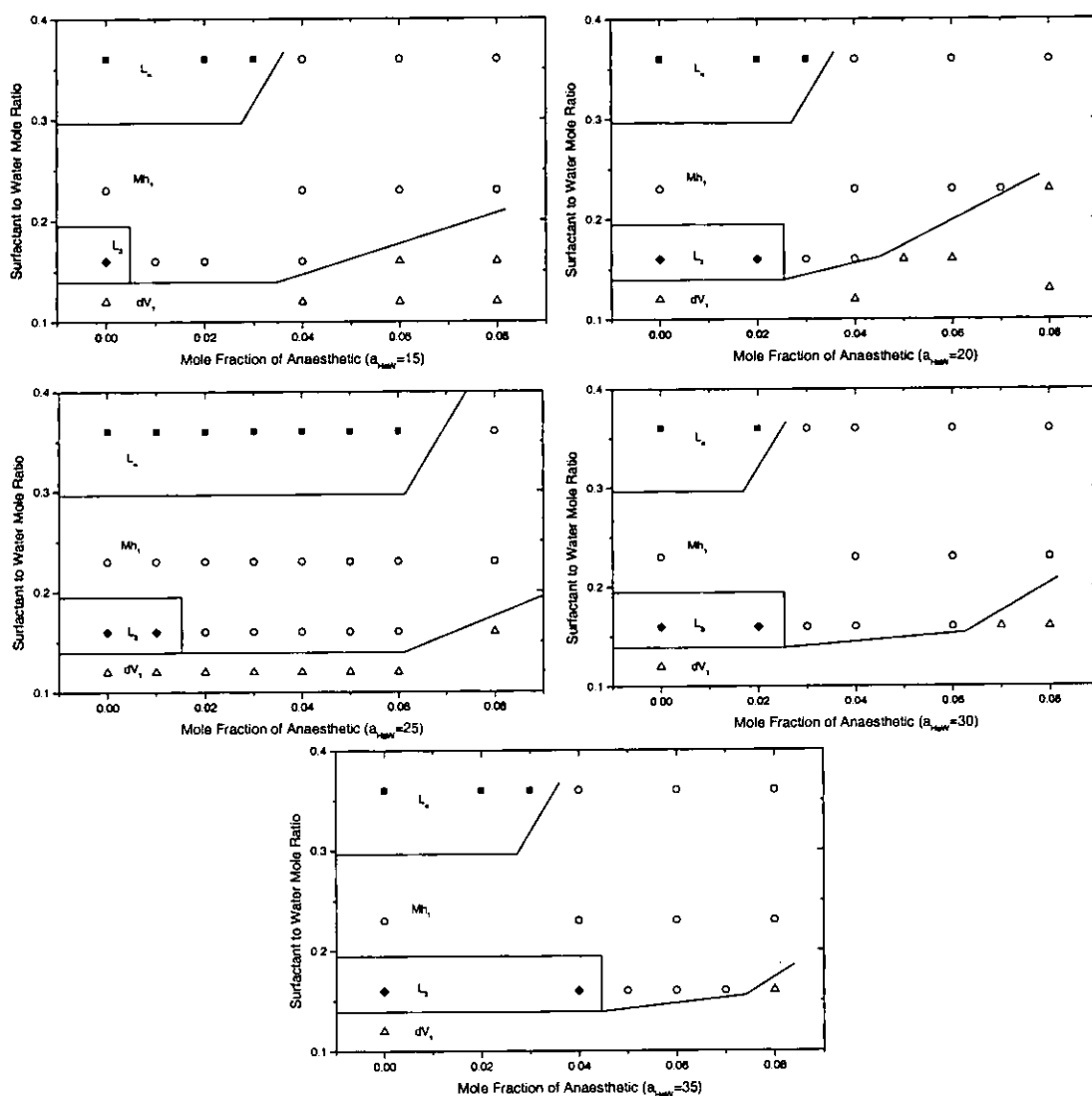


Figure 5.9 Phase diagram showing phases on increasing mole fraction of anaesthetics with $a_{HaW}=15, 20, 25, 30$ and 35 (14.5nm box). Filled squares = L_α open circles = Mh_1 , filled diamonds = L_3 and open triangles = dV_1 . Solid lines are a guide to the eye.

Anaesthetic head - water repulsion parameter	$X_{sw}=0.16$	$X_{sw}=0.16$	$X_{sw}=0.23$	$X_{sw}=0.36$
	$L_3 - Mh_1$	$Mh_1 - dV_1$	$Mh_1 - dV_1$	$L_\alpha - Mh_1$
15	0.005	0.045	0.095	0.035
20	0.025	0.045	0.075	0.035
25	0.015	0.065	0.115	0.075
30	0.025	0.065	0.095	0.025
35	0.045	0.075	0.105	0.035

Table 5.2 Phase transition concentrations on changing anaesthetic head-water repulsion parameter

The effects of changing the anaesthetic head-water repulsion parameter were investigated further by plotting the concentrations for each phase transition for anaesthetics with $a_{HaW}=15, 20, 25, 30$ and 35 . Plots are shown in Figure 5.10 and Figure 5.11 for the L_3 to Mh_1 and Mh_1 to dV_1 at $X_{sw}=0.16$ phase transitions respectively, and Figure 5.12 and Figure 5.13 for the Mh_1 to dV_1 at $X_{sw}=0.23$ and L_α to Mh_1 at $X_{sw}=0.36$ phase transitions respectively. These figures show that for the $X_{sw}=0.23$ $Mh_1 - dV_1$ and the $X_{sw}=0.36$ $L_\alpha - Mh_1$ phase transitions there is no discernible trend on changing the interaction parameter. The L_α to Mh_1 transition may have a peak at $a_{HaW}=25$, and decrease for parameters stronger or weaker than this, but as there is insufficient data, this is just conjecture. However for the L_3 to Mh_1 and Mh_1 to dV_1 phase transitions, both at a lower surfactant concentration of $X_{sw}=0.16$, there is a noticeable trend, where increasing the repulsion parameter increases the concentration for the phase transition.

These results indicate that at high surfactant concentration, there is no discernible relationship between a_{HaW} and the concentration of phase transition, while at lower surfactant concentration ($X_{sw}=0.16$), there is a relationship. The repulsion parameter a_{HaW} therefore has an increased effect at lower surfactant concentrations where there is more water for the anaesthetics to repel from the interface. The stronger this repulsion is, the more water is repelled from the interface, decreasing the interfacial curvature, delaying the formation of phases with higher surface curvature, i.e. increasing the anaesthetic concentration required for the phase transitions to phases with higher surface curvature.

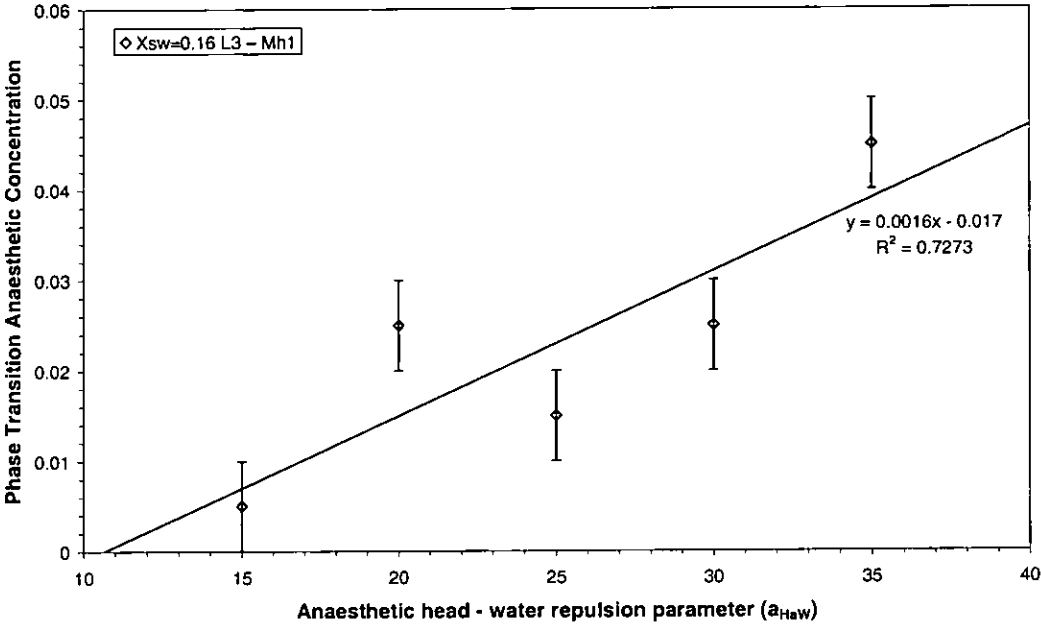


Figure 5.10 Phase transition concentration for the addition of anaesthetic for the $L_3 - Mh_1$ transition at $X_{sw}=0.16$.

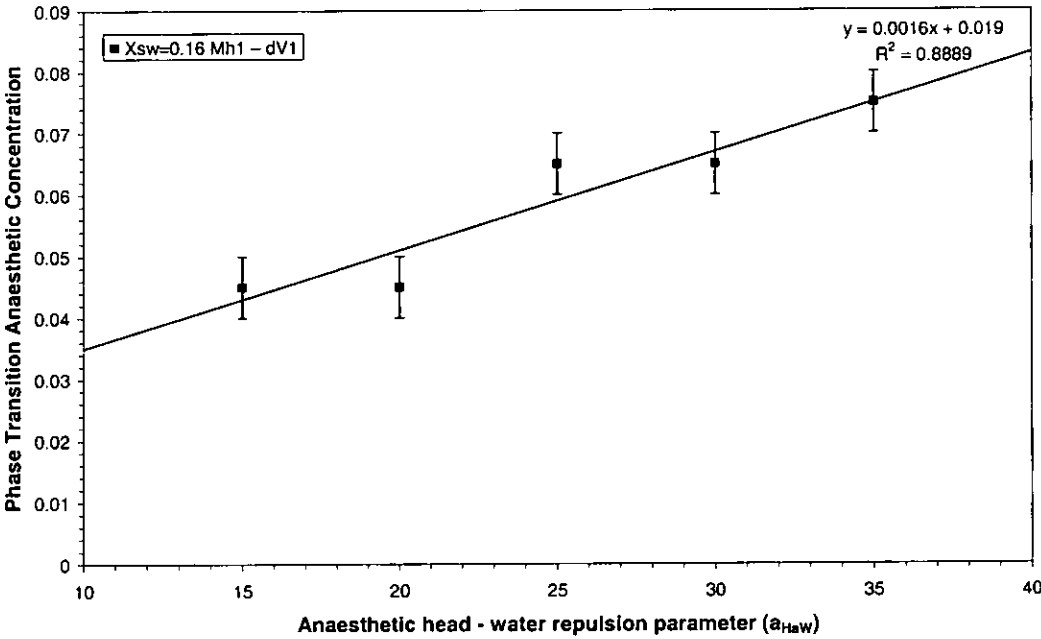


Figure 5.11 Phase transition concentration for the addition of anaesthetic for the $Mh_1 - dV_1$ transition at $X_{sw}=0.16$.

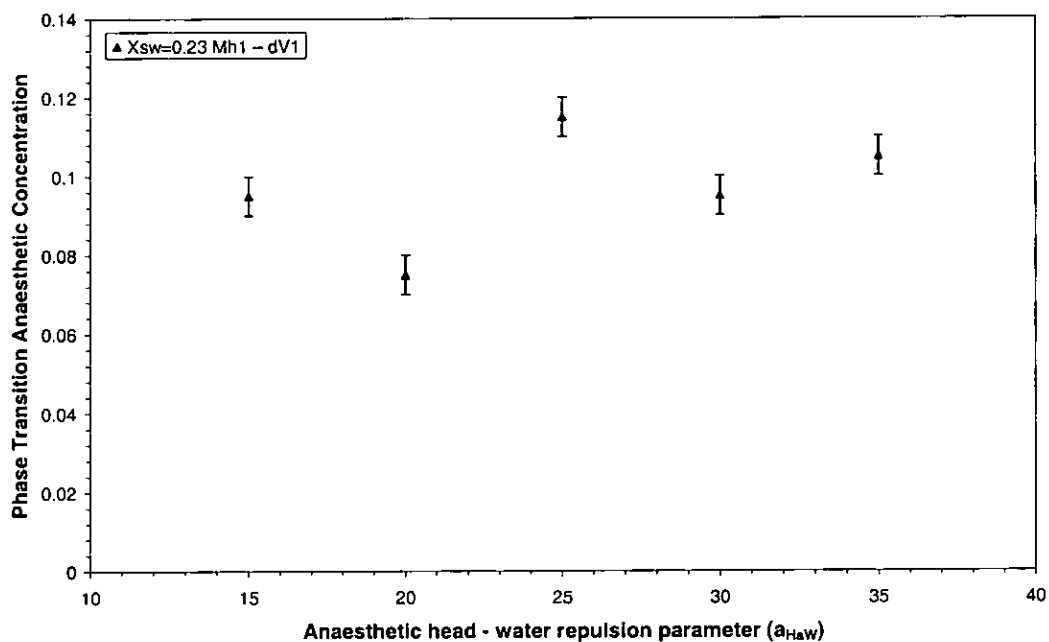


Figure 5.12 Phase transition concentration for the addition of anaesthetic for the $Mh_1 - dV_1$ transition at $X_{sw}=0.23$.

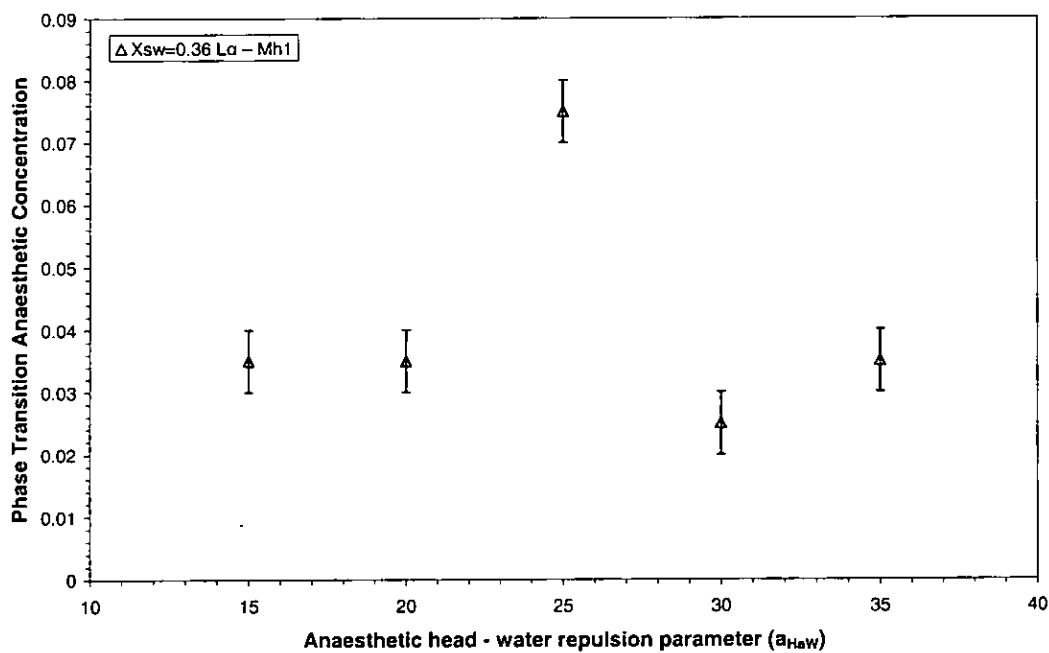


Figure 5.13 Phase transition concentration for the addition of anaesthetic for the $L_a - Mh_1$ transition at $X_{sw}=0.36$.

5.5 Comparison to Experiment

The addition of several types of anaesthetic molecules to surfactant-water mixtures has been performed in experiments^[2]. The results of these experiments show that two types of behaviour are observed upon adding anaesthetics to surfactant water mixtures, known as type I and type II. Type I anaesthetics have a polar moiety and decreased the surface curvature of phases, destabilizing phases such as the cubic and mesh phase in favour of the lamellar phase. However type II anaesthetics carry a localized charge and increased the surface curvature of the mixtures, inducing mesh and cubic phases. At a physiological pH however, both types of anaesthetics decreased the surface curvature of the phases.

The simulation results show that the addition of a generic anaesthetic molecule increases the interfacial curvature, so therefore this simulated anaesthetic behaves as a type II anaesthetic.

Modifying this molecule so that its tail is lipophobic (by increasing the interaction parameter between the tail of the anaesthetic and the tail of the surfactant to $a_{TaTs}=30$ and 35) increases the anaesthetic's ability to induce higher surface curvature, enhancing type II behaviour.

Experimentally, Type II anaesthetics carry a localised charge in their molecules. The association of the charged part of the molecule with the base of the head group region may affect interfacial curvature. This effect was mimicked by reducing a_{HaW} (the repulsion parameter between the anaesthetic head and water) from 25 to 20 and 15. Anaesthetics with $a_{HaW}=20$ and 25 also had a greater ability to induce higher surface curvature, showing that this enhances type II behaviour.

Type I anaesthetics have polar moieties which displace water from between the ethylene oxide head groups, promoting their dehydration, inducing decreased surface curvature. This behaviour was replicated in the model by increasing the repulsion parameter between the anaesthetic head group and water (a_{HaW}) from 25 to 30 and 35. These anaesthetics still overall served to increase the surface curvature of the phases, enhancing type II behaviour. However, at $X_{sw}=0.16$ (lower surfactant concentration), where there was more water for the anaesthetic to repel, the effect of these anaesthetics was to decrease the ability to induce higher surface curvatures, diminishing type II behaviour.

Overall, all of the anaesthetics modelled represent type II anaesthetics, even for anaesthetics with $a_{HaW} = 30$ and 35, which were adapted in an attempt to induce type I behaviour. Table 5.3 summarises the results of adding anaesthetics to bulk surfactant-water systems in experiment and simulation for ease of comparison.

Experiments were also attempted at pH 7.5, where type II anaesthetics displayed type I behaviour as well. To model this pH difference in a simulation, the charges of the anaesthetics with their associated counter ions would need to be modelled, and such a study lies outside the scope of this research.

In comparison to the addition of oil, the addition of anaesthetics acts quite differently, increasing interfacial curvature instead of decreasing it. Therefore, the behaviour of these mixtures behaves differently depending on the nature of the small molecule being added.

		Type I	Type II
Experiment	Examples	Halothane Sodium Thiopental Lidocaine base form	Lidocaine Hydrochloride Prilocaine Hydrochloride Ketamine Hydrochloride
	No Buffer	Decrease Curvature	Increase Curvature
	pH7.5 Buffer	Decrease Curvature	Decrease Curvature
	Distinguishing property	Have Polar Moiety	Carry localised charge
	How it may affect curvature	Displaces water from head groups, decreasing curvature	Association of charged part with base of head group may affect curvature
Simulation	Generic Anaesthetic	Behaves as type II	
	Anaesthetic head – water repulsion parameter	Increase ($a_{HaW}=30, 35$)	Decrease ($a_{HaW}=20, 15$)
	Effect	No real change, behaves as type II. However at low surfactant concentration it behaves less like type II, as more water present for anaesthetic to repel	No real change. Still behaves as type II

Table 5.3 Summary of the results of adding anaesthetics to bulk surfactant-water systems in experiment and simulation for ease of comparison.

5.6 Alcohol

The addition of amphiphilic molecules to the surfactant-water system with tails of increasing lengths was modelled. These alcohol-like molecules consisted of one head bead like the anaesthetics and multiple tail beads, making the molecule have a bulkier chain region. Three alcohols were simulated, with 2, 3 and 4 tail beads, labelled as A_2B , A_3B and A_4B . The parameters were the same as for the generic anaesthetic. The phase diagram on increasing A_2B concentration to surfactant-water mixtures of different mole ratios is shown in Figure 5.15. Similar figures for A_3B and A_4B appear in Figure 5.16 and Figure 5.17 respectively. Considering the modelled anaesthetic A as a very short alcohol (AB), the phase diagram taken from Figure 5.2 is shown again in Figure 5.14 for comparison.

Figure 5.14 shows that upon the addition of AB, L_3 is destabilised in favour of Mh_1 , and dV_1 remains stable.

Figure 5.15 shows that upon the addition of A_2B , the L_3 and dV_1 phases are destabilised in favour of the Mh_1 phase. The Mh_1 phase is the most widespread phase in the entire diagram, and at mole fractions above 0.05, the Mh_1 even becomes stable over the L_α phase at $X_{sw}=0.36$.

Figure 5.16 Shows that A_3B destabilises the Mesh phase at lower alcohol concentrations, favouring the mesh phase. While there is no change in the sponge phase, the dV_1 phase expands slightly, making the mesh phase smaller than for A_2B . Figure 5.17 shows the same trend, where the mesh phase is destabilised at even lower concentrations of alcohol for A_4B than for A_3B . Again, there is no change in the sponge phase but the dV_1 phase expands slightly, making the mesh phase smaller still than in the A_2B phase diagram. Figure 5.18 shows a composite figure of the alcohol additions. The stability of the mesh phase decreases as the length of the chain of the alcohol increases. It is shown that A_2B phase diagram has the largest mesh region, showing that the mesh phase is most stabilised after the addition of this component. Therefore, the stability of the mesh phase in various ternary systems with amphiphilic additives depends on the length of the chain. The alcohol chain length critically affects the stability of the phases. Figure 5.19 illustrates the different effects of short and long chain alcohols by showing isodensity images of phase evolution of the addition of A_2B and A_4B .

A short chain alcohol (AB and A_2B , Figure 5.20 (left)) will encourage the growth of higher curvature structures, e.g. dV_1 and Mh_1 . As the alkyl chain length increases

(A_3B and A_4B , Figure 5.20 (right)), and with the alcohol anchored at the interface curvature will decrease and the interface will flatten.

Curved interfaces are suppressed even at higher alcohol concentrations and dV_1 retreats as does Mh_1 .

The stabilisation of a phase such as Mh_1 critically depends upon the alcohol chain length; too short and dV_1 dominates (alcohol AB), too long and all high curvature phases are squeezed out (A_3B and A_4B). The optimum chain length for Mh_1 stability for this model is 2 tail beads (A_2B).

These findings are in agreement with experiments ^[3] that show longer chain alcohols behave as oils and shorter chain alcohols act as co-solvents and/or co-surfactants, depending on chain length.

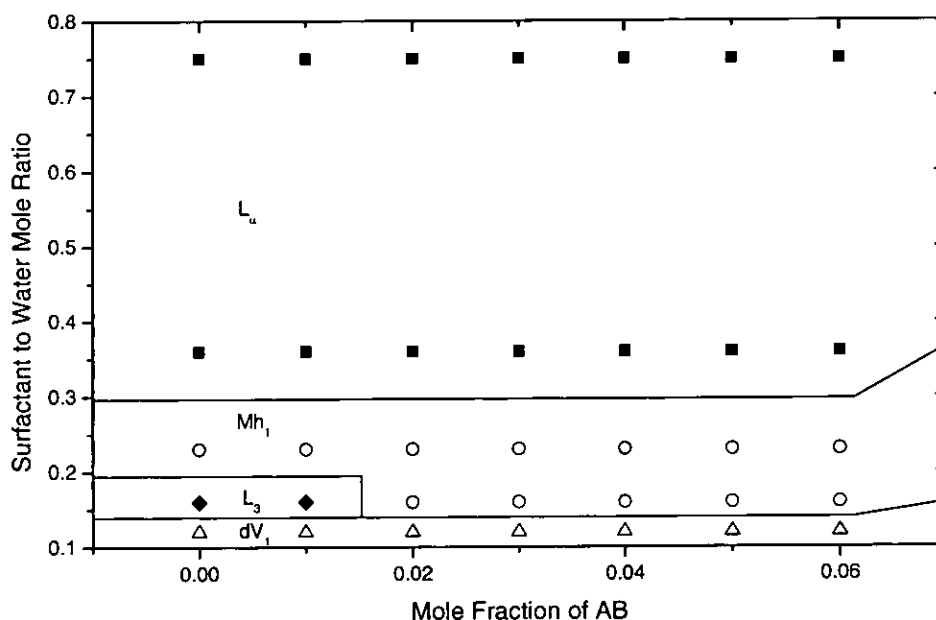


Figure 5.14 Phase diagram showing phases on increasing mole fraction of AB (14.5nm box). Filled squares = L_u , open circles = Mh_1 , filled diamonds = L_3 and open triangles = dV_1 . Solid lines are a guide to the eye.

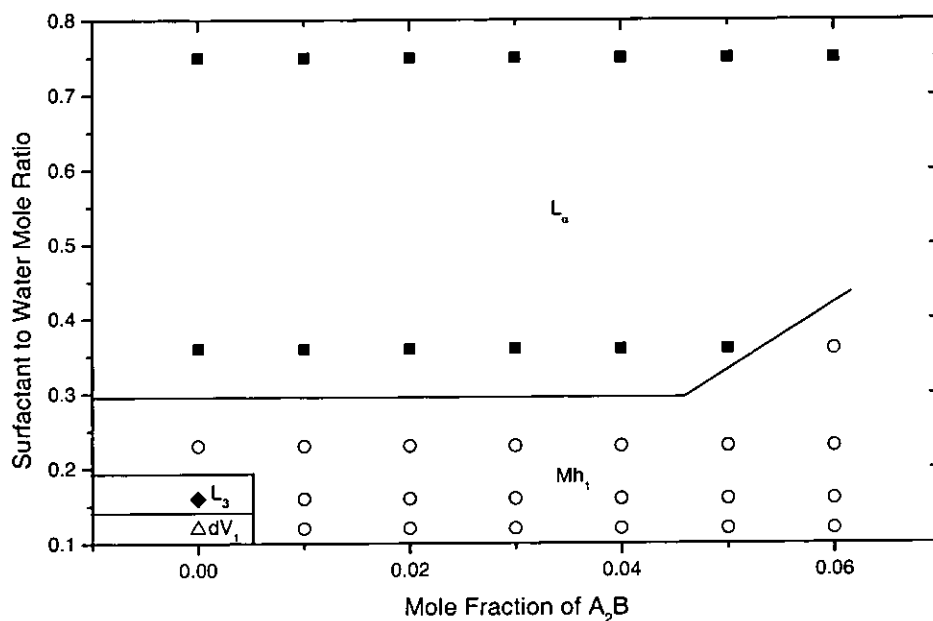


Figure 5.15 Phase diagram showing phases on increasing mole fraction of A_2B (14.5nm box). Filled squares = L_α , open circles = Mh_1 , filled diamonds = L_3 and open triangles = dV_1 . Solid lines are a guide to the eye.

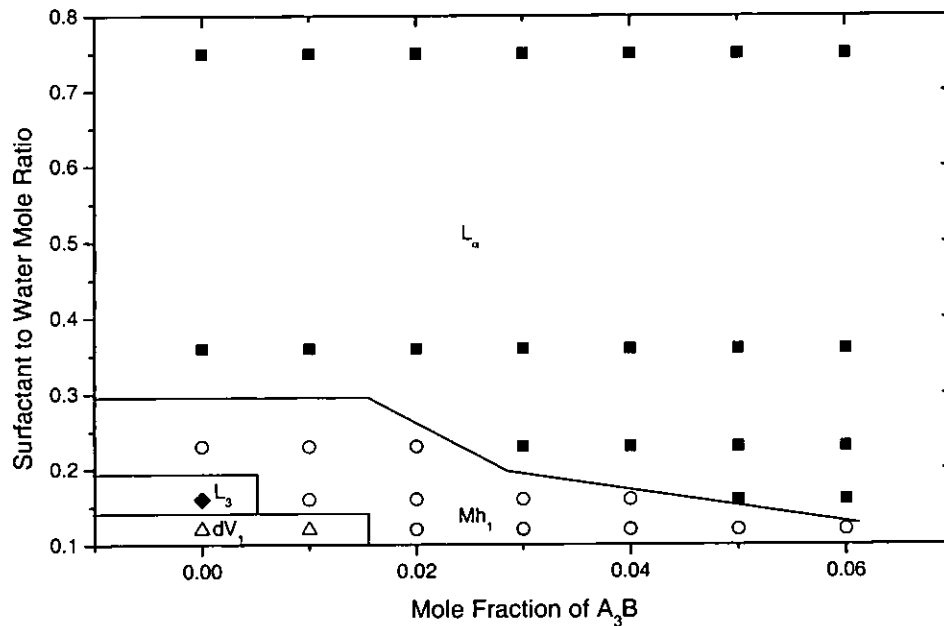


Figure 5.16 Phase diagram showing phases on increasing mole fraction of A_3B (14.5nm box). Filled squares = L_α , open circles = Mh_1 , filled diamonds = L_3 and open triangles = dV_1 . Solid lines are a guide to the eye.

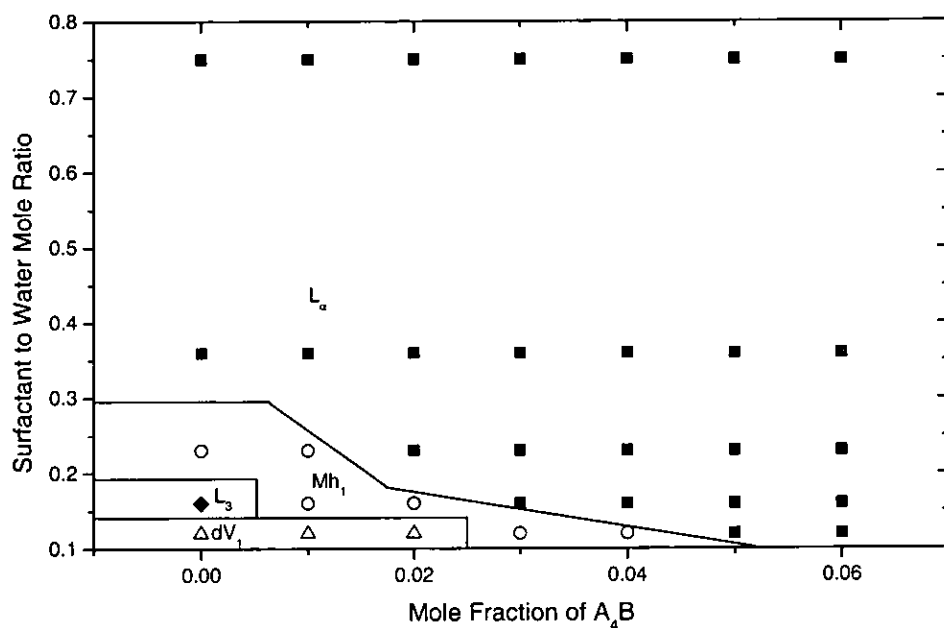


Figure 5.17 Phase diagram showing phases on increasing mole fraction of A₄B (14.5nm box). Filled squares = L_α, open circles = Mh₁, filled diamonds = L₃ and open triangles = dV₁. Solid lines are a guide to the eye.

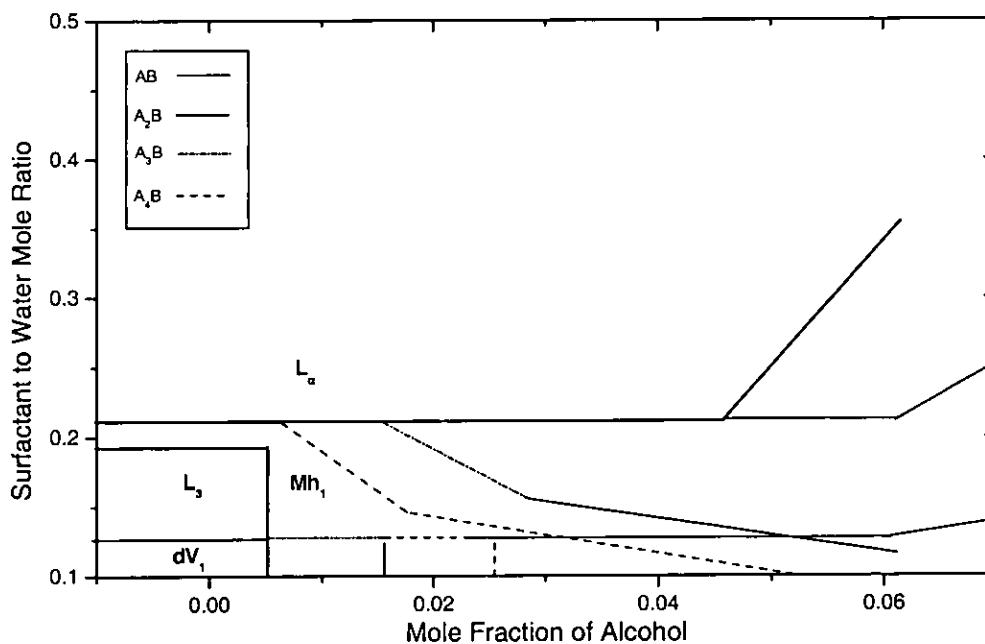


Figure 5.18 Composite Phase diagram showing phases on increasing mole fraction of AB, A₂B, A₃B and A₄B (14.5nm box). Filled squares = L_α, open circles = Mh₁, filled diamonds = L₃ and open triangles = dV₁. Solid lines are a guide to the eye. Phase region for L₃ remains same for all alcohols, and as chain lengthens beyond A₂B phase region for dV₁ extends (boxes) and phase boundary for Mh₁ to L_α transition lowers (lines).

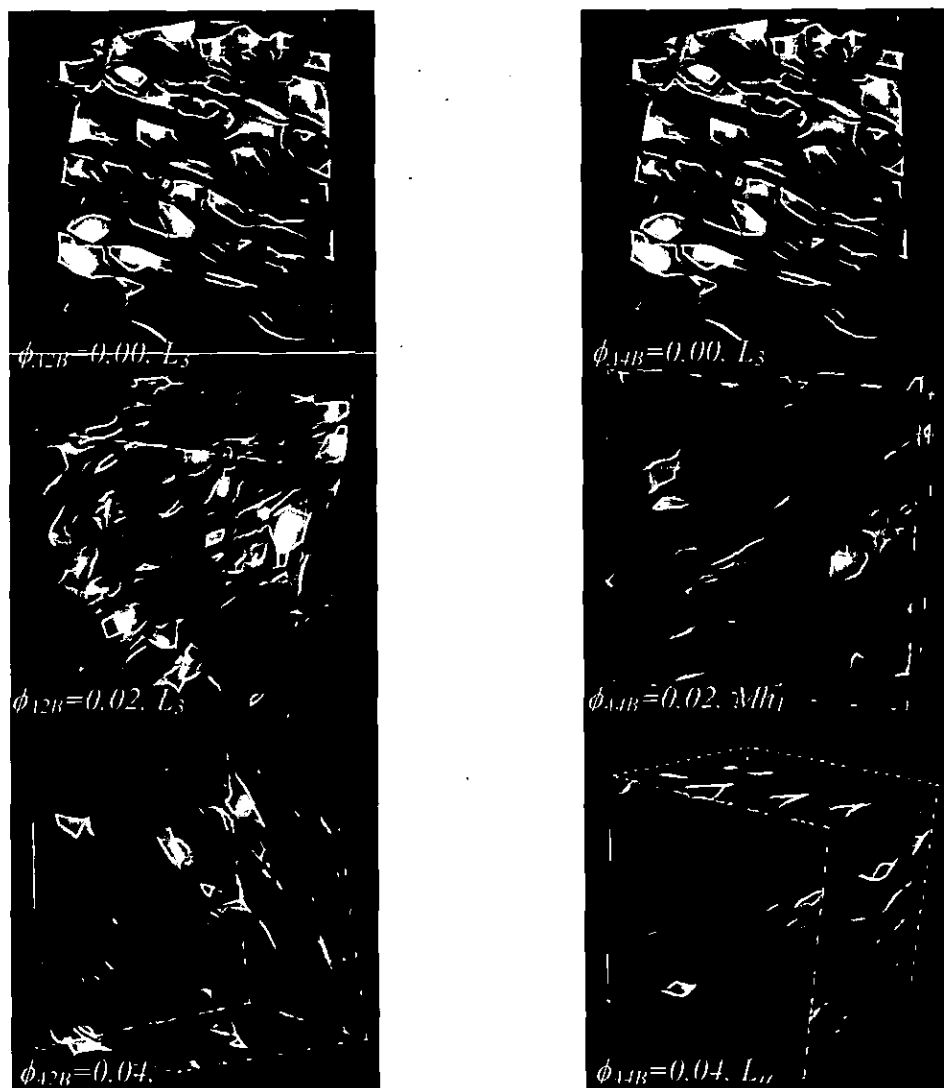


Figure 5.19 Isodensity surfaces showing phase structures on the addition of alcohol A_2B (left) and A_1B (right) at $X_{sw}=0.16$

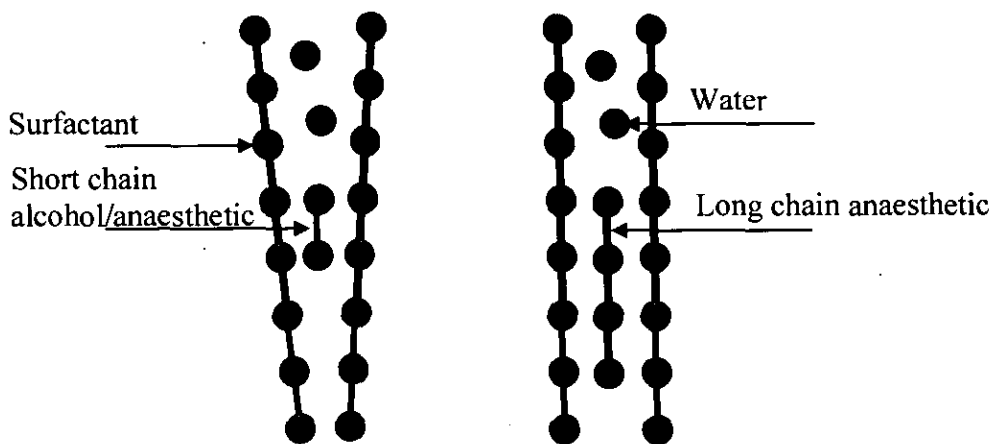


Figure 5.20 Surface curvature promoted by short chain alcohol/anaesthetic molecules (left), Surface Curvature flattened by long chain alcohols (right).

5.7 Summary

The generically modelled anaesthetic increases the curvature of the phases, like a type II anaesthetic. Modifying the anaesthetic so that its tail is lipophobic (as anaesthetics typically are) increases the interfacial curvature, enhancing type II behaviour.

Anaesthetics with $a_{HaW} = 20$ and 15 also had a greater ability to induce higher surface curvature, showing that this enhances type II behaviour.

Anaesthetics with $a_{HaW} = 30$ and 35 still overall served to increase the surface curvature of the phases, enhancing type II behaviour. However, at $X_{sw} = 0.16$ (lower surfactant concentration), where there was more water for the anaesthetic to repel, the effect of these anaesthetics was to decrease the ability to induce higher surface curvatures, diminishing type II behaviour.

Overall, all of the anaesthetics modelled represent type II anaesthetics, even for anaesthetics with $a_{HaW} = 30$ and 35, which were adapted in an attempt to induce, type I behaviour. As type I anaesthetics have polar moieties which displace water from between the ethylene oxide head groups, inducing decreased surface curvature, it is apparent that an increased repulsion parameter alone does not mimic the effect of an ionic charge. This may be why this model failed to model type I behaviour.

Short chain amphiphiles (such as alcohols) promote curved surfaces, but the chain length critically affects the surface curvature, and therefore affects the stability of phases with curvature. If the chain is too short, dV_1 dominates (alcohol AB), if it is too long, all high curvature phases are squeezed out (A_3B and A_4B). There is an optimum chain length for Mh_1 stability and for this model is 2 tail beads (A_2B).

5.8 References

1. I Ueda, "Interfacial effects of anaesthetics on membrane fluidity". In *Drug and Anaesthetic effects on membrane structure and function*, RC Aloia, Ed. Wiley-Liss: New York 15 (1991)
2. R Zhou, "A Study of the effect of anaesthetic molecules on model membranes formed in surfactant/water mixtures". PhD Thesis *University of Central Lancashire*, (2004)
3. M Tomsic, M Bester-Rogac, A Jamnik, W Kunz, D Touraud, A Bergmann, O Glatter. *Journal of Colloid and Interface Science* **294** (1) 194 (2006)

6 Langmuir-Blodgett Trough

6.1 Introduction

Experimental work on monolayers was carried out to provide a comparison to the computational model. Two different anaesthetics - one type I and the other type II (refer to Table 5.3) - were added to monolayers of two surfactants and two different lipids to investigate their effect on monolayer surface pressure.

6.2 Monolayers

A monolayer is a single, closely packed layer of molecules. A Langmuir or insoluble monolayer is a single layer of insoluble, organic molecules spread onto an aqueous surface known as the subphase. Rayleigh first proposed that films on water were one molecule thick ^[1], and it was Langmuir who developed the experimental and theoretical concepts which form the understanding of the behaviour of molecules in insoluble monolayers ^[2].

Molecules in monolayer films can be categorised into different phases, in the same way that molecules in bulk systems can be categorised into different phases. The film can be changed from one phase to another by changing the temperature or surface pressure. There are three main phases that have distinct properties, and these states are known as gaseous, condensed and expanded ^[3-5]. The surface pressure of these phases, and how the surface pressure varies with surface area of the monolayer, characterises the phases. The equilibrium surface pressure, π , of a monolayer is equal to the reduction of the pure liquid-surface tension by the film:

$$\Pi = \gamma_0 - \gamma \tag{6.1}$$

Where γ_0 is the tension of the pure liquid and γ is the tension of the film-covered surface.

In the gaseous phase, the molecules on the surface are far enough apart to exert relatively little force on one another. Gaseous films are characterised experimentally by a surface pressure approaching zero asymptotically as surface area is increased. The surface viscosity is very low. Any monolayer forming substance will exist in the gaseous phase if the molecules are far enough apart.

In condensed monolayers, the molecules are arranged with their closest possible packing, making it effectively a two dimensional crystal. Condensed monolayers of long chain fatty acids, alcohols and glycerides were studied by Langmuir ^[6], where it

was found that the molecules stood nearly perpendicular to the water surface, with terminal polar groups in the water, and the long chains closely packed. Pressure-area plots for condensed monolayers are almost straight and very steep, indicating the very low compressibility due to the strong chain-chain interactions. For molecules in the condensed phase, the surface area per molecule is approximately equal to the cross sectional area of the molecule in a bulk crystal ^[7]. Electron diffraction studies confirm that the molecules are nearly vertical, and optical measurements show that the thickness of the monolayer corresponds to the fully extended chain length.

Expanded monolayers have a molecular area between that of condensed and gaseous films. Expanded monolayer films are characterised experimentally by a surface pressure approaching zero at a constant, steep angle as surface area is increased. The molecular area in the expanded phase is generally two to three times the cross sectional area, and the surface viscosity is also low. Many monolayers that are condensed at low temperature change to expanded at high temperature. Langmuir ^[8,9] suggested that the expanded phase can be thought of as a very thin liquid phase where the hydrophobic parts of the molecules in the expanded film are in a random orientation, where only the polar groups are in contact with the subphase.

Monolayers can be compressed to pressures considerably higher than their equilibrium pressures. Eventually, it is impossible to increase the surface pressure further, and the area decreases if the pressure remains constant or the pressure decreases if the area is held constant. This is known as the collapse point of a monolayer, where molecules are forced out of the monolayer and into the subphase.

6.3 Materials

The local anaesthetics prilocaine hydrochloride and lidocaine (base form) (both 98% purity) were supplied by Sigma (UK), and were used as received. The molecular structure of prilocaine hydrochloride and lidocaine are shown in Figure 6.1. The non-ionic surfactants hexaethylene glycol *n*-dodecyl ether (C₁₂E₆) and hexaethylene glycol *n*-tetradecyl ether (C₁₄E₆) (both 98% purity) were synthesised by Nikkol Chemicals (Japan), and were used as received. The lipids DMPC (1,2-dimyristol-sn-glycero-3-phosphocholine) and DMPS (1,2-dimyristol-sn-glycero-3-phospho-L-serine.sodium salt) were supplied by Avanti Polar Lipids (UK). The molecular structure of DMPC and DMPS are shown in Figure 6.2. Tris (tris{hydroxymethyl} aminomethane) was supplied by Melford (UK), Chloroform was supplied by VWR (UK) and HCl was

supplied by Sigma (UK). Buffers and solutions for experiments were prepared using Milli-Q water (specific resistance $18\text{M}\Omega\text{ cm}$).

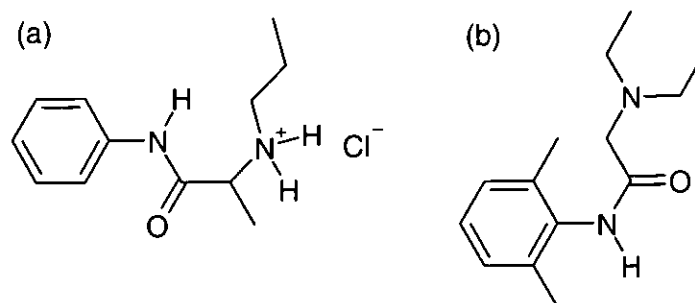


Figure 6.1 Molecular structure of the anaesthetics prilocaine hydrochloride (a) and lidocaine (base form) (b)

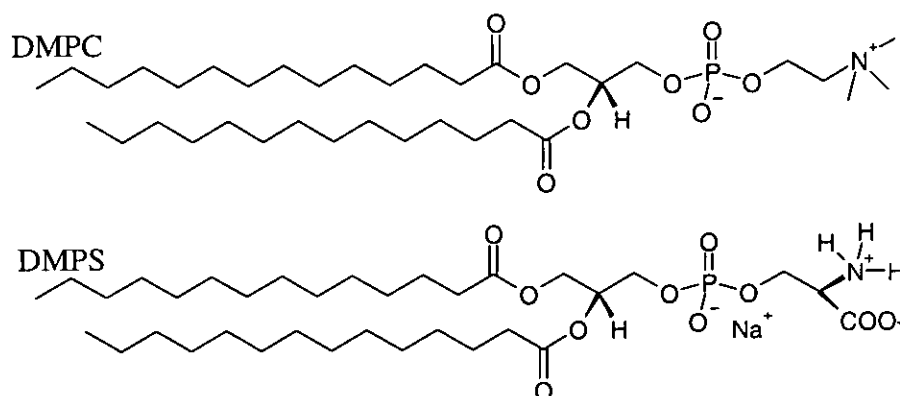


Figure 6.2 Molecular structure of the lipids DMPC and DMPS

6.4 Experimental Apparatus

Surface pressure was monitored by the Wilhelmy method using a 10mm wide paper plate (Whatman's Chr1 chromatography paper) in conjunction with a microbalance, as described by Demel^[10]. Changes in monolayer surface pressure/area were recorded as graphic output on a PC using NIMA software (v5.16), which interfaced with the Langmuir-Blodgett microbalance. Figure 6.3 shows a schematic view of the Langmuir-Blodgett apparatus. All experiments were conducted at an operating temperature of $21.0 \pm 0.1^\circ\text{C}$ and used a subphase of Tris (10mM, pH 7.5 (for prilocaine hydrochloride experiments) or pH 6.5 (for lidocaine experiments)) prepared using purified MilliQ water. The subphase was stirred continuously by a magnetic bar (10rpm). Contaminants were removed from the buffer subphase surface prior to injection by aspiration and a stable surface pressure taken to be that with fluctuations of less than 0.01mNm^{-1} .

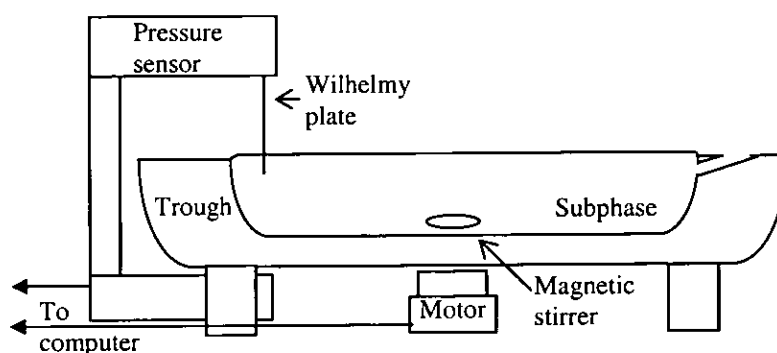


Figure 6.3 Schematic Diagram of Langmuir-Blodgett Trough

6.5 Compression Isotherms

Compressional isotherms are experiments performed at constant temperature that plot the surface pressure of a monolayer as the surface area of the monolayer decreases by compression. They are obtained by compressing a known amount of monolayer forming molecules spread onto the subphase, giving a plot of surface pressure versus surface area per molecule.

Compression isotherm studies were conducted using a NIMA (UK) 601M Teflon Langmuir trough, which possessed surface area dimensions of $5\text{cm} \times 16\text{cm}$ and held a volume of 80ml, mounted on a vibration-isolated table. The trough was equipped with two mechanically coupled Delrin barriers^[11]. Compression isotherms investigated the anaesthetics' behaviour. Monolayers were formed by spreading $5\mu\text{l}$ of 0.004M chloroform solution of lidocaine on to a Tris buffer subphase giving a total of 1.28×10^{16} molecules present on the surface, or $6\mu\text{l}$ of 0.004M solution of prilocaine hydrochloride giving 1.38×10^{16} molecules on the surface. Figure 6.4 shows a Langmuir-Blodgett trough set up for compressional isotherms. After spreading, the solvent was allowed to evaporate off the subphase surface over 30 minutes and then the monolayer was compressed using a barrier speed of $5\text{cm}^2 \text{min}^{-1}$ until monolayer collapse was achieved. For all compression isotherms, changes in anaesthetic monolayer surface pressure with changes in monolayer area were recorded. Figure 6.5 and Figure 6.6 show the isotherms obtained for lidocaine and prilocaine hydrochloride respectively.

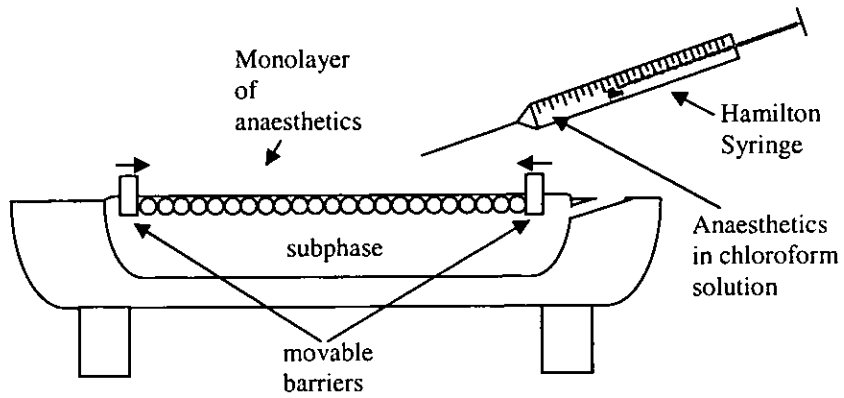


Figure 6.4 Langmuir-Blodgett trough set up for compressional isotherms. Anaesthetics are spread dropwise onto subphase with a syringe allowing a monolayer to form.

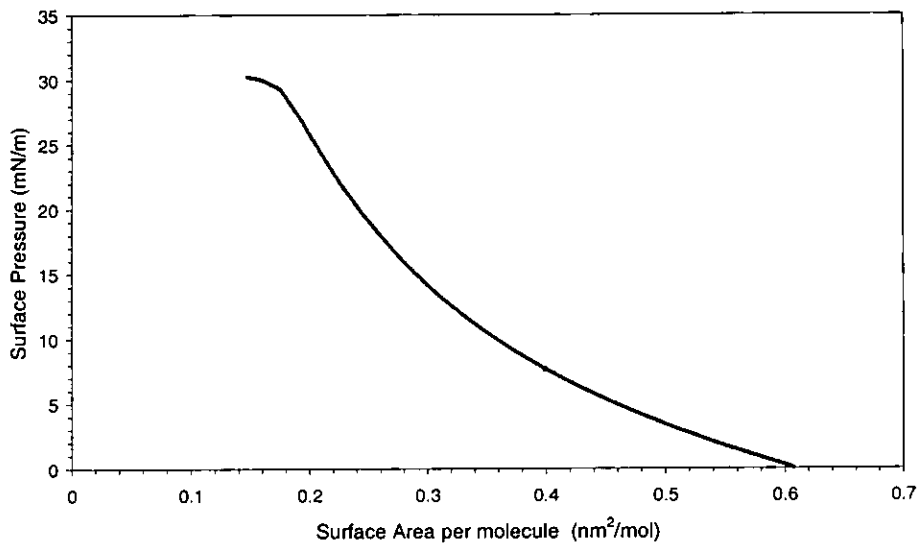


Figure 6.5 Isotherm for lidocaine

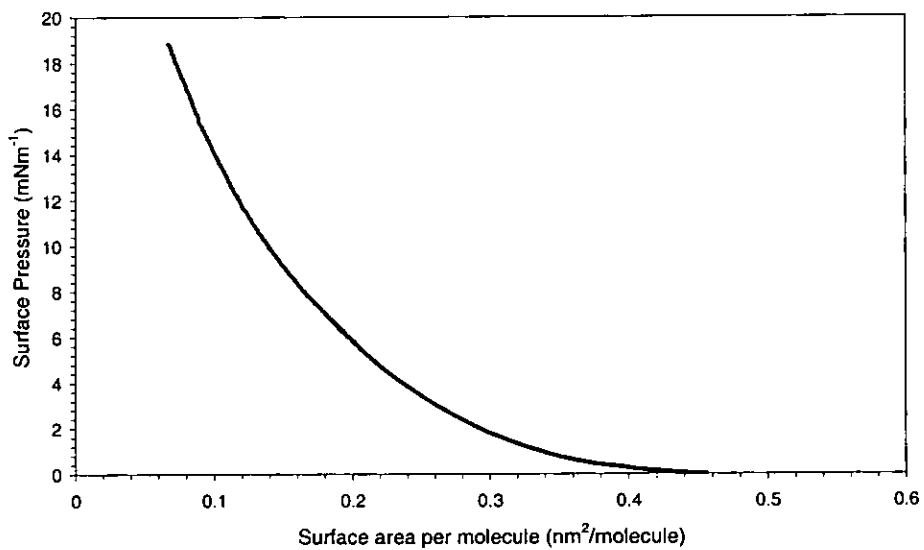


Figure 6.6 Isotherm for prilocaine hydrochloride

Figure 6.5 shows that as the barriers are compressed, the surface pressure increases, and the rate of increase also increases as the barriers get closer together. The curve meets the surface pressure = 0 axis at an angle, indicating that the lidocaine is in the expanded phase. When surface area per lidocaine molecule reaches 15.3 nm²/molecule, the surface pressure reaches a plateau at 30 mNm⁻¹. This is where monolayer collapse occurs, as the surface area per molecule is too small to support a stable monolayer. For Figure 6.6, the isotherm for prilocaine hydrochloride, shows that there is no collapse for this anaesthetic in the range investigated. The surface pressure – surface area curve appears in the same form, rising to 18.6 mNm⁻¹ at a surface area per molecule of 6.8 nm²/molecule, but at maximum compression there is no indication that monolayer collapse is achieved. The curve meets the surface pressure = 0 axis asymptotically, suggesting that the prilocaine hydrochloride is in the gaseous phase. Thermodynamic analysis of compression isotherms was used to investigate the dynamic behaviour of the anaesthetic monolayers. The compressibility modulus, C_s^{-1} , provides a measure of the compressional elasticity of a monolayer and can be used to characterise the phase state of the isotherm, thereby providing information about the compactness and packing of the model membrane^[12]. Values of C_s^{-1} were computed according to:

$$C_s^{-1} = -A \left(\frac{\delta\pi}{\delta A} \right) \quad (6.2)$$

where π is the surface pressure of the monolayer and A represents the area per molecule in the monolayer.

Plots of the values for C_s^{-1} against area per anaesthetic molecule for lidocaine and prilocaine hydrochloride are shown in Figure 6.7 and Figure 6.8 respectively. Figure 6.7 shows that C_s^{-1} increases from 20 to 30 during compression, and suddenly drops to nearly zero at 0.2nm²/molecule, the point of monolayer collapse. A compressibility modulus of approximately 20 to 50 represents the liquid expanded phase^[12], therefore lidocaine exhibits a liquid expanded phase in a monolayer.

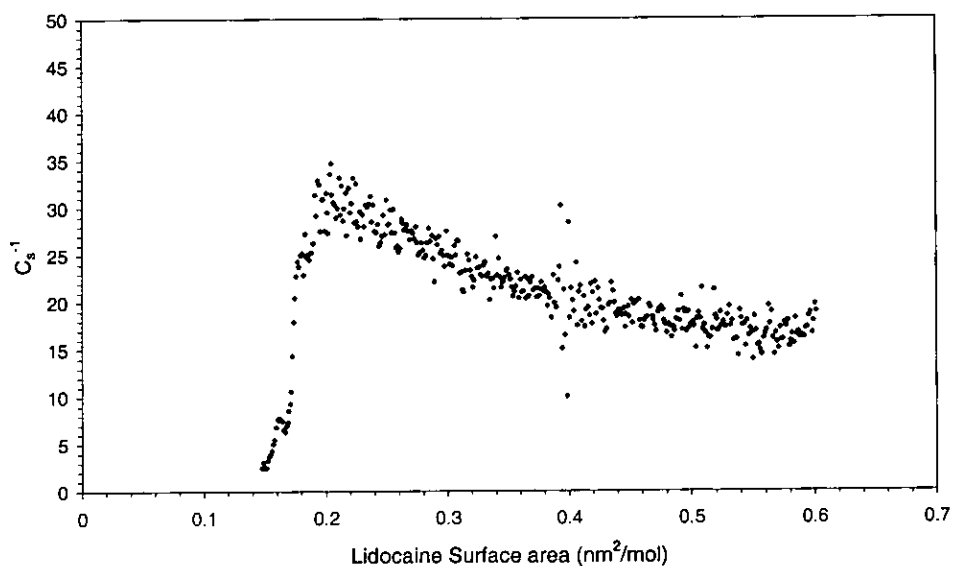


Figure 6.7 C_s^{-1} as a function of surface area per molecule of lidocaine

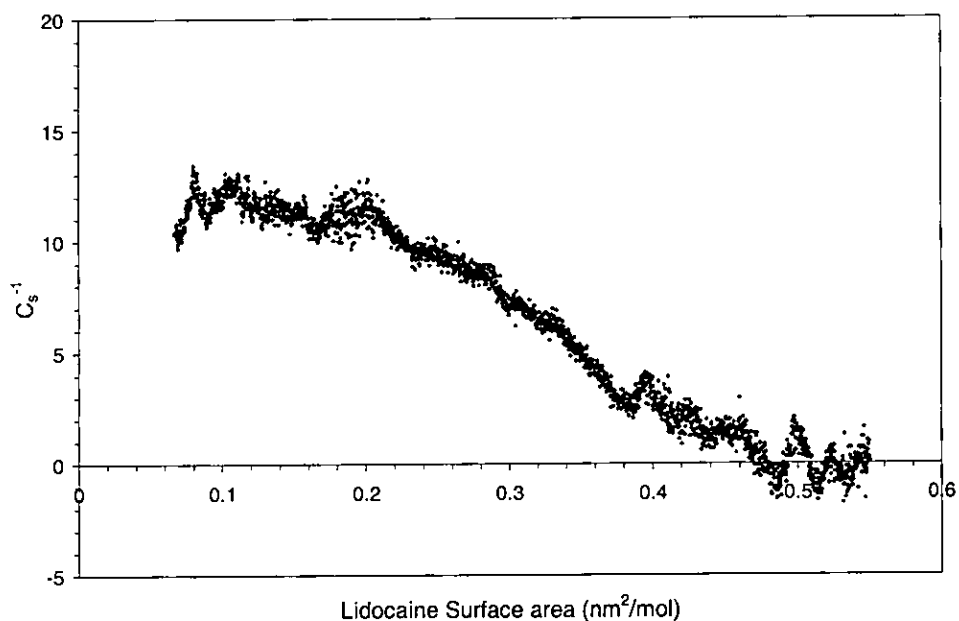


Figure 6.8 C_s^{-1} as a function of surface area per molecule of prilocaine hydrochloride

Figure 6.8 shows that C_s^{-1} increases from 0 to 12 during the compression of prilocaine hydrochloride. If the C_s^{-1} values followed the surface pressure values, it would indicate that the phase is an ideal gaseous phase, following the simplified equation of state $A\Pi = k_B T$. The standard equation of state for gaseous films includes a correction so that when $\Pi \rightarrow \infty$, $A \neq 0$: $\pi(A - A_0) = k_B T$ where A_0 is the surface area actually occupied by the molecules. This equation applies for ideal films, where there is no cohesion or repulsion between the molecules. If strong cohesion exists between molecules, where there is no electrical repulsion or hydrophobic interactions are present (e.g. long

chains), the cohesion is approximately constant over a range of area, and corresponds to the liquid expanded phase. For charged films, the equation of state is more complicated, including a strong repulsive term.

Comparing Figure 6.6 and Figure 6.8, the compressibility modulus does not closely follow the same values as the surface pressure, indicating that prilocaine hydrochloride is not in the gaseous phase. prilocaine hydrochloride is a charged anaesthetic, with large repulsive forces between molecules, and this maybe why it is not either in the gaseous phase, or in the liquid expanded phase as lidocaine.

These compression isotherms confirm that anaesthetics are monolayer forming, behaving like small surfactants. It also reveals a significant difference in the behaviour of lidocaine and prilocaine hydrochloride, because of prilocaine hydrochloride's charge.

6.6 Surface Activity

Surface activity experiments have been performed determining the surface pressure increase for a given concentration of anaesthetic added to the aqueous subphase. Surface pressure will increase with concentration until a certain point has been reached, where the surface pressure will remain constant. These studies enabled an appropriate anaesthetic concentration to be chosen for introducing into surfactant/lipid monolayers, to investigate the pressure increase for different anaesthetic-surfactant/lipid combinations.

Surface activity studies were conducted using a Teflon trough, which possessed surface area dimensions of 6cm × 5cm and held a volume of 15ml, mounted on a vibration-isolated table.

Anaesthetics in 10mM Tris were introduced into the subphase *via* an injection port with a Hamilton syringe to give desired final concentrations. The anaesthetic molecules dispersed to the top of the subphase and formed a monolayer. Concentration and volume of the injected sample were calculated using the formula

$$M_S V_S = M_T V_T \quad (6.3)$$

where V_T and V_S are the volumes of the trough and syringe respectively, and M_T and M_S are concentrations of the trough and syringe respectively.

A schematic diagram of the Langmuir-Blodgett trough set up for surface activity experiments is shown in Figure 6.9.

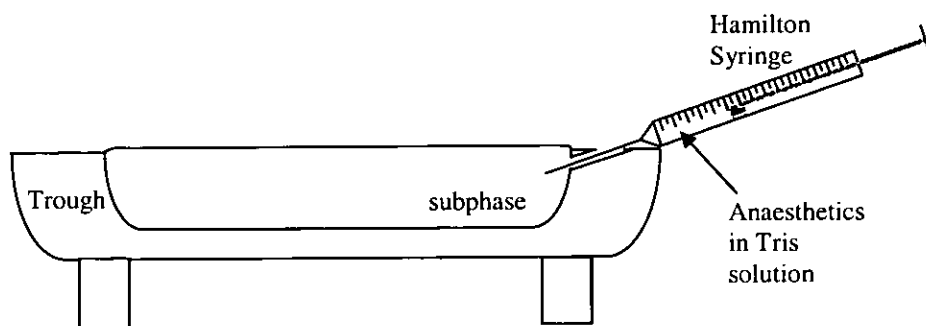


Figure 6.9 Schematic diagram of the Langmuir-Blodgett trough set up for surface activity experiments. Anaesthetics float up to surface after injection.

Various trough concentrations of prilocaine hydrochloride and lidocaine were introduced to the subphase and the resultant surface pressure was recorded to determine the surface activity of the anaesthetics. Figure 6.10 shows a typical surface pressure versus time graph. Surface activity graphs are shown in Figure 6.11 and Figure 6.12 for prilocaine hydrochloride and lidocaine respectively.

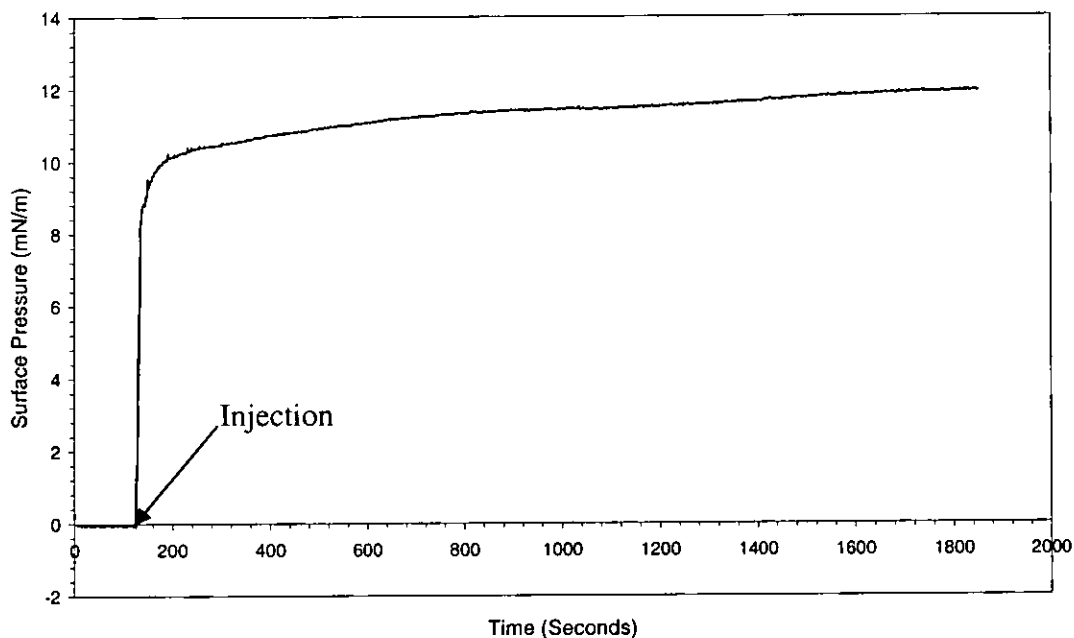


Figure 6.10 Surface Pressure increase on the addition of 10mM prilocaine hydrochloride (after 120 seconds) to a Tris subphase.

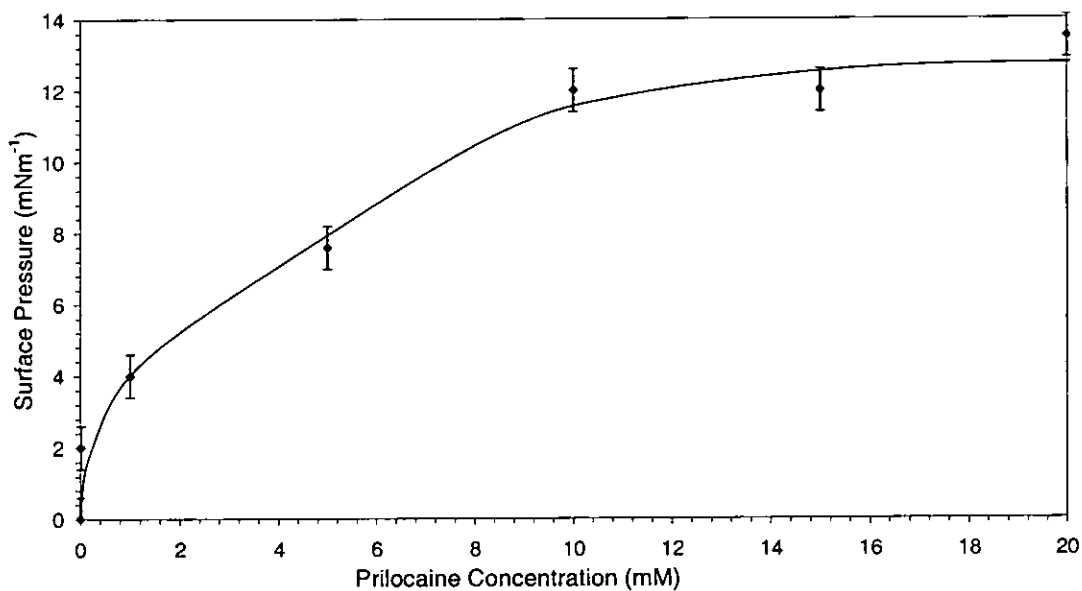


Figure 6.11 Surface Pressure increases of prilocaine hydrochloride added to a Tris Buffer. Line is a guide to the eye.

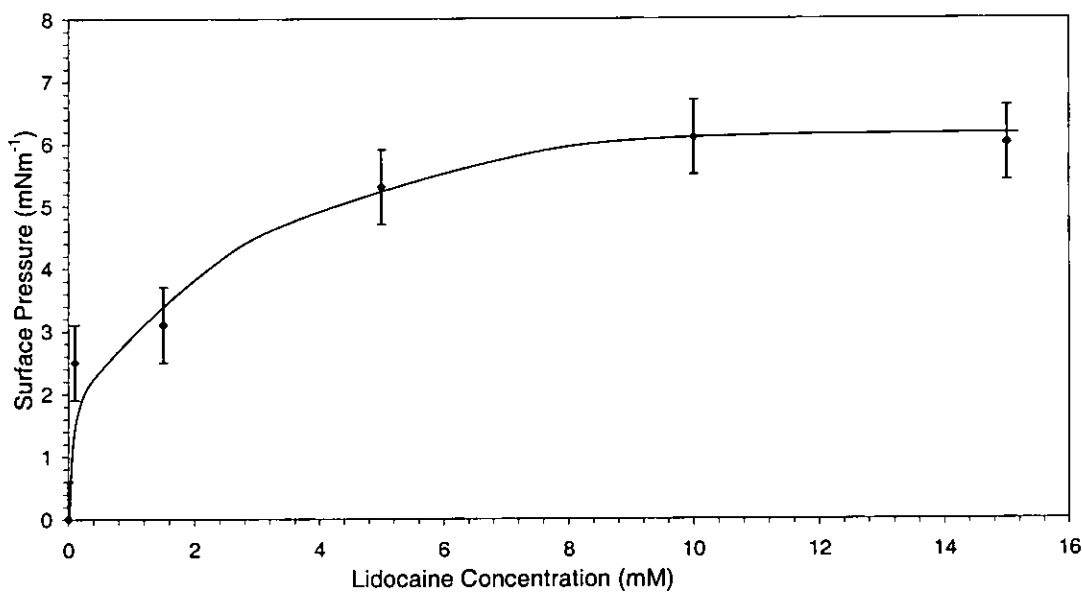


Figure 6.12 Surface Pressure increases of lidocaine added to a Tris Buffer. Line is a guide to the eye.

Figure 6.11 and Figure 6.12 show that the anaesthetic concentration at which the surface pressure increase reaches a plateau is 10mM, for both anaesthetics. This anaesthetic concentration was used as a standard for the main experiments.

6.7 Amphiphile Anaesthetic Interactions

The ability of the anaesthetics to penetrate surfactant and lipid monolayers at constant area was studied. These studies were also conducted using the same trough as surface activity experiments. Monolayers were formed by spreading chloroform solutions of $C_{12}E_6$, $C_{14}E_6$, DMPC or DMPS onto the Tris subphase until a surface pressure of 30mNm^{-1} was achieved. After spreading, the solvent was allowed to evaporate off the surface of the subphase for 30 minutes. After the monolayer had stabilised, the anaesthetics were introduced into the subphase *via* the injection port, achieving a trough concentration of anaesthetic of 10mM . Anaesthetic molecules dispersed to the top of the subphase and spread out, interspersing with the existing monolayer. Interactions of the anaesthetics with monolayers were measured as changes in monolayer surface pressure versus time. Figure 6.13 shows the Langmuir-Blodgett set up for these experiments. Figure 6.14 shows a typical surface pressure versus time graph. Surface pressure increase for the two anaesthetics introduced to the surfactants and lipids are shown in Table 6.1. As results for the two surfactants and two lipids are all within experimental error, Table 6.2 combines these results to aid analysis for the differences in surface pressure increases for non-ionic and ionic lipids with both anaesthetics.

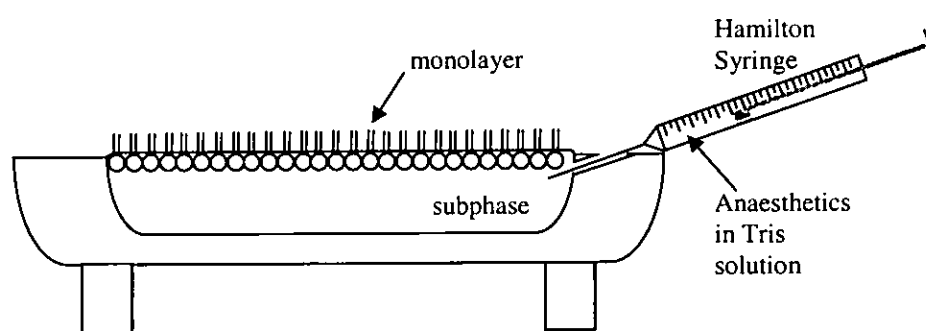


Figure 6.13 Langmuir-Blodgett set up for amphiphile-anaesthetic interaction experiments. Anaesthetics float up to surface after injection, changing surface pressure of monolayer.

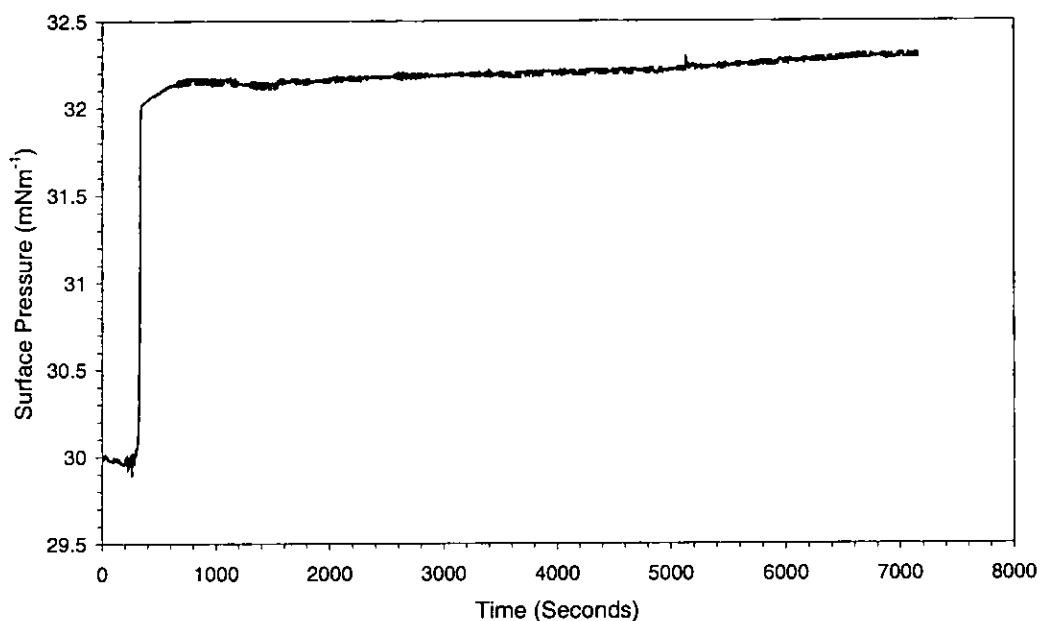


Figure 6.14 Typical surface pressure increase plot: The addition of 10mM lidocaine to a DMPC monolayer.

Anaesthetic	Surfactant/Lipid	Surface Pressure Increase (mNm^{-1}) $\pm 0.1 \text{ mNm}^{-1}$
Prilocaine Hydrochloride	C_{12}E_6	1.2
	C_{14}E_6	1.3
	DMPC	1.9
	DMPS	1.7
Lidocaine	C_{12}E_6	0.8
	C_{14}E_6	0.9
	DMPC	2.3
	DMPS	2.1

Table 6.1 Surface Pressure increases for different anaesthetic-surfactant/lipid combinations

Anaesthetic \ Monolayer	Surfactants	Lipids
	(Nonionic)	(Ionic)
Lidocaine	0.9	2.2
Prilocaine	1.3	1.8

Table 6.2 Surface Pressure Increases ($\text{mNm}^{-1} \pm 0.1 \text{ mNm}^{-1}$) after averaging results from both surfactants and both lipids.

Considering both surfactant monolayers, the addition of prilocaine hydrochloride induced a higher surface pressure increase than for lidocaine. However, for both lipids, the opposite trend was found, where it was lidocaine that induced the greatest surface pressure change. For both anaesthetics, the lipids induced a greater surface pressure increase than that for the surfactants. These results can be compared to the findings from ^[13]. It was shown that the addition of lidocaine to surfactant water systems has the effect of displacing water from the head groups, decreasing interfacial curvature. The affect of adding prilocaine hydrochloride also decreases interfacial curvature (at pH 7.5), where the association of the charged part of the anaesthetic with the base of the head group may affect surface curvature.

Before specific discussion of these results are considered, it is important to consider the degree of protonation of the anaesthetics at the pH of the buffer. This can be done by comparing the pK_a values of the anaesthetics with their relevant buffer pH. If the pH and pK_a values are similar (within one unit of each other) then the molecule will exist in both protonated and deprotonated forms of similar quantities. If the pH of a solution is more than the pK_a of its molecule (differing by more than one unit) then the molecule's deprotonated form dominates. If the pH of a solution is less than the pK_a of its molecule then the molecule's protonated form dominates. This is in accordance with the Henderson-Hasselbalch equation ^[14]:

$$pH = pK_a - \left(\frac{[acid]}{[base]} \right) \quad (6.4)$$

Table 6.3 shows pK_a and pH values for the two anaesthetics, along with their $[acid]/[base]$ ratios calculated from equation 6.4.

Anaesthetic	pK_a	pH of buffer solution	$pK_a - pH$	$[acid]/[base]$ ratio
Lidocaine	7.86 ^[15]	6.5	1.36	22.9
Prilocaine hydrochloride	7.75 ^[15]	7.5	0.25	1.8

Table 6.3 pK_a and pH values for the anaesthetics showing degree of protonation.

Table 6.3 shows that lidocaine is mostly in its protonated form and prilocaine hydrochloride is in a mixed form. This mixed form will include some molecules that

are protonated and some that are deprotonated. Therefore, due to these conditions, the differences of behaviour of the two types of anaesthetics cannot be established.

Despite this, Table 6.2 still shows the effect that charge plays on the surface pressure. The surface pressure increases for the anaesthetics added to the charged lipids (2.2mNm^{-1} and 1.8mNm^{-1} for lidocaine and prilocaine hydrochloride respectively) were higher than for those added to the non-ionic surfactants (0.9mNm^{-1} and 1.3mNm^{-1} for lidocaine and prilocaine hydrochloride respectively).

The ionic strength I of the subphase can be found using the formula^[14]:

$$I = \frac{1}{2} \sum_i z_i^2 m_i \quad (6.5)$$

where z_i is the number of charges of an ion i , and m_i is its molar concentration, and the sum is over all ions in solution. For lidocaine, predominantly in its protonated form, the molar concentration of ions is 10mM, so taking into account the anions and cations, along with the ions from the buffer solution, its ionic strength will be approximately 20mM. For prilocaine hydrochloride, with an [acid]/[base] ratio of 1.8, the concentration of prilocaine ions will be approximately 6.4mM. Summing over anions and cations for both amino groups of the molecule with the ions from the buffer solution, its ionic strength will be approximately 23mM.

6.8 Conclusion

Anaesthetics are small, surface active molecules, and this work shows that anaesthetics associate with the interface and increase surface pressure. Compression isotherms revealed that lidocaine, the non-ionic anaesthetic is in the liquid expanded phase while prilocaine hydrochloride's phase could not be elucidated, because of the increased repulsion between its charged molecules.

The effect of adding the anaesthetics to both surfactant monolayers is the same, and the effect on both lipid monolayers is the same, indicating that size or small structural differences have a negligible affect on surface pressure. The cause of the differences in behaviour is that the lipids are ionic and the surfactants are non-ionic. Coulombic interactions give rise to an increase in surface pressure increase.

6.9 Summary

Thermodynamic analysis on the lidocaine isotherm revealed that lidocaine is in the liquid expanded phase and monolayer collapse is achieved at $15.3 \text{ nm}^2/\text{molecule}$, where the surface pressure suddenly plateaus to 30 mNm^{-1} . There was no such collapse for prilocaine hydrochloride, whose phase could not be determined.

The effect of adding the anaesthetics to both surfactant monolayers is the same, and the effect on both lipid monolayers is the same, indicating that size or small structural differences have a negligible affect on surface pressure. For both anaesthetics, the lipids induced a greater surface pressure increase than that for the surfactants. The cause of the differences in behaviour is that the lipids are ionic and the surfactants are non-ionic. Coulombic interactions give rise to an increase in surface pressure increase.

6.10 References

1. Lord Raleigh, *Phil. Mag.*, **48** 337 (1899)
2. I Langmuir, *Journal of the American Chemical Society*, **39** 1848 (1917)
3. NK Adam, "Physics and Chemistry of Surfaces"; (1944)
4. WD Harkins, "Physical Chemistry of Surface Films"; (1952)
5. DG Dervichian, *Journal of Chemical Physics*, **7** 931 (1939)
6. KJI Groth, "Proceedings of the Second International Congres of Surface Activity". 275 (1957)
7. I Langmuir, VJ Schaefer, D Wrinch, *Science*, **85** 76 (1937)
8. HJ Trurnit, *Science*, **111** 1 (1950)
9. HJ Trurnit, *Scince*, **112** 329 (1950)
10. RA Demel, *Methods Enzymol.*, **32** 539 (1974)
11. NJ Hardy, TH Richardson, F Grunfield, *A Physiochem. Eng. Asp.*, **284/285** 202 (2006)
12. JT Davies, EK Rideal, "Interfacial Phenomena"; 2 ed. *Academic Press*: New York (1963)
13. M Ardeleanu, "A Study of the effect of anaesthetic molecules on model membranes formed in surfactant/water mixtures". PhD Thesis *University of Central Lancashire*, (2004)
14. PW Atkins, "Physical Chemistry"; 5 ed. *Oxford*: (1994)

15. TL Lenke, DA Williams, "Foye's Principles of Medicinal Chemistry"; 6 ed.
Williams & Wilkins: (2007)

7 Conclusion and Further work

7.1 Conclusion

This piece of research attempted to address how the addition of small molecules can affect interfacial curvature, and hence, phase structures of surfactant-water systems. The understanding of these affects can be utilised to enable phase structures to be controlled by the small molecules, enabling potential applications making use of stabilised phases with significant surface curvature, such as the mesh phase, to be achieved.

It has been shown that surfactant-water systems with added molecules can be successfully simulated using mesoscale dynamics. The results of these simulations agree with experiment.

Small molecules generally decrease surface curvature, losing complex phase structures. Oil added to surfactant-water systems resides in the hydrophobic region, bulking the chain region either in a swelling or penetrating nature, depending on the length of the oil. This bulking effectively destroys any positive interfacial curvature, favouring the lamellar phase at high concentrations. This agrees with previous experimental work.

Short chain amphiphiles (such as alcohols) promote curved surfaces, but the chain length critically affects the surface curvature, and therefore affects the stability of phases with curvature. If the chain is too short, dV_1 dominates (alcohol AB), if it is too long, all high curvature phases are squeezed out (A_3B and A_4B). There is an optimum chain length for Mh_1 stability and for this model it is 2 tail beads (A_2B).

Experiments on the addition of anaesthetics to monolayers have found that coulombic interactions are important where present, and these will inevitably dominate. However, these coulombic interactions have not been successfully modelled here.

Both experimental and computational work has confirmed that anaesthetics/small surfactants are located at the surface, and can profoundly affect phase structure. The dimensions, structure and interactions of these small molecules critically affect the surface in which they reside, affecting surface curvature and hence phase structure. However, using such molecules to engineer phase structures for templating applications may be very difficult because of the extreme chemical environments involved in templating solutions, which may themselves destroy the phase structures that the amphiphilic molecules create.

7.2 Further work

As it has been found that coulombic interactions critically affect the surface curvature, the model could be developed to include ionic interactions and to study the effects.

More experiments could be performed on the langmuir trough studying molecular homologues, changing size and ionic state to understand how different structure and charge of the amphiphiles affect their interaction with the monolayer.

In order to strengthen the conclusions found from the addition of the amphiphilic molecules, it would be useful to investigate the addition of different amphiphilic molecules to different surfactant models to elucidate whether the same pattern reoccurs.

By performing experiments such as grazing incidence diffraction experiments such as Small Angle Neutron Scattering (SANS), the structure and orientation of the anaesthetic molecules within the monolayer could be elucidated. This would also give more clues as to how amphiphilic molecules affect the surface pressure and interfacial curvature.

Appendix A – About OCTA & COGNAC

OCTA is an integrated simulation system for soft materials. It is a joint project of industry and academia, funded by the Ministry of Economy, Trade and Industry (METI), Japan.

OCTA includes four simulation programs or “engines”, including:

- COGNAC (molecular dynamics)
- PASTA (reptation dynamics)
- SUSHI (Edwards self consistent field theory)
- MUFFIN (Continuum dynamics)

COGNAC is the engine that was used in this study, and can simulate both full atomistic and coarse-grained models.

These four engines all use the same Graphical User Interface (GUI), called GOURMET. This is the editor and viewer of text files that the engines use. These text files are written in a user defined format (udf) for ease of manipulation.

These udf files consist of a definition part and a data part. The definition part provides the names to all of the data, and the structure of the data. This can be seen, edited and processed using a script written in a programming language called python. The data part is read and rewritten by the engine during its execution.

To perform a simulation using OCTA, first an input udf file needs to be created containing all of the relevant information about the parameters to be used (such as number of time steps, size of box etc), the number and structure of each type of molecule, and algorithm and engine to be used in the simulation itself (in our case Dissipative particle dynamics and COGNAC, respectively). This is done by writing a python script in a template udf file, that will create a given number of each type of molecule with a given number of beads and their associated bonds for the input udf file.

The input udf file is read and executed by the engine, the output of which is either appended to the input file or put into a separate output udf file. This file not only gives the intermediary and final positions of each bead, but also the velocity and force applied to each bead and the total energy at given time intervals during the simulation, if required. The output file is read by GOURMET, and can be viewed using different visualisation methods (see section 3.4) and can be analysed using existing scripts or creating new scripts to perform specific, detailed analysis of the result.

Appendix B

The following is a succinct description of the C++ program written to create probability density functions for each type of bead in the lamellar phase.

Step 1: Read coordinates of beads

The coordinates of all of the beads from the simulation can be copied into a text file for the program to read. The numbers of each type of molecule are printed on the top line of this file, so that the program can identify how many of each type of bead to identify. The number of beads in an oil molecule is inputted (1 for butane, 2 for hexane, 4 for dodecane and 6 for octadecane). The number of beads in a surfactant molecule is set to 8, and 1 for water. Then the input file can be read, so that each bead is identifiable as a surfactant head, surfactant tail, water or oil.

Step 2: Coordinate transformation

This is done so that the new x axis is normal to the lamellae layers, making it possible to perform the density profile step. The number of repeat distances in each direction, n_x , n_y and n_z are inputted, and the angles α and β are calculated according to the following equations (see section 4.5.1):

$$\alpha = \arctan\left(\frac{n_y}{n_x}\right)$$

$$\beta = \arctan\left(\frac{n_z \cos(\alpha)}{n_x}\right)$$

The lamellar spacing is calculated using the following equation:

$$d_0 = \frac{L}{n_x} \cos(\alpha) \cos(\beta)$$

where L is the box length. Using α and β , the coordinates can then be transformed to new coordinates. Only the new x coordinate is needed for the probability density calculation, so the set of equations used to get the new x coordinate, utilising an intermediary set of coordinates, are the following:

$$x_{\text{int}} = x \cos \alpha + y \sin \alpha$$

$$z_{\text{int}} = z$$

$$x_{\text{new}} = x_{\text{int}} \cos \beta + z_{\text{int}} \sin \beta$$

Step 3: The raw density profile

The density profile can now be taken. First, the number of divisions to be taken within each lamellar layer (the higher the number the higher the resolution of the density profile), and the overall distance over which the density profile will be taken (quoted in number of lamellar spacing distances) are inputted.

The total number of divisions for which bead density profile is taken is simply a multiple of divisions within lamellar spacing (32 was used for all data) and total number of spacing distances (10 was used for all data). The size of each division is simply the lamellar spacing divided by the number of divisions.

Now, the density profile itself can be created. For each bead, for each division or slice, the number of that bead within that slice is summed. This gives the number of each bead across the x axis for the simulation in the total number of divisions (320 for these parameters).

Step 4: The probability density function

Now this density profile over several lamellar layers can be merged into one layer, giving a probability density function across the lamellar phase.

This is done by summing up the number of each bead in the first division of each lamellar spacing, then the second division of each lamellar spacing, and so on until the numbers of each bead of all 32 divisions are summed over all 10 lamellar spacing distances.

Each of these numbers can be divided by the total number of that bead to give a probability density function across a single lamellar layer for each type of bead.

Appendix C

The following is a succinct description of the C++ program written to create probability density functions for each surfactant tail bead in the lamellar phase to study structure of surfactant tails on the addition of oil. The program is essentially the same as the program in Appendix B, but the differences are noted.

Step 1: Read coordinates of beads

This step is the same as in Appendix B, however the input coordinates are read into the program so that each surfactant tail bead is identifiable as 1 (the terminal bead), 2, 3 or 4 (interfacial bead).

Step 2: Coordinate transformation

This step is the same as in Appendix B.

Step 3: The raw density profile

This step is also the same as in Appendix B.

Step 4: The probability density function

This final step is also the same as in Appendix B, however the result is a probability density function across a single lamellar layer for each surfactant tail bead type.

Afterword

When I first started this PhD on manipulating interfacial curvature, I naively thought that by the end, I would know everything there is to know about it. As it turns out, I've only really touched the surface.